High Speed Imaging of Nanoscopic Organisation and Dynamics in the Cell Membrane



Gabi de Wit

University of Oxford

Hilary Term 2016

0.1 Abstract

The ability of the membrane to dynamically organise its lipid and protein constituents is vital to the function of the cell. How this organisation is controlled on the molecular level, however, is poorly understood, in large part due to the two-fold difficulty of observing entities that are both nanoscopic and in rapid motion.

In this thesis, we use interferometric scattering microscopy (iSCAT) for its unique combination of sensitivity, spatial precision and temporal resolution in order to investigate longstanding questions about the physical origins of anomalous diffusion and dynamic phase separation in cell and model bilayer membranes.

Chapters 1 introduces the state of current knowledge in the field of membrane organisation and describes the model frameworks used to interpret and understand experimental observations.

Chapter 2 provides an outline of the development of optical microscopy techniques towards the goals of single molecule tracking and label-free imaging of nanoscopic objects in cell and model membranes, particularly focusing on scattering detection.

Chapter 3 describes the design principles and construction of the iSCAT microscope and characterises the optomechanical stability and localisation accuracy achieved in this work.

In **Chapter 4**, we demonstrate the unprecedented ability to image single nanoscopic domains in motion, by exploiting the sensitivity of iSCAT to intrinsic differences in refractive index between lateral bilayer phases. We directly prove the existence of lipid bilayer mixtures that dynamically form nanoscopic domains, and quantify the sizes and lifetimes of these lipid assemblies for the first time.

In **Chapter 5** we study how a single lipid, ganglioside GM1, diffuses within the

bilayer and interacts with its environment, in order to understand the mechanistic origins of heterogeneous mobility in a simple model membrane system. With iSCAT microscopy we achieve 2 nm spatial precision, and 20 μs temporal resolution, allowing for the facile identification of transient trapping events within sub-10 nm domains. By varying properties of the substrate and the lipid head and tail groups, we identify the factors necessary for the induction of anomalous diffusion and conclude that transbilayer interactions with immobilised lipids in the opposite leaflet explain the observed trapping events. This chapter also examines the effect of the size of the gold nanoparticle label on the measured trajectories, addressing a major concern in single particle tracking studies.

In **Chapter 6** we investigate the effect of the actin cytoskeleton on the mobility and spatial distribution of membrane proteins in hippocampal neurons. The periodic arrangement of sub-membrane actin rings found uniquely in this particular cell type permits the trajectories of single molecules to be spatially correlated with the cytoskeleton for the first time. Using both high speed tracking with 40 nm gold labels and fluorescent single molecule tracking at lower speeds, we observe periodicity in the localisation probability that coincides with the arrangement of actin. Our results suggest that the actin cytoskeleton controls the diffusion of membrane proteins not via its assumed role as a highly impermeable barrier, but by locally slowing diffusion via protein crowding effects.

0.2 Declaration

The work described in this thesis was carried out between July 2012 and September 2015, in the laboratory of Dr Philipp Kukura at the Chemistry Research Laboratory of the University of Oxford. All the work described within this thesis is entirely my own, unless expressly attributed to my co-workers. This work has not been submitted previously for any other degree at the University of Oxford or any other university.

0.3 Acknowledgements

I would firstly like to thank my supervisor, Dr. Philipp Kukura, for the opportunity to carry out this work. This research was driven by a vision that all the pieces will eventually fall into place, which provided inspiration though the long months of puzzling data and seemingly conflicting results, and finally led to the discovery of previously unimagined explanations to complex problems. The past four years have provided a unique environment in which to develop many diverse skills and be a part of a team studying exciting problems. The valuable feedback and discussions have greatly strengthened this thesis from start to finish.

I would also like to thank the Kukura group and the whole iSCAT team, with special mention to Dr. Joanna Andrecka for sharing her considerable biochemistry experience as well as for her good humour in the lab, Dr. Katelyn Spillane for initiating the experimental work on supported lipid bilayers and for showing me the ropes in the wet lab, and Dr. Jaime Ortega-Arroyo for being a wealth of information on microscope construction and data analysis. I also owe much gratitude to Joanna and Dan Cole for valuable feedback on my thesis.

It is my pleasure to thank everyone with whom I have been fortunate to collaborate. In particular, thanks to David Albrecht and John Danial for rewarding collaborations on the neurons project and nanodomains project. Discussions with Dr. Mark Wallace, Dr. Helge Ewers and Dr. Philipp Kukura have also been very useful in planning experiments and interpreting data.

This project would not have been possible without the invaluable assistance of Kevin Valentine, Tim Powell, Charlie Jones and the staff in the Mechanical and Electronics workshops. Thank you for willingly sharing your time and knowledge with a complete novice and for the opportunity to learn a number of principles that were vital to the optimal performance of the microscope.

I would also like to acknowledge the support of the Clarendon Scholarship, which funded this work, as well as assistance from Balliol college and an Andrew Pang Bursary which allowed me the time to write this thesis.

Finally, thanks to my family, to Caterina and Tom, and to the wonderful people who helped along the way.

Contents

0.1 Abstract iii

0.2 Declaration v

0.3 Acknowledgements vi

0.4 Acronyms xiii

0.5 Chemicals xiv

1 Introduction **1**

1.1 The lipid bilayer 2

1.1.1 Lipids 2

1.1.2 Synthesis and delivery of membrane lipids 5

1.1.3 Membrane proteins 6

1.1.4 Asymmetry of bilayer leaflets 6

1.1.5 The membrane-adjacent actin cytoskeleton 7

1.2 Beyond the fluid mosaic model 8

1.2.1 The lipid raft concept 10

1.2.2 Evidence for lipid rafts in cells 11

1.2.3 Organisation beyond the lipid raft model 14

1.2.4 Outlook 19

2 Single Molecule Detection with and without Labels **21**

2.1 Introduction 21

2.2 Scattering labels 25

2.3 Approaches to scattering detection 26

2.4 Intrinsic capabilities of scattering detection 31

2.4.1 Label-free imaging . . . 31
2.4.2 Background subtraction . . . 33
2.4.3 Imaging molecular assemblies . . . 34
2.4.4 Localised heating around gold nanoparticles . . . 35
2.5 Outlook . . . 37

3 Setup Construction and Characterisation 38
3.1 Microscope setup . . . 38
3.1.1 Lasers . . . 39
3.1.2 Cameras . . . 41
3.1.3 Illumination approaches . . . 43
3.2 Construction of the microscope . . . 46
3.2.1 Stabilisation of the objective-sample distance . . . 50
3.2.2 Calibration of tracking in the axial dimension . . . 51
3.2.3 Data acquisition and visualisation software . . . 53
3.3 Data fitting . . . 55
3.3.1 Nanoscopic localisation and tracking . . . 55
3.4 Characterisation of setup performance . . . 56
3.4.1 Optomechanical stability . . . 56
3.4.2 Localisation accuracy . . . 57

4 Label-Free Imaging of Lipid Nanodomains 61
4.1 Introduction . . . 61
4.1.1 Phase separation in mixtures . . . 62
4.1.2 Macroscopic phases vs domains . . . 63
4.1.3 Current methods for detecting micro- and nano-domains . . . 64
4.2 Materials and methods . . . 65
4.3 Results . . . 71
4.3.1 Proof of concept 1: label-free detection . . . 71
4.3.2 Proof of concept 2: detection of nanodomains . . . 71

4.3.3 Control experiments . . . 72
4.3.4 Determining the size of nanodomains . . . 74
4.3.5 Dynamic observation of liquid ordered nanodomains . . . 81
4.4 Discussion . . . 87
4.5 Summary and outlook . . . 91
4.6 Contributions . . . 92

5 Single Particle Tracking in Model Membranes 93
5.1 Introduction . . . 93
5.2 Methods . . . 95
5.3 Results . . . 100
5.3.1 GM1 diffuses anomalously in SLBs on glass substrates . . . 100
5.3.2 Effect of substrate: Brownian diffusion is restored on mica . . 100
5.3.3 Effect of label size: Diffusion is affected on short time intervals only . . . 103
5.3.4 GM1 structure modification: unsaturated tails restore Brownian diffusion . . . 103
5.3.5 Effect of varying GM1 concentration . . . 105
5.4 Discussion . . . 108
5.4.1 Minimum components for anomalous diffusion . . . 108
5.4.2 Mechanistic model . . . 110
5.4.3 Static and dynamic error at short time lags . . . 113
5.5 Summary and outlook . . . 115
5.6 Contributions . . . 116

6 Mobility of Membrane Proteins within a Periodic Actin Network 118
6.1 Introduction . . . 118
6.1.1 The periodic actin-spectrin cytoskeleton in neurons . . . 121
6.1.2 Aims of this work . . . 123
6.2 Methods . . . 123
6.3 Simulations . . . 129

6.3.1 Autocorrelation analysis . . . 131
6.4 Results . . . 133
6.4.1 High speed tracking with iSCAT . . . 133
6.4.2 Spatial modulation in mobility . . . 135
6.4.3 Effect of cytosolic domain on mobility . . . 138
6.4.4 Mobility of a GPI anchored protein . . . 140
6.4.5 Comparison of mobility in axons and dendrites . . . 141
6.4.6 Diffusion analysis . . . 144
6.4.7 Tracking with fluorescent labels . . . 146
6.5 3D localisation . . . 148
6.5.1 3D reconstruction from circular geometry . . . 150
6.5.2 Angular distribution of localisation events . . . 151
6.6 Discussion . . . 153
6.6.1 The cytoskeleton as a traffic jam, not a road block . . . 153
6.6.2 Why is hopping not observed? . . . 153
6.6.3 Could periodic mobility arise from steric interactions of the label? . . . 155
6.6.4 Are GPI anchored proteins confined with rafts? . . . 156
6.7 Summary and outlook . . . 158
6.8 Contributions . . . 159

7 Conclusion and Outlook **160**

Bibliography **165**

Abbreviations

0.4 Acronyms

D_{micro}	Short range diffusion coefficient
D_{macro}	Long range diffusion coefficient
DIB	Droplet interface bilayer
FWHM	Full width at half maximum
HWHM	Half width at half maximum
iSCAT	Interferometric scattering microscopy
PSF	Point spread function
SLB	Supported lipid bilayer
SMT	Single molecule tracking
SNR	Signal to noise ratio
SPT	Single particle tracking
TIRF	Total internal reflection fluorescence microscopy
$\phi = 40$ nm	40 nm diameter

0.5 Chemicals

bSM	Brain sphingomyelin
CTxB	Cholera toxin B subunit
DOPC	1,2-dioleoyl-sn-glycero-3-phosphocholine
DOPE	1,2-dioleoyl-sn-glycero-3-phosphoethanolamine
DPhPC	1,2-diphytanoyl-sn-glycero-3-phosphocholine
DPPC	1,2-dipalmitoyl-sn-glycero-3-phosphocholine
DPPE	1,2-dipalmitoyl-sn-glycero-3-phosphoethanolamine
GPI-GFP	Glycosylphosphatidylinositol anchored Green Fluorescent Protein
GM1	Monosialotetrahexosylganglioside
HEPES	4-(2-hydroxyethyl)-1-piperazineethanesulfonic acid
PBS	Phosphate buffer solution
POPC	1-palmitoyl-2-oleoyl-sn-glycero-3-phosphocholine

List of Figures

1.1 Structure of the lipid bilayer 3

1.2 The three families of lipids found in the plasma membrane 4

1.3 Schematic of the liquid ordered and liquid disordered phases 11

1.4 Schematic of hop diffusion trajectories 16

2.1 Localisation precision as a function of the number of detected photons 23

2.2 Implementations of pure scattering and interferometric scattering schemes, based on an inverted microscope setup 27

2.3 Localisation precision as a function of incident light intensity for iSCAT and dark field detection 32

2.4 Differential imaging by subtraction of static background 34

2.5 Heating due to gold nanoparticles of different sizes 36

3.1 Diagram of the iSCAT/TIRF setup 40

3.2 Illumination approaches for fast and wide-field imaging 44

3.3 Stabilisation of the objective-sample distance 51

3.4 Calibration of particle height based on astigmatism of the fluorescence PSF 54

3.5 Fourier transform analysis of setup stability 58

3.6 Localisation errors in noisy environments 60

4.1 Structures of lipids used to create phase separated mixtures 67

4.2 Schematic of a droplet interface bilayer 68

4.3 Interference fringes in droplet bilayers 70

4.4 Detection of lipid microdomains using iSCAT and TIRF microscopy . 72

4.5 iSCAT imaging of the onset of phase separation in a cooling droplet bilayer 73

4.6 Control of nanodomain size through gradual laser heating 75

4.7 Diffusion coefficient of nanoscopic and macroscopic domains as a function of time lag, and as a function of radius 81

4.8 Radius of solid ordered nanodomains, determined from the diffusion coefficient 82

4.9 TIRF and iSCAT images of quaternary mixtures with varying lipid composition and domain size 83

4.10 Imaging of liquid ordered nanodomains in quasi-equilibrium: appearance, merger and dissolution of domains are observed 85

4.11 Distributions of radius, lifetime, diffusion coefficient and HWHM for liquid ordered nanodomains 86

5.1 Components of the GM1 single particle tracking assay 96

5.2 Anomalous subdiffusion of GM1 in supported lipid bilayers on glass substrates 101

5.3 Brownian motion of GM1 in supported lipid bilayers on mica substrates 102

5.4 Time-dependent mobility of GM1 vs label size 104

5.5 Brownian motion of GM1 with modified lipid tail groups in supported lipid bilayers on glass substrates 105

5.6 Fraction of time that native and modified GM1 lipids are confined, on glass and mica substrates 107

5.7 Radial probability density plots and super-resolved trajectories of confinement sites 109

5.8 A model of nanoscopic rocking of the AuNP/CTxB/GM1 complex . . 111

6.1 A schematic of the actin-spectrin cytoskeleton in neuronal axons and dendrites 122

6.2 Labelling of recombinant protein constructs with AuNPs 125

6.3 An example image of the neuron cell culture, visualised by iSCAT . . 127

6.4 Simulated hop diffusion trajectories on a neurite containing a periodic array of submembrane actin rings 130

6.5 1D autocorrelation of a simulated Brownian trajectory 132

6.6 An example trajectory of the extended transmembrane probe 134

6.7 Modulation of mobility along the axon for a transmembrane probe with extended cytosolic domain 137

6.8 Modulation of mobility along the axon for a transmembrane probe with minimal cytosolic domain 139

6.9 An example trajectory of the GPI-GFP construct labelled with 40 nm gold 140

6.10 Modulation of mobility of GPI-GFP in the distal axon membrane . . 142

6.11 Modulation of mobility of GPI-GFP and transmembrane constructs in the dendrite membrane 143

6.12 Comparison of time-dependent diffusion on the neuron axon for three membrane proteins 145

6.13 Spatial density map constructed from the localisation events of multiple QDot-labelled GPI-GFP probes diffusing on the distal axon, tracked at 200 Hz 147

6.14 Example 3D trajectory of a protein on a neurite, determined from fluorescence imaging with astigmatic focusing 150

6.15 3D trajectory of a GPI-GFP protein on a neuron 152

6.16 Angular distribution of localisation events on a neuron 152

Chapter 1

Introduction

The plasma membrane forms the boundary of every living cell, isolating the cytoplasmic contents from the external environment, maintaining electrochemical gradients necessary for cell function, hosting receptors involved in sensing the extracellular environment and communicating with other cells, and orchestrating nuanced and directed responses to signalling events triggered by molecular scale interactions.

The lipids and proteins that compose the plasma membrane diffuse with rates of up to 10 $\mu\mathrm{m}^2 s^{-1}$, rearranging dynamically with respect to one another. The mobility of individual components is highly heterogeneous in time and space, with consequences for a number of biological functions. Specific molecular motifs have been identified as playing important roles in signalling and other dynamic processes in the membrane, but the complete set of physical and chemical principles that control membrane organisation on nanoscopic to microscopic length scales is still far from being understood. This chapter sets the context for the questions addressed in this thesis and presents various mechanisms thought to describe the key aspects of membrane organisation.

1.1 The lipid bilayer

The basic attributes of the cell membrane arise from the chemical and physical properties of the lipid bilayer. Spontaneously assembled from amphiphilic lipid molecules, the bilayer consists of two opposing leaflets with a hydrophobic core and a hydrophilic surface at the interface with water (Figure 1.1). The lipid bilayer is typically 4-5 nm thick, with local variations depending on the length and conformation of the hydrophobic tails of the constituent lipids.

A key property of the lipid bilayer is that it is a fluid at physiological temperatures and compositions. This discovery instigated a conceptual breakthrough in understanding of cell membranes in the 1970s, described by Singer and Nicolsons "fluid mosaic" model [1] and based on earlier work by Frye and Edidin [2]. The fluid mosaic model also recognises that a significant fraction of the membrane is composed of proteins, solvated by lipids at a ratio of approximately 1 protein for every 50-100 lipids. Over the past several decades it has become clear that cell membranes contain a vast structural diversity of lipids and proteins, whose abundance differs among cell types and between the two leaflets of the bilayer, as well as varying over large dimensions in certain polarised cells, such as epithelial cells and neurons. The composition and locations of membrane lipids and proteins are described below.

1.1.1 Lipids

In most eukaryotic cell membranes, the bilayer is predominantly composed of **glycerophospholipids**, having a polar head group and two hydrophobic hydrocarbon tails (Figure 1.2). The tails are usually fatty acids, and they can differ in length (normally containing an even number of carbon atoms between 14 and 24). One tail usually has one or more cis-double bonds (i.e., it is unsaturated), while the other tail does not (i.e., it is saturated). Unsaturated bonds introduce

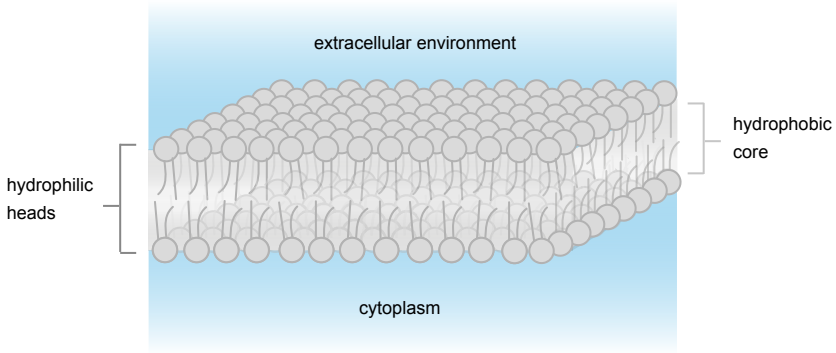


Figure 1.1: The lipid bilayer consists of two opposing sheets, composed primarily of phospholipids arranged tail to tail. The interior region is hydrophobic, while the polar heads are in contact with the aqueous environments of the cytoplasm (inner leaflet) and the extracellular fluid (outer leaflet).

kinks in the lipid tail, and therefore the number of double bonds affects the ability of phospholipid molecules to pack against one another, controlling the density and fluidity of the membrane.

The next most prevalent lipid type are **sterols**, of which only one - cholesterol - is present in most eukaryotic cells. The structure of cholesterol is unrelated to other membrane lipids, consisting of a rigid four ring system. The amount of cholesterol differs considerably from cell to cell, but is usually in the range of 30-40 mol % [3, 4]

The remainder of the membrane is composed of **sphingolipids**, typically accounting for 10-20 mol % [5]. While glycerophophospholipids are based on a glycerin, sphingolipids are based on a ceramide backbone, biologically synthesised from the amino acid serine. The ceramide backbone enables the sphingolipids to function as hydrogen bond acceptors and donors [6, 7] and the interaction between the hydroxyl group on cholesterol and the amide on the ceramide backbone is thought to have an important role in lateral organisation. Glycerin on the other

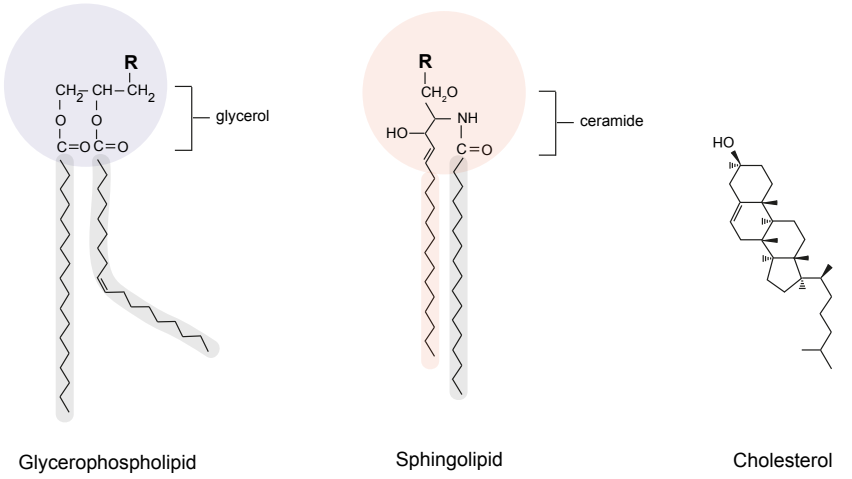


Figure 1.2: The three families of lipids found in the plasma membrane. For glycerophospholipids, R is commonly phosphocholine (PC), phosphoethanolamine (PE), phosphoserine (PS), phosphoinositol (PI). For sphingolipids, R is commonly phosphocholine (PC), phosphoethanolamine (PE) or a sugar or oligosaccharide.

hand is only a hydrogen bond donor and does not interact with cholesterol. Unlike glycerophospholipids, sphingolipids typically contain two saturated tails [8], allowing them to pack tightly together [9], creating an environment which is favoured by the rigid and hydrophobic cholesterol.

Sphingolipids commonly contain a phosphocholine headgroup or a complex carbohydrate headgroup. The latter represent a diverse family of lipids known as glycosphingolipids (GSLs), containing anywhere between 1 and 60 sugar residues. GSLs are found exclusively in the outer bilayer leaflet, where they can act as primary receptors for carbohydrate-binding proteins. One widely studied example is the ganglioside, GM1, which is a receptor for the Cholera toxin. In addition, GLSs have been shown to modify the activity of other laterally adjacent receptors in the cell membrane headgroup interactions. The extensive body of literature on GSL functions is reviewed in reference [10].

1.1.2 Synthesis and delivery of membrane lipids

The endoplasmic reticulum (ER) is the main site of *de novo* synthesis of all the lipids that form the plasma membrane and other organelles in the cell. Lipids are subsequently delivered from the ER to their target membranes, often via several intermediate membranes where enzymatic modifications cause lipid structures to diverge and gain complexity. Lipids may be incorporated in their destination membranes either as final biological products, or as structural starting points for further modification [11]. A detailed description of the synthesis and trafficking of glycerophopholipids, sphingolipids and cholesterol can be found in the review by Blom [12].

Because of their hydrophobic tail groups, lipids cannot be transferred by free diffusion within the cytoplasm. Lipid trafficking is achieved instead by one of three mechanisms: budding of vesicles, which diffuse through the cytoplasm and fuse with the target membrane; transport within carrier proteins exhibiting a hydrophilic surface with peptides targeting the donor and acceptor membranes; or transfer of lipids via direct contact of two membranes [12].

Sorting of lipids and proteins occurs both in vesicles and the trans-Golgi complex, allowing subsequent delivery of specific lipids and proteins to targeted membranes [13, 14]. The organisation of lipids and proteins are highly interrelated, due to the ability of lipids to recruit soluble proteins, and to modulate the localisation of membrane associated proteins, as well for proteins to gather a lipid shell [12]. Once lipids reach their destination, active transport mechanisms enrich specific lipids in the cytosolic leaflet, or the extracellular leaflet of the plasma membrane [11].

1.1.3 Membrane proteins

The lipid bilayer houses a diverse array of proteins and protein complexes, including receptors that relay information between the internal and external environment, transport proteins that move molecules and ions across the membrane, enzymes for a wide range of biochemical reactions and cell adhesion molecules that allow cells to recognise each other and mediate the immune response.

Membrane proteins associate with specific lipids in the bilayer, by forming a lipid shell which moves together with the protein. A number of membrane proteins also interact specifically with other proteins via the cytoplasmic or extracellular ectodomains, in particular by transiently forming homo-dimers. As such, proteins play a role in defining lipid organisation. Conversely, the lipid environment has been reported to affect the functional state of proteins [15].

Proteins that are permanently associated with the membrane are termed "integral" membrane proteins. Such proteins include transmembrane proteins, characterised by one or more membrane spanning domains, and lipid-anchored proteins, in which the protein has been post-translationally modified at the C-terminus position by the addition of a lipid tail. A ubiquitous lipid modification is the glycosyl-phosphatidyl-inositol (GPI) anchor, a complex glycolipid moiety with two, usually saturated acyl chains. The mobility of GPI anchored proteins depends in part on the properties of the lipid tail, and is affected particularly by the length of the acyl chains forming the GPI anchor [16, 17].

1.1.4 Asymmetry of bilayer leaflets

The membrane composition is asymmetric with respect to both lipids and proteins. The extracellular leaflet contains most of the sphingolipids, and all of the GPI-anchored proteins, whereas the cytoplasmic leaflet is enriched in PI

(phospatidylinositol) phospholipids and the negatively charged PS (phosphatidylserine) [18] phospholipids. This asymmetry is maintained by specific membrane proteins which actively flip the lipids from one leaflet to the other [19]. Cholesterol is equally distributed in both leaflets, which is consistent with its high rate of spontaneous flipping between the two leaflets (on the order of 1/s) [5].

1.1.5 The membrane-adjacent actin cytoskeleton

Beneath the plasma membrane lies a network of protein filaments, primarily composed of the protein actin. One of many distinct actin structures in the cell, this network is commonly referred to as the cortical (meaning peripheral) actin cytoskeleton, due to its immediate proximity to the boundary of the cell.

The cortical actin network plays important physical roles in defining cell shape and resisting mechanical stress [20]. Additionally, actin-membrane interactions appear to play an integral role in the organisation of membrane lipids and proteins [21, 17] as well as in regulating the dynamic organisation of actin [22].

Dynamic assembly of actin filaments

Actin filaments, or f-actin, are formed from single actin units, called g-actin (g for globular), which polymerise into elongated structures having a typical length of up a few microns in living cells. F-actin has a diameter of 7 nm, and forms with a right handed helical twist with a repeat lenth of 36 nm on average [23].

Actin filaments are assembled and disassembled dynamically, with the shape and stability of actin networks being controlled by dozens of regulatory actin-binding proteins, some of which are activated by membrane lipids. A recent review of actin-regulating proteins can be found in [22]. The actin networks in most cell types are random, forming a 3D mesh with a depth between 50 nm - 2 μm [24]. In some

cell types actin networks have a regular, 2D structure, where the actin filaments are interconnected with other cytoskeletal proteins, in particular spectrin and Band 4.1, and capped by adducin which prevents polymerisation or depolymerisation at the filament ends. The first example of this type of 2D structure was identified in red blood cells some twenty years ago [25] and a similar geometric structure has recently been found in neurons [26, 27].

Actin mesh sizes in dynamic networks are typically in the range of 100 300 nm diameter, as measured via electron tomography [28]. Mesh sizes in periodic structures have been measured by electron microscopy and super-resolution fluorescence microscopy, and are of comparable dimensions. Considering the 7 nm diameter of actin filaments, the cortical actin network covers a small fraction of the plasma membrane area.

Actin-membrane connections

The actin network is anchored to the cell membrane via a number of linker proteins [29, 30]. Most associations are indirect, through actin-binding protein which also bind to lipids, transmembrane proteins or peripheral membrane proteins. Such interactions are also transient, the lifetime depending on the dissociation rate of the adapter proteins with both actin and the membrane. Actin also binds to some transmembrane proteins, forming a direct link between the cytoskeleton and the membrane [30].

1.2 Beyond the fluid mosaic model

As early as a few years after the proposal of the "fluid mosaic" model, aspects of membrane organisation were discovered that could not be explained in terms of a randomly organised lipid and protein matrix. The earliest example was the

discovery of compositional differences between regions of polarised cells. Early work on epithelial cells indicated that the interior facing surface of the plasma membrane, also called the apical surface, is enriched in sphingolipids (glycosphingolipids and sphingomyelin) and cholesterol, whereas the basolateral surface is higher in unsaturated phospholipids [31, 5].

A more general concept of membrane compartmentalisation was later developed, driven by evidence that smaller and hence less easily detectable heterogeneities were present in a wide range of cell types. This idea was based largely on a technique to isolate parts of the cell membrane according to their solubility in detergents such as Triton X-100. The insoluble fractions, termed Detergent Resistance Membranes (DRMs) were found to be higher in sphingolipids, cholesterol and a number of signalling proteins [32, 33].

The correspondence between DRMs and specialised domains present in the cell was widely postulated. Several concerns about the validity of this interpretation have been raised, however, owing to evidence that detergent treatment can alter the original location of some proteins [34, 35], and that the low temperature at which extraction is carried out can change the phase properties [36, 37]. Furthermore, the addition of detergent to the membrane changes the thermodynamic properties of the lipid mixture, and promotes domain formation at high concentrations [38], while the particular detergent used, the length of treatment, and other conditions varying from one laboratory to another also affected the composition of DRMs.

Nonetheless, the idea of spontaneously assembled domains enriched in specific lipids and proteins presents intriguing possibilities as a potential mechanism for a number of membrane-mediated processes, from protein sorting to receptor assembly to lipid-controlled modulation of protein conformation.

1.2.1 The lipid raft concept

To explain DRM results, the concept of "lipid rafts" was introduced, the description of which has evolved over time to the current, rather broad definition as "dynamic, nanoscale, sterol and sphingolipid - enriched, ordered assemblies of proteins and lipids, in which the metastable raft resting state can be stimulated to coalesce into larger, more stable raft domains by specific lipid-lipid, protein-lipid and protein-protein oligomerizing interactions" [39].

A potential mechanism for the formation of lipid rafts was recognised from studies in biomimetic model membranes, which exhibit the tendency to separate laterally into two phases [40, 41]. At most biologically relevant cholesterol concentrations both the phases have the properties of a liquid, and are distinguished by different degrees of order, and accordingly named the "liquid ordered" and "liquid disordered" phase. [1] The liquid ordered phase is enriched in lipids with long, saturated tails, while the disordered phase is enriched in unsaturated lipids. This distinction matches the experimentally observed partitioning of lipids into detergent-insoluble and detergent-soluble phases. Furthermore, macroscopic liquid phase coexistence has been observed in giant plasma membrane vesicles extracted from cells, but only upon cooling to room temperature [42, 43]. Simulations similarly show phase separation, driven by the unequal interaction energies between different lipid species [44, 45]. A number of signalling proteins contained in the detergent-insoluble fractions in previous experiments have been found to associate preferentially with the liquid ordered phase in cell-extracted membrane vesicles, suggesting that DRMs may indeed reflect the intrinsic organisation of the cell membrane [42, 43]. The relationship between extracted vesicles and the original plasma membrane is debated, however, as the chemical treatments used to extract part of the plasma membrane remove a large and unknown fraction of the

[1] While unimportant biologically, additional phases can occur higher or lower cholesterol compositions, including a solid "gel" phase.

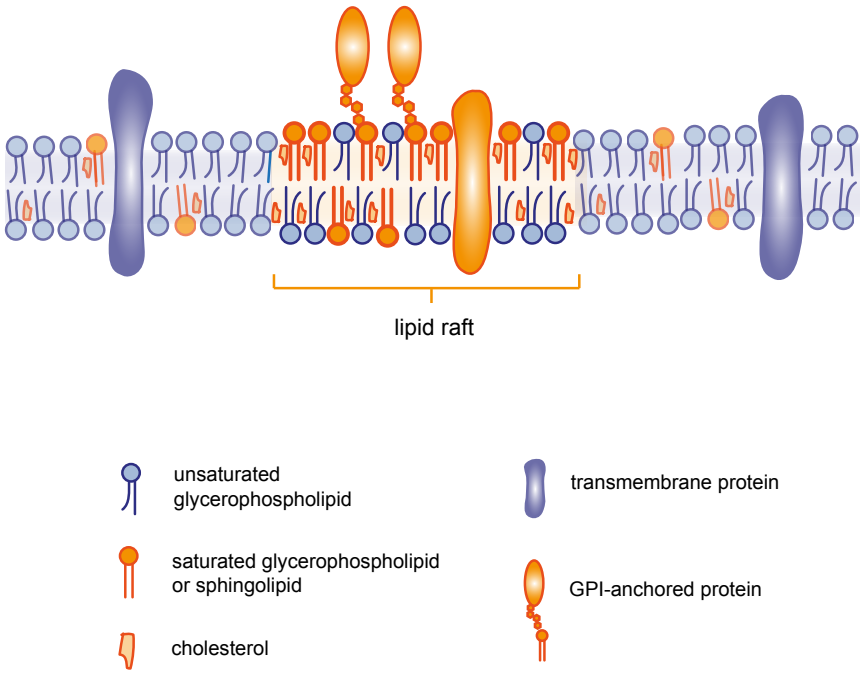


Figure 1.3: Schematic of the liquid ordered and liquid disordered phases in a bilayer membrane.

proteins originally embedded within, and attached to, the membrane.

1.2.2 Evidence for lipid rafts in cells

The ability to directly study heterogeneous organisation in cell membranes has emerged in the past two decades with the development of fluorescent proteins and fluorescent lipid analogues and the advent of highly sensitive optical methods [46, 47, 48, 49, 49, 50, 51, 52]. Measurement of the lateral diffusion of ensembles of molecules and even individual molecules within the membrane is now routinely achieved. As mobility is closely related to membrane structure (as well as molecular interactions), this provides a method to study membrane organisation on nanoscopic lengthscales [53, 54, 55, 56].

A vast number of techniques have been developed to probe various aspects of membrane organisation and dynamics, particularly based on one of three methods: Fluorescence Recovery After Photobleaching (FRAP) [57, 58]; Fluorescence Correlation Spectroscopy (FCS) [59, 60, 61]; and Single Molecule Tracking or Single Particle Tracking (SMT / SPT) [62, 54]. These techniques have supplied detailed information on membrane organisation and dynamics that are consistent with the raft hypothesis. For example, ussing FCS, Bacia and coworkers showed that it is possible to distinguish a raft marker (GM1) from a non-raft marker by their different diffusional mobilities in cells [63]. Recent experiments using Stimulated Emission Depletion FCS (STED-FCS), have revealed the cause of the slowed raft-marker mobility as transient trapping ($\sim$ 10 - 20 ms) within $<$20 nm diameter areas [64, 65, 66]. The finding has been replicated with a novel fluorescence photon counting method using point detectors [67]. In all cases, trapping was observed for raft lipids and GPI anchored proteins, but not for unsaturated lipids, and was dependent on cholesterol.

With fluorescently labelled lipids it is also possible to study the co-localisation between molecules. Using a number of methods, different groups have shown that GPI-anchored proteins exist predominantly as homo-dimers, remaining together for timescales up to seconds [68, 69]. The distribution of GPI-anchored proteins has also been investigated via Förster Resonance Energy Transfer (FRET) methods. Measurements of the fluorescence anisotropy as a function of homo-FRET indicate clustering of GPI-anchored proteins, with fits to parameterised models yielding 2-4 molecules per cluster [70, 71, 72]. From photobleaching behaviour, these clusters were found to be immobile, but continuously reforming. The authors suggest that the transient nanodomains form at sites where proteins are anchored to underlying actin asters - populations of shorter dynamic actin filaments undergoing actomyosin contractility [21].

A complementary approach to detecting rafts is to probe the phase of the bilayer. One property that differs markedly between the ordered and disordered phase, is the degree of water permeability into the bilayer, which is higher in the disordered phase. The bilayer polarity as a function of z position has been used to detect nanoscopic rafts in model membranes via small angle neutron scattering [73] and in cell membranes via electron spin resonance of phospholipids bearing a spin-labelled nitroxide moiety on the acyl chain [74]. Fluorescent labelling methods have also been applied, using reporter dyes which change emission wavelength depending on the polarity of the solvent. The lipophilic dye Laurdan, has been found to be well suited to these measurement [75, 76]. Recently, by combining measurements of Laurdan polarisation (the relative intensities at blue and red wavelengths) with FCS in live cells, Sanchez and coworkers observed fluctuations in polarisation that can be modelled as the diffusion of rafts with sizes in the range of 25 - 300 nm [77]. Additional information on membrane environment can be obtained by recording the ultrafast shift in emission wavelength [78, 79], which reflects the mobility of the lipid shell. Due to the technology requirements, such time resolved experiments record total intensity across the membrane. Alternately, time-resolved microscopy has been demonstrated via fluorescence lifetime imaging (FLIM), which detects the fluorescence decay lifetime at each pixel. In this case, the ideal reporter dye has a lifetime this is highly sensitive to the solvent polarity. Using this technique, Stöckl and coworkers [80] detected submicroscopic domains in model and cell membranes.

Discrepancies in the raft description

While there is a significant body of evidence to support the existence of lipids rafts, a number of experimental approaches have nonetheless failed to detect lateral heterogeneity consistent with the raft hypothesis. Some hetero-FRET measurements, for example, yield no indication of nanoscale heterogeneity [81, 82].

Measurements of long-range diffusion of different lipid markers which are known to preferentially associate with either the liquid ordered phase or the liquid disordered phase in model membranes, should provide an alternate method to probe membrane structure. Measurements of such markers in cells, however, yield similar diffusion times [83]. In addition the reported size of putative rafts varies widely, from 5 - 300 nm depending on the method used, and the discrepancy in lifetime is even greater, spanning more than four orders of magnitude from less than 1 ms [84] to 10s of seconds [68]. The reasons for the discrepancies are unknown, but it is perhaps not surprising given the possibility that various measurements probe different aspects of lateral organisation, which may have distinct mechanistic origins. Another confounding factor is the model dependent nature of results. As any assertion about lipid rafts is drawn from a hybrid of experimental observation and model-based extrapolation, it is perhaps no surprise that the estimated properties of lipid rafts are so uncertain.

1.2.3 Organisation beyond the lipid raft model

A key finding in support of the lipid raft hypothesis is that raft molecules exhibit organisation and confined mobility that is distinctly different from non-raft molecules. While this is frequently observed, a number of studies have also reported general factors that affect the diffusion of all membrane components, or that depend on molecular structures that are not necessarily related to raft association.

One set of evidence suggesting an additional mechanism of membrane organisation is the high speed imaging of single molecules in cell membranes. Using 40 nm diameter (hereafter written $\phi = 40$ nm) gold nanoparticles as strongly scattering labels, Kusumi and co-workers have recorded trajectories of single molecules at 40 kHz frame rates, up to 1000 times higher than that typically accessible with

fluorescent labels. The authors found that simple phospholipids, sphingolipids, GPI-anchored and transmembrane proteins all undergo anomalous diffusion in live cell membranes [85, 86, 87, 84]. Visual analysis of trajectories appears to indicate that single molecules diffuse within confined regions of 10s-100s nm, and occasionally "hop" to immediately apposed regions on 1-10 ms timescales [87, 84, 86], too fast to be detected by fluorescent labelling methods. The size of these compartments has been determined for various cell types, and is typically in the range of 100-700 nm. These dimensions are much larger than the 20 nm trapping regions observed by STED-FCS and photon counting methods, and furthermore the existence, compartment size and timescale of hopping are not significantly affected by cholesterol depletion [86, 88], a tenet of the raft hypothesis.

Corraling by the actin cytoskeleton

Based on these findings, Kusumi and co-workers hypothesised that the anomalous diffusion stems from interactions with the underlying actin cytoskeleton. To explain how outer leaflet lipids and proteins are corralled without directly encountering the cytoskeleton, the "picket fence" model was proposed, in which transmembrane proteins immobilised on the membrane adjacent cytoskeleton act as "pickets", relaying the actin fence structure to the membrane. This model is depicted in Figure 1.4, showing an example trajectory of a GPI anchored protein in orange.

This model is consistent with the relatively fast hopping rates observed for lipids and peripheral lipid anchored proteins, compared to transmembrane proteins [84]. Additionally, removal of the cytoplasmic domain of transmembrane proteins was found to result in an increased hop rate [89], whereas the size of the extracellular domain had little effect on diffusion [86]. Partial depolymerisation of actin was found to increase the compartment size, without significantly changing the hop rate [86].

A recent STED-FCS study of a minimal in vitro system consisting of a lipid bilayer bound to an actin network of variable density also reported an inverse correlation between actin density and mobility of both a lipid and protein probe within the membrane [90].

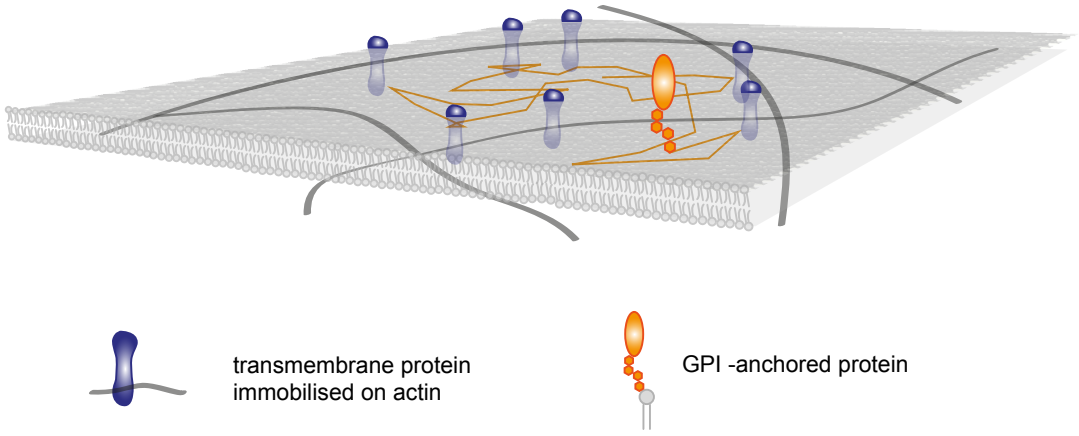


Figure 1.4: Schematic of the actin picket fence. Hopping of transmembrane species (blue) might occur when actin filaments are briefly severed or dissociate from the membrane. Hopping of a lipid anchored protein (orange) can occur when the protein finds a gap between pickets.

The picket fence model is an elegant concept that may explain why oligomerisation and complex formation drastically reduces the mobility of proteins in cells. By extrapolation, it is feasible that actin fences are involved in localising signalling complexes at the point where the extracellular signal has been received [86]. More generally, the picket fence model provides a possible explanation for a long-standing problem - why diffusion coefficients in cells are 5-50 times slower than those measured in reconstituted, actin-free, membranes.

It has not been possible, however, to directly observe hop diffusion with any other technique, as SPT is the only method capable of imaging single molecules with sufficiently high spatial and temporal resolution. Tracking of fluorescently labelled lipids and proteins at high speeds (1 kHz) does not show evidence of actin corrals [67], however this may be too slow to directly detect hopping. Hop diffusion should still be visible as an offset in the mean square displacement as a function of time, however, this has not been observed in fluorescent labelling studies [91].

This suggests that the observed compartmentalisation of trajectories could be an artefact of the gold label. It is well known, that the $\phi = 40$ nm gold label can influence the observed mobility, yielding a reduction by up to a factor of 5 in the macroscopic diffusion coefficient compared with single-molecule tracking of fluorescent lipid or protein analogues [84]. A better understanding of the influence of the gold label is needed to confirm whether such hopping behaviour occurs irrespective of the presence of a label.

Interleaflet coupling

An important function of the membrane is to selectively transmit information from the cell to its external environment and vice versa. It is clear that binding-induced conformational changes in transmembrane proteins could communicate signalling events across the bilayer, but less clear how communication occurs for receptors that

are located in the outer leaflet only, such as the GM1 lipid targeted by the cholera toxin ligand. The question of how interleaflet communication is achieved applies equally to the induction of raft domains from the extracellular to the cytoplasmic leaflet, even though the latter does not have a composition that phase separates on its own.

There is clear evidence that the two leaflets of the bilayer somehow interact, even in simple, lipid-only model membranes. This can be seen from the fact that diffusion of lipids in both leaflets of a bilayer formed on a solid support is the same, and that this value is more than two times slower than in an unsupported bilayer, under identical conditions with bilayers formed of simple phospholipids [92]. It is not clear how this monolayer coupling occurs, though some studies indicate that friction between monolayers varies substantially with the lipid and temperature [93].

Another form of communication can arise from lipid tail interdigitation. While the extent of tail interdigitation occurs in cells is unclear, experiemnts in model bilayers consisting of a mixture of short or unsaturated lipid tails, and long, saturated lipid tails - in particular those of glycosphingolipids - show evidence that the saturated acyl tails cross the bilayer midplane, where they may interact with terminal portions of acyl chains in the opposing monolayer [94].

Other studies have argued, however, that this effect only occurs at low temperature in the gel phase, reporting no interdigitation of lipid tails at physiological temperatures in the presence of cholesterol and in the liquid-crystalline phase. Instead, the carbohydrate headgroup of the glycosphingolipid may be forced farther above the bilayer surface to accommodate the difference in tail length [95].

Recent results have built a strong case for communication across the plasma membrane by long, saturated acyl chains [96, 17], however the exact mechanism remains uncharacterised.

Protein crowding

Interpretation of the lateral diffusion of lipids and proteins in the cell membrane is largely framed in terms of ideal conditions in which the membrane constituents are considered to be highly fluid and, for simplicity, the effects of mobile and immobile proteins on lipid packing and hydrodynamic friction are ignored. As the average distance between membrane proteins is roughly 3 nm in a typical membrane [97], ignoring the effects of membrane protein crowding is a potentially serious oversimplification.

Protein crowding and heterogeneous protein densities could explain several observations, such as wide variation in macroscopic diffusion coefficients in different locations in the membrane [98], as well as complete spatial trapping [99, 100, 101].

The influence of protein crowding on mobility is difficult to measure experimentally, as the density of proteins can typically be determined only on average. Nonetheless, atomic and coarse-grained simulations have revealed that protein crowding can dramatically affect mobility. In particular recent simulations have identified anomalous diffusion to be an intrinsic property of protein motion under crowding [101], while a different study also identified heterogeneity of lipid motion, with lipids in the vicinity of membrane proteins diffusing much more slowly compared to lipids far from proteins [102].

1.2.4 Outlook

The recent expansion in imaging capabilities has revealed that live cells are organised on multiple time and length scales, leading to a renewed description of the plasma membrane that includes lipid nanodomains (rafts), interaction of the membrane with the cytoskeleton, protein-protein and protein-lipid interactions, coupling between leaflets and protein crowding. The individual contributions of these factors to the

mobility of membrane proteins and lipids, however, are not well understood.

A major challenge at present is the lack of non-invasive and highly sensitive methods to visualise membrane domains directly. Currently, the dynamic properties of nanoscopic membrane domains can only be inferred from the behaviour of a subset of labelled molecules. This has led to a range of reported conclusions about the size and lifetime of membrane domains depending on the design of the experiment, and a physical understanding of the dynamics of putative membrane domains has not been developed.

The potential interplay of lipid rafts with the actin cytoskeleton, as well as the effects of interleaflet coupling and protein crowding render experiments in live cells difficult to interpret. Model membrane systems have provided a very useful niche for examining cause and effect of anomalous mobility, and are made use of in this thesis.

Finally, a large part of the reason why membrane dynamics remains a puzzle is the impasse between between the desired and achievable spatial and temporal resolution of single molecule techniques. Even state of the art single particle tracking experiments using colloidal gold labels are limited to resolutions approximately an order of magnitude away from the intrinsic length and timescales of single membrane molecules.

In this thesis we apply a highly sensitive scattering-based technique to the study of single molecule diffusion in cells and model membrane systems, demonstrating spatiotemporal resolution ten times better than state of the art measurements, as well as the ability to image lateral membrane phases on the nanoscale, without any labels, allowing for the elucidation of details of membrane organisation and dynamics previously beyond reach.

Chapter 2

Single Molecule Detection with and without Labels

2.1 Introduction

The advent of single molecule methods over the past two decades has revolutionised the field of cell biology, allowing researchers to directly observe molecular behaviours and interactions on length scales approaching the size of single biomolecules. Single molecule methods have enabled detection of rare and transient events that could not have been accomplished by examining ensembles. For example, molecules associated with lipid rafts experience transient confinement on ms timescales in regions smaller than 20 nm while many signalling-related molecules form transient oligomer complexes with lifetimes of 1 - 10 ms [103, 104, 105]. If one were to measure the behaviour of a sample in bulk, only the average mobility of the ensemble would be observed. Furthermore, detection of transient events and measurement of diffusion in the plasma membrane requires the ability to measure dynamics on fast timescales, together with spatial precision comparable to molecular dimensions (one to several nanometers).

Optical microscopy is unique in offering these capabilities, as well as possessing the important property of non-invasiveness in biological settings. Imaging single molecules is clearly a significant feat, however, considering that light can only be focused to an area of 5×10^{-10} cm^2 with a high numerical aperture objective, resulting in as many as 10^7 molecules in a typical illumination volume. This suggests that in order to detect one and only one molecule within a diffraction limited volume, it must be the only molecule to interact with light, and also interact strongly enough that the optical response can be detected. While the detection of single dye molecules via optical absorption has been demonstrated [106, 107, 108], this approach places demanding requirements on the experimental setup for the small dip in transmitted light to be measurable above fluctuations in intensity due to shot noise. An alternate approach is to detect fluorescence from a single dye molecule, which has the advantage that the fluorescence is red-shifted relative to the illumination light, and therefore the signal can be detected on a zero background with dichroic mirrors and wavelength filters.

A vast array of fluorescent probes have been developed for studying biomolecules within the plasma membrane, including: biomolecular fluorescent analogues, whereby the native molecule has been conjugated to a small molecule dye moiety; endogenous fluorescence proteins that can be expressed in cell culture; small fluorescent proteins that bind to target biomolecules; and dye molecules that preferentially locate in certain chemical or physical environments. As native cells do not typically contain strongly fluorescent molecules, fluorescent probes can provide a means to detect target molecules with 100% specificity, and also offer the advantage of adding minimally to the size of the target molecule.

Having focused up to this point on the sensitivity of single molecule imaging approaches, it is important to address two other factors that characterise the performance of an imaging methodology, namely the spatial precision and temporal

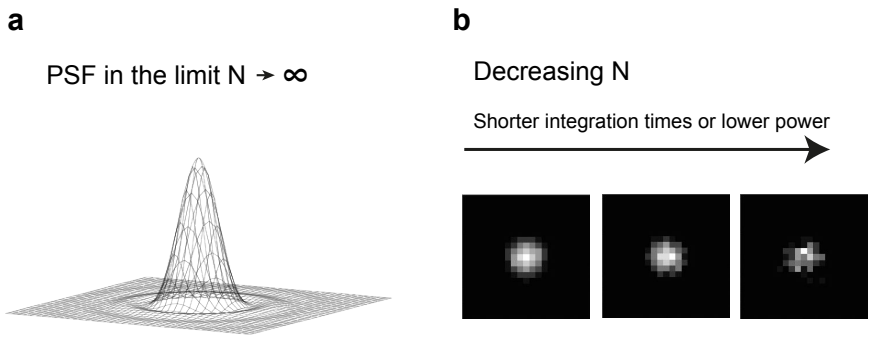


Figure 2.1: a) Single molecules can be imaged by labelling with a probe that produces an optical response under illumination. When imaged onto a camera, the spatial distribution of such a point source resembles a two dimensional Gaussian function with a FWHM given by FWHM $= \frac{\lambda}{2NA}$ where λ is the wavelength of light and NA is the numerical aperture of the light collection optics, as dictated by the diffraction limit. b) The accuracy with which the centre of mass of the PSF can be determined depends on the number of collected photons. For a finite photon flux, faster imaging results in fewer detected photons, and a deterioration in the localisation precision, illustrated for three images. From left to right the total number of photons, N, is 10000, 1000 and 100.

resolution. While the diffraction limit sets the spatial resolution of the microscope, if the density of labels is sufficiently low such that there is less than one emitter per diffraction limited volume, the position of a single label can be determined with a spatial precision much smaller than the optical resolution by determining the centre of mass of the point spread function (PSF), illustrated in Figure 2.1. The accuracy with which the centre can be localised depends on the number of detected photons in the PSF, denoted N. For a stationary particle in the absence of any sources of background noise, the signal to noise ratio scales as $\sqrt{N}$. It is therefore instructive to examine the emission properties of fluorescent probes.

A key factor in the spatiotemporal performance of a fluorescent label is the total number of photons emitted before photobleaching, which falls typically in the range of $\sim 10^5$ - 10^7 photons. If all of the available photons emitted from a single

fluorescent molecule can be used to determine the location of an immobile molecule, then the localisation precision (the Gaussian width in the position measurements [109]) can be better than 1.5 nm [110, 111]. In order to determine a trajectory, however, only a small fraction of the photons are available for each localisation. In a trajectory of 50 steps, it is possible to localise the probe in each frame with ∼10 nm precision in *in vitro* experiments, or 2-3 times poorer in living cells, due to background autofluorescence [112]. This estimate does not take into account the blurring of the position that occurs if the probe moves during the exposure time. One could aim to minimise this blur by recording at a very fast frame rate, however, the maximum photon emission rate from a single emitter is also limited due to the need to populate an excited state with a lifetime typically in the range of 1 - 10 ns, resulting in a photon flux ceiling known as "optical saturation". As a general rule of thumb (again, discounting position blurring), a single emitter can be tracked with a precision of roughly 1 nm $\mathrm{Hz}^{\frac{1}{2}}$, for example, 10 nm precision at 100 Hz. This illustrates that the achievable localisation precision and temporal resolution are two sides of the same coin whereby one can be increased at the expense of the other.

Luminescent semiconductor nanocrystals, also known as quantum dots or QDots, can be pumped much closer to the optical saturation limit without photobleaching, allowing higher spatial and/or temporal resolution, and longer observation times [113]. QDots pose two major disadvantages however, namely the tendency to exhibit "blinking" behaviour due to charge trapping by surface defects, and a relatively large size, totally 10-30 nm in diameter, once passivation layers have been applied to ensure biocompatibility. Like single dyes, the fluorescence signal also decays over time - albeit more gradually - due to photobleaching.

2.2 Scattering labels

Given the limitations of single-emitter-based microscopy and the discrepancy between the achievable spatiotemporal resolution and the level required to image mobile molecules at their intrinsic length scales, alternate approaches to single molecule tracking have been investigated. One such approach relies on detection of scattered light. Scattering from a nano-object is analogous to having a "nano-mirror", whereby the photon flux is only limited by the amount of incident power on the nano-object. The fraction of light scattered is proportional to the scattering cross section, which depends on the refractive index of the object and that of its surroundings, as well as on the object's size and shape. Furthermore as scattering from nanoscopic objects is not subject to photobleaching or blinking, indefinite observation times are possible.

For a particle that is small compared to the wavelength of light, the scattered waves from all parts of the particle are in phase, which allows the scattering amplitude to be expressed according to the expression:

$$s(\lambda) = \epsilon_{med}(\lambda)\pi\frac{D^3}{2}\frac{\epsilon_{obj} - \epsilon_{med}}{\epsilon_{obj} + 2\epsilon_{med}} \tag{2.1}$$

where ϵ_{obj} / ϵ_{med} is the complex dielectric constant of the object / medium. Equation 2.1 implies that the scattered field depends on the difference in refractive index between the particle and medium, and also scales with the volume, V, of the particle.

Several types of particles are commonly used as scattering labels, including silica and latex beads and metal nanoparticles, with coupling to biological targets achieved by attaching proteins, ligands or antibody fragments that confer specificity to the molecule of interest. As scattering cross-sections are smaller than fluorescence cross sections, scattering labels must typically be at least 10s to 100s of nanometers in diameter to allow detection with a sufficient signal to noise ratio. It is clearly

desirable to minimise the label size, as large labels can potentially perturb the underlying motion of the molecule being studied. Small metallic nanoparticles are particularly useful in this regard as they exhibit enhanced scattering at the plasmon resonance wavelength due to coherent oscillations of electrons. Gold in particular is a label of choice in biological applications as gold nanoparticles are inert, non cytotoxic, and the plasmon resonance wavelength is in the visible light region [114]. A $\phi = 40$ nm gold nanoparticle illuminated at 532 nm exhibits roughly the same scattering cross section in water as the 160 nm diameter silica bead, thereby enabling the use of a much smaller label for the same scattered photon flux.

2.3 Approaches to scattering detection

Dark field detection

Unlike fluorescence, scattered light cannot be separated from incident light based on wavelength, and therefore requires alternate detection strategies. Biological applications commonly make use of the evanescent field from a totally internally reflected beam to excite scattering labels, which poses the dual advantages of illuminating a thin region of the sample, and allowing for the scattered light to be detected with theoretically zero background. This approach of Total Internal Reflection Dark Field Microscopy (TIRFDM) is illustrated in Figure 2.2 a. The light scattered by a single emitter appears as a bright spot on a dark background, analogous to fluorescence imaging (Figure 2.2 b).

Interferometric detection

A second approach to scattering detection is based on interferometry, whereby rather than excluding the incident light, a part of the incident beam is collected

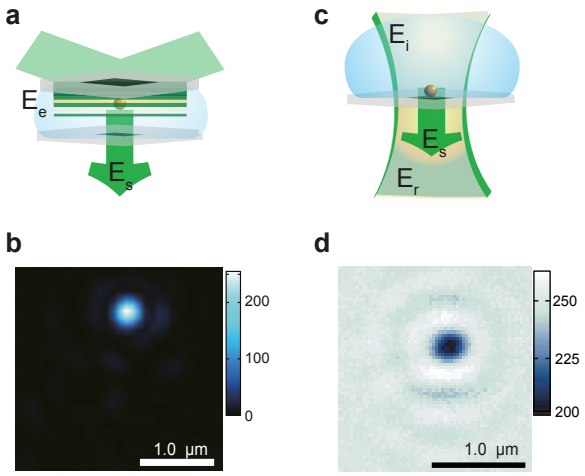


Figure 2.2: a) Illumination scheme for a pure scattering approach using total-internal-reflection darkfield-microscopy (TIRFDM). The particle is excited by the evanescent field produced by total-internal-reflection, resulting in a scattered field E_s. The scattered light propagating in the direction indicated is imaged onto a camera producing the image in b). The detected image appears as a bright spot on a dark background, shown in false colour. c) Illumination scheme for an interferometric scattering (iSCAT) approach. The objective collects light reflected from the glass-water interface together with the light scattered by the particle in the direction indicated. When imaged onto a camera, the detected image appears as a dip in intensity on a large, bright background, shown in d). Figure from [115]

together with the scattered light. Interferometric scattering detection was first demonstrated in cell biology by Curtis in 1964 [116], who named the technique Interference Reflection Microscopy (IRM). This method uses the reflection that occurs at the interface between the glass coverslip and water as a reference field, as illustrated in Figure 2.2c. A few key developments have been critical in increasing the sensitivity of this method, resulting in the specific implementation known as interferometric scattering microscopy, or iSCAT. In particular, iSCAT uses a coherent, monochromatic light source rather than incoherent, white light illumination, which improves the contrast. The spatial dimensions of the beam and level of coherence are important considerations in whether back reflections from

optics create interference fringes that are detrimental to the quality of the detected image. The choice of optics and mechanical components is also critical for ensuring that the microscope is stable and that sources of noise are minimised. These matters are discussed in Chapter 3, which outlines the procedure for constructing and aligning an iSCAT microscope so as to achieve optimal sensitivity. Advances in camera technology, such as increased full well capacities and frame rate have enabled combinations of sensitivity and speed that can visualise biological nano-objects in motion, with spatial precision close to molecular lengthscales.

When the coherence length of the illumination beam is at least as long as the distance between the particle and the coverslip, the scattered and reflected fields interfere giving rise to a signal at the detector that can be described by Equation 2.2.

$$I_{detected} = |E_r + e^{i\theta}E_s|^2 = |E_i|^2(r^2 + |s|^2 - 2r|s|sin\theta) \tag{2.2}$$

where r is the amplitude of the reflected field (r = $\sim$ 0.065 for the glass-water interface) and θ is the phase shift between the reflected and scattered fields measured at the glass coverslip, which depends on the height of the particle, the scattering phase of the probe, and the focus position of the incident light as described in Section 3.2.2. The sine function arises from the Gouy phase shift, $-\frac{\pi}{2}$, of the focused reflection at the camera. A particle within $\sim$ 100 nm of the coverslip appears as a dip in intensity on a bright background (Figure 2.2 d).

When the scattered field is much larger than the reflected field, as is the case for scattering particles greater than $\sim$50 nm in diameter, the interferometric scattering yields no advantage over pure scattering. On the other hand, when the reflected field is much larger than the scattered field, the pure scattering term is negligible compared to the interferometric term, and the detected intensity reduces to Equation

2.3:

$$I_{detected} = |E_i|^2(r^2 - 2r|s|sin\theta) \tag{2.3}$$

Defining the contrast as the difference in intensity in the presence of a scattering nano-object, divided by the background intensity, the scattering contrast can expressed as:

$$contrast = \frac{\Delta I_{detected}}{background} = -2\frac{|s|sin\theta}{r} \tag{2.4}$$

From Equation 2.4 it can be seen that the contrast is proportional to the scattering amplitude, the reflected field amplitude and the phase difference between the reflected and scattered fields. The reflected amplitude is determined by the sample, specifically by the difference in refractive index between the glass coverslip and the aqueous medium, and is therefore constant. Similarly for imaging a particle at a fixed height such as in a planar bilayer, the phase is also constant, in which case the contrast is determined by the scattering amplitude. In a medium of uniform refractive index, the scattering amplitude is a function of the particle size only, implying that regardless of the illumination intensity the contrast of a scattering label remains the same, thereby providing a means to identify labels of known sizes even in environments crowded with scattering objects.

Inspection of Equation 2.4 also reveals that the contrast of a small scatterer scales with the scattering amplitude, s, when detected interferometrically. On the other hand, in pure scattering detection, where the measurement is ideally performed over a zero-background, the contrast is simply the detected intensity, which scales as s^2. As the scattering amplitude, s, is proportional to the volume, or equivalently d^3 where d is the diameter, a reduction in particle size of 2 leads to an 8 fold reduction

in contrast for iSCAT, whereas the same decrease in size leads to a 64 fold reduction in contrast in pure scattering detection. This reduced size sensitivity presents a major difference in interferometric detection compared to both pure scattering and fluorescence approaches.

In theory it is possible to detect arbitrarily small scatterers using either dark field or interferometric approach, simply by increasing the number of photons to a point where the contrast of the object is higher than shot noise fluctuations. In practice however, there are additional sources of background light from reflections off optics in the detection path, resulting in a baseline light level that increases with the incident power. In iSCAT detection this baseline represents a small fraction of the (high) background and slightly decreases the detected contrast. In pure scattering, however, the baseline adds to a zero background, representing a large fraction of the total detected signal, hence reducing the available dynamic range of the camera. It is typically feasible to detect particles down to $\sim$ 40 nm in diameter by pure scattering methods, before dynamic range becomes the limiting factor. In contrast, nano-objects as small as a single protein have been detected using iSCAT [117, 118], demonstrating the intrinsic sensitivity of the interferometric approach.

Localisation precision vs incident power

Having established that iSCAT has theoretically unlimited sensitivity, it is useful to quantify the localisation precision that can be achieved for a specific exposure time, as a function of the incident power. The intensity of the reflected beam is 0.4% of the incident intensity, and the detected photon flux is roughly 10% of this intensity, being the product of the pixel fill factor (35%), the photoelectron quantum yield of the camera (30%) the transmission of the objective and other optics in the detection path (80%) where the values in parentheses are the efficiencies of the camera and optics in the setup built for this thesis. Based on these values, the iSCAT localisation

precision curves for gold nanoparticles with diameters of $\phi = 40$ nm, 20 nm, and 10 nm are displayed as bold lines in Figure 2.3, for a 100 μs exposure time . Data is also included for pure scattering detection of a $\phi = 40$ nm gold label (dashed red line), based on a state of the art experimental setup reported in the literature [119], and for a single emitter (dashed orange line), based on typical values of fluorescence quantum yield and excited state lifetime. All calculations assume the experiment is shot noise limited.

2.4 Intrinsic capabilities of scattering detection

2.4.1 Label-free imaging

The detection of light scattering offers a number of applications that are not possible using fluorescent labelling approaches. One immediate application is the detection of nanoscopic objects without the use of any labels, which is possible by virtue of the fact that any material with a different refractive index from its surroundings will scatter light. The first biological scattering objects to be detected without labels using iSCAT were virus-like particles of the Simian Virus 40 [120]. These 36 nm - diameter protein shells generate a comparable contrast to 15 nm diameter gold nanoparticles, and are easily detectable with a SNR of 30 at an exposure time of 10 ms. Subsequent iSCAT experiments have demonstrated the successful detection of proteins with molecular weights in the 10s of kDa range [117].

It is instructive to ask the question - what is the smallest protein that can be detected? Trends in the contrast of single proteins indicate a scaling with molecular weight, which is not surprising as the partial specific volume (the inverse of the density) of most proteins falls within a narrow range around a mean value of $\nu = 0.73\ cm^3 g^{-1}$, and hence the molecular weight is a rough approximation to the

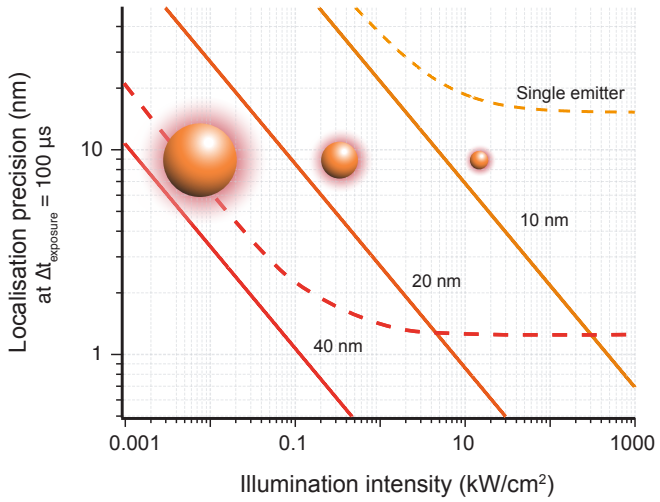


Figure 2.3: Localisation precision as a function of incident light intensity for iSCAT and dark field detection. The values are based on 532 nm illumination, with a typical detection efficiency determined by the properties of the camera and optics. The localisation precision curves for pure scattering detection and for a single emitter are limited by the detection dynamic range, and by optical saturation respectively.

volume. As such, for every factor of 2 decrease in the molecular weight of a protein, an increase in the number of photons by a factor of 4 is required to maintain the same SNR.

Given that our camera saturates at 2×10^5 photoelectrons per pixel, the resulting baseline noise is on the order of 0.3% root-mean-squared (RMS). This implies that a protein on the order of this contrast or smaller cannot be detected in a single frame. Such small scatterers can still be detected, however, by magnifying the image on the camera chip and/or by frame averaging. In the iSCAT setups constructed in our laboratory, the RMS noise decreases at the expected rate for shot noise limited imaging with frame averaging up to 60 ms, beyond which point the gain in SNR is no longer shot noise dominated. This places the minimum detectable size in the realm of 10s of kDa.

Beyond its ability to detect nanoscopic objects, iSCAT is also sensitive to refractive index variations in the glass coverslip itself, having a surface roughness on the order of a few nm, or a peak-to-peak contrast of 0.5%. These variations in height may be thought of as nanoscopic scattering objects, whose position is static.

2.4.2 Background subtraction

As the scattering signal from any object is stable over time i.e. not subject to photobleaching or blinking, it is possible to perform exact background subtraction (within the shot noise limit) of the scattering signal arising from all immobile objects. Using this principle, our group has detected single Myosin V proteins with a contrast of 0.18%, or less than half the peak to peak variation of the coverslip roughness and roughly one fifth that of the actin filaments on which the protein walks [118]. The median contrast values of each pixel were calculated over a time stack longer than the time taken for the myosin motor protein to move a distance several times the diffraction length, and subtracted from the raw images to produce a movie of only mobile components. Background subtraction can also be applied to distinguish between components that move with different characteristic timescales. For example the timescale of the motion of large scattering objects in the cell is much slower than the motion of a single protein, allowing over 90% of the background from the cell to be subtracted. These two cases are illustrated in Figure 2.4. A further application is to calculate the difference between images using a sliding time window, in order to detect arrival and departure of matter on a surface containing an arbitrary amount of scattering material, with a sensitivity that is as high as detection on a bare coverslip.

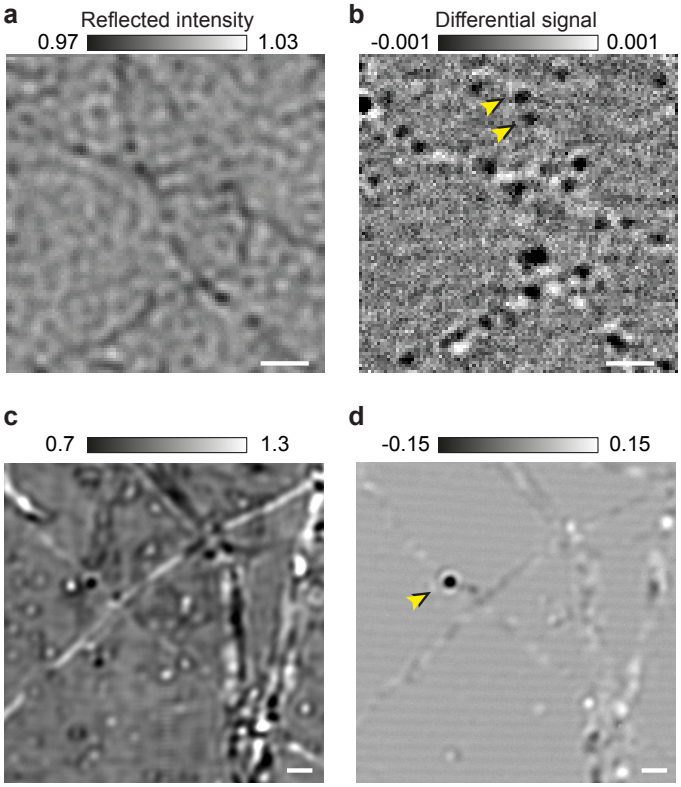


Figure 2.4: Illustration of original (left) and background subtracted (right) images. Top: a myosin V motor protein assay. In a) actin filaments appear as darker lines, on top of the glass coverslip roughness. In b) mobile myosin V proteins are visible on a shot noise limited background. Bottom: cultured hippocampal neurons. In c) single and bundled neurites appear as bright and dark filaments depending on their average height above the coverslip, and in d) a mobile gold particle label can be distinguished. As the cells move slowly, the differential image also shows blurring due to displacement of the cell. The arrows show two of the myosin proteins (top) and a $\phi = 40$ nm gold label (bottom). Scale bars are 1 μm.

2.4.3 Imaging molecular assemblies

Given the ability to detect the volume of a nanoscopic object based on its contrast, iSCAT is well suited to studying molecular assemblies of varying size. One application that is pursued in this work is the visualisation of phase-separated domains in a lipid bilayer. Other applications include label-free imaging of cytoskeletal

filaments such as microtubules [121] which are composed of monomeric units, visualising transitions in the structure of matter, such as the spontaneous formation of a bilayer from vesicles [122], and even determining rates of chemical reactions [123]. In each case, fluorescence labelling techniques cannot reach the same level of sensitivity, due to optical saturation, changes in intensity due to bleaching, and often the impossibility of labelling 100% of the units within an assembled structure.

In some of the cases above, it is useful to study the process of assembly and disassembly. Instead of subtracting the static background features from an entire movie stack, one can subtract the previous frame such that the resulting image shows the appearance or disappearance of matter from one frame to the next due to exchange of matter between the coverslip surface and the aqueous medium. If greater sensitivity is needed, frames can be averaged prior to performing subtraction. This method requires assembled objects to be static, and hence is not applicable to the dynamic work presented in this thesis, however it is nonetheless an interesting related application of label-free iSCAT with potential to elucidate membrane processes with very high sensitivity.

2.4.4 Localised heating around gold nanoparticles

When optically illuminated, gold nanoparticles generate heat, which is transferred to the surroundings resulting in a highly localised temperature rise. While many applications make use of the heating effect of gold nanoparticles for controlling temperature on the nanoscale, such heating is undesirable in tracking experiments as it can perturb biological dynamics. Quantitative knowledge of the amount of heat generated at typical illumination intensities is therefore important.

The maximum temperature rise around a gold nanoparticle can be calculated by evaluating the temperature at which the rate of heating is equal to the rate of

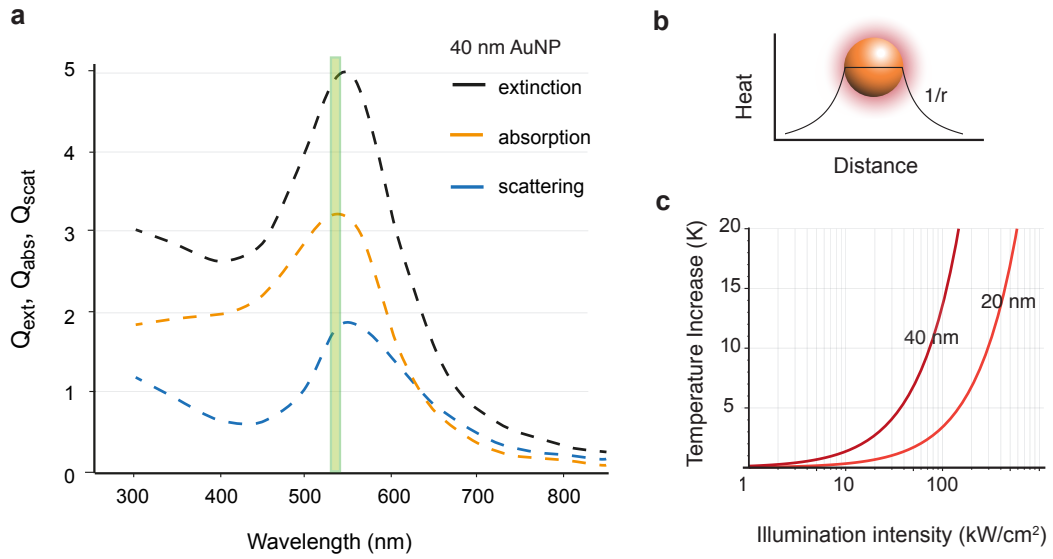


Figure 2.5: a) Calculated optical extinction, absorption, and scattering spectra for a spherical gold nanoparticle with $\phi = 40$ nm in water [124]. The green rectangle marks the plasmon resonance wavelength. b) Distance profile of temperature rise in the vicinity of a nanoparticle [125]. c) Maximum temperature increase on the surface of a single $\phi = 40$ nm and $\phi = 20$ nm spherical nanoparticle induced by absorption of incident light at 532 nm [125]

dissipation of heat energy to the surroundings [125]. Heating rates have been found experimentally to depends on the particle size- and wavelength-dependent absorption [126, 127, 124], shown for a $\phi = 40$ nm gold nanoparticle in Figure 2.5a (orange trace). Examination of the wavelength-dependence of the absorption coefficient reveals that absorption (and hence heating) is the highest at the plasmon resonance frequency in the range of 520 - 532 nm, where the scattering efficiency is also maximised. Illumination with red wavelengths results in comparatively lower absorption both in absolute terms and relative to scattering, suggesting that wavelengths above 600 nm are more suitable in applications where it minimising heating is essential.

In the current work, we perform tracking at up to 50 kHz using power densities of $20 - 30$ kWcm^{-2}, which corresponds to a maximum increase in temperature of

1.5 K for $\phi = 20$ nm gold, or 4 K for $\phi = 40$ nm gold at 532 nm. In Chapter 6 we image gold nanoparticles with 633 nm illumination, making use of the much reduced temperature rise compared to 532nm illumination [125]. In our experiments, we estimate a temperature rise of <0.4 K for $\phi = 40$ nm gold nanoparticles tracked at 20 kWcm^{-2}.

2.5 Outlook

The experimental difficulty of resolving small, transient structures remains the biggest challenge in understanding the organisation of the cell membrane. While diffraction limited optical microscopy remains a workhorse of cellular imaging, some information is intrinsically off-limits to this approach. For example, the detection of rare events or behaviours that vary in space and time require the ability to observe and track single molecules. In this regard, scattering detection has intrinsic advantages over fluorescence, as scattering offers theoretically unlimited spatiotemporal resolution and indefinite observation times, while also being intrinsically sensitive to refractive index variations which generate contrast without the use of labels. Interferometric scattering detection in particular allows scattering detection in the shot noise limit for arbitrarily small signals.

Chapter 3

Setup Construction and Characterisation

3.1 Microscope setup

A microscope was designed and constructed for the work in this thesis, including two iSCAT channels, an optional fluorescence channel and a focus stabilisation channel. The microscope is based on an inverted epi-fluorescence setup, where the sample is illuminated from below and the detected light is collected in the same direction. A high NA objective (Olympus PLAPON oil immersion 1.42 NA, 60× magnification) focuses the incident light onto the sample and collects the light reflected at the glass coverslip interface and the light backscattered by particles within the illumination region, as well as fluorescence from excited dye molecules, if applicable. Efficient separation of the incident and collected light in the two iSCAT channels was accomplished by using linearly polarised incident light together with a quarter wave plate immediately before the objective. The polarisation of the reflected light is shifted by $\frac{\lambda}{2}$ relative to the incident light, and separated by means of a polarising beam splitter. The fluorescence was separated from the

iSCAT beam paths and the incident excitation light by a dichroic mirror, and detected with the appropriate filters. Distinct wavelengths were used for each of the three imaging channels and the focus stabilisation channel, allowing beams to be separated by dichroic mirrors. Most of the work in this thesis was carried out on a setup using red wavelengths (638 nm, 662 nm) for the two iSCAT channels in order to minimise photodamage and heating of gold nanoparticles and blue (462 nm) excitation in the fluorescence channel. Fluorescence excitation was combined with the incident iSCAT beam path by reflecting off a 605 nm dichroic mirror. The fluorescence excitation and emission were separated by a 505 nm dichroic mirror, providing a fluorescence detection window from 505 - 605 nm, which encompasses the fluorescence ranges of GFP, YFP and a number of commonly used lipophilic dyes. The three imaging channels are illustrated in Figure 3.1 and described in greater detail in the following sections. Experiments described in Chapter 5 were carried out on a similar setup that used 532 nm illumination for the fast tracking channel, to excite gold nanoparticles close to the plasmon resonance frequency.

3.1.1 Lasers

Diode lasers were used in each of the imaging channels (λ = 462, 638, 662 nm) and the autofocus channel (λ = 405 nm). Lasers were mounted in copper or aluminium housing for heat sinking, rather than using cooling fans as the latter produce vibrations.

Diode lasers have the advantage of high output powers, availability in a range of wavelengths, and being compact and inexpensive. They are also particularly well suited to iSCAT imaging due to their relatively low coherence length, or temporal coherence. While a certain degree of temporal coherence is necessary for the scattered and reflected waves to interfere, it is ideal if the coherence length is not significantly greater than the distance between the scattering object and the cover-

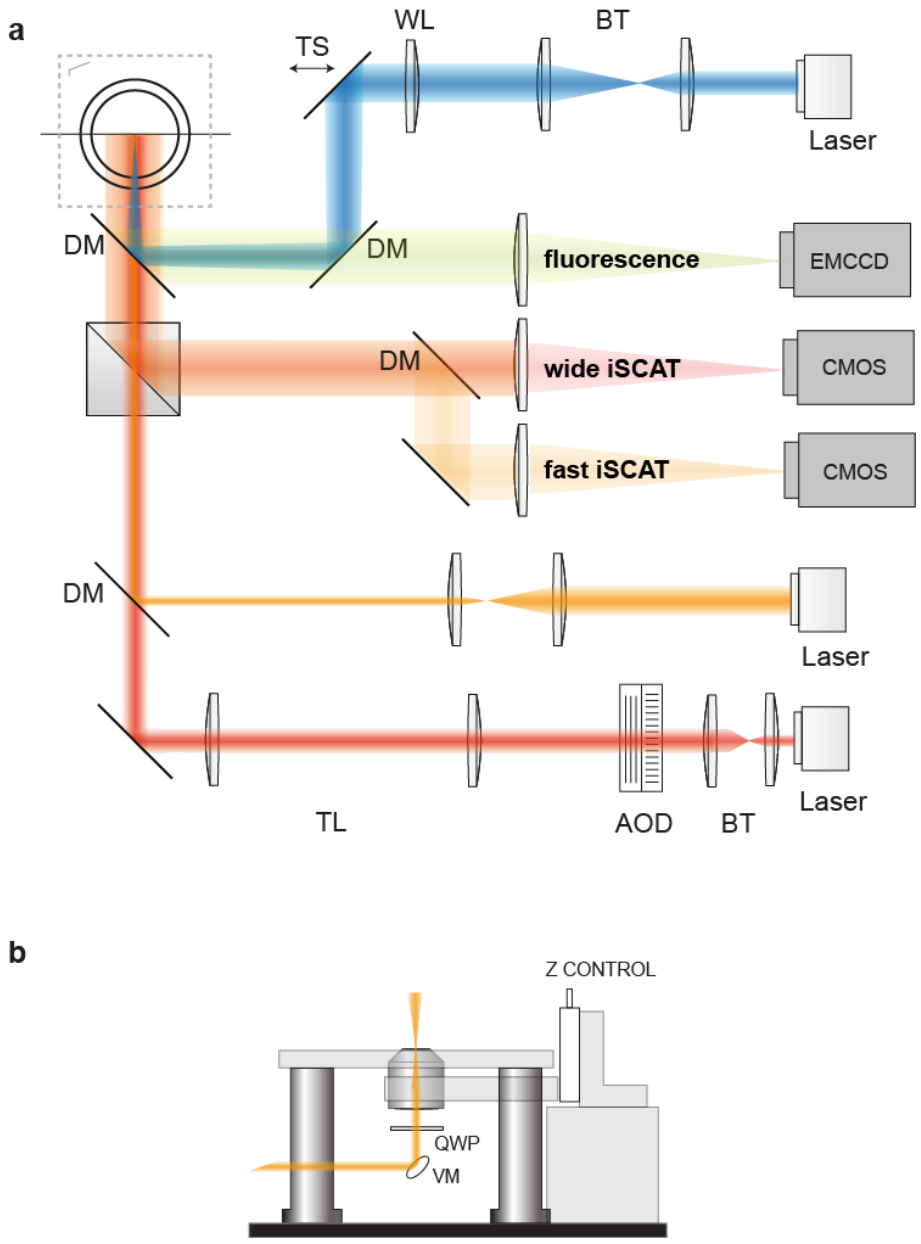


Figure 3.1: Schematic of the experimental setup, showing a) a top down view of the table and b) a sideways view of the region indicated by the dashed rectangle in a. The setup included two iSCAT channels for fast imaging (638 nm) and wide-field imaging (662 nm), and a fluorescence channel using TIRF illumination (462 nm excitation, 505-605 nm detection). An additional channel (which has been omitted for clarity) was used to stabilise the objective-sample distance, as described in Section 3.2.1. Abbreviations: PBS = polarising beam splitter; DM = dichroic mirror; BT = beam telescope; TL = telecentric lenses; WL = wide-field lens; TS = translation stage; AODs = acousto-optical deflectors; QWP = quarter waveplate (QWP); VM = vertical mirror.

slip, such that scattered or reflected waves above the focal plane do not contribute to the signal. The coherence length of diode lasers is typically only a few hundred microns, due to current fluctuations in the power supply which lead to small changes in output power and wavelength. High spatial coherence can also be deleterious in imaging applications due to the formation of speckle patterns from coherent interference of waves off nanoscopically rough optical surfaces. As various parts of the emitting area in diode lasers produce light independently, the lateral phase correlation is relatively low, and spatial coherence artefacts are not observed.

3.1.2 Cameras

As detectors in the interferometric channels, high-speed CMOS cameras (Photon Focus MV-D1024-160-CL-8) were used with a frame grabber (PCIe 1430 NI) allowing imaging at frame rates up to 70 kHz. The CMOS cameras were chosen for their versatility in the selection of region of interests, large full-well capacities (200 ke^-), and generally lower cost than their EM-CCD counterparts. Fluorescence images were recorded on an EM-CCD camera (Andor iXon3 860), with EM gain up to 300× and operation at a chip temperature of -80°C, providing high sensitivity and low thermal noise. For the focus feedback channel, an inexpensive CCD camera was used (Thorlabs DCC1545M). The beam was expanded over multiple pixels to increase the effective photoelectron capacity.

We employ two iSCAT channels such that one can be used for imaging a small area at high speed or high magnification and the other provides a large field of view of the sample. In both cases the frame time is the sum of the exposure time and the readout time, which scales linearly with the number of pixels. A 28 × 28 pixel region of interest, for example, has a 10 μs readout time. To compromise between achieving a frame rate and maximising the exposure time, we operate the camera with a 50% duty cycle (10 μs exposure time, 20 μs frame time) at 50 kHz. The

general rule for optimal localisation in particle tracking recommends an effective pixel size of approximately half the diffraction limit, i.e. about 100 nm in the visible [128], or a 3 × 3 μm area in the above example.

If imaging speed is not the primary concern, the detected area can be much larger. For example, an area of 10 × 10 μm can be imaged at up to 1000 Hz, or 100 μm at up to 100 Hz. Alternately, a higher magnification can be employed to collect more photons per diffraction limit area. For example, using a 10 nm effective pixel size the photoelectron capacity is increased by 1000-fold compared to a 100 nm pixel size, yielding 10-fold reduction in shot noise (scaling with $\frac{1}{\sqrt{N}}$) or equivalently a 10-fold increase in the signal to noise ratio. A quantitative estimate of the achievable SNR can be estimated as follows: when each pixel is filled to the full photo-electron capacity of 200 ke$^-$, shot noise fluctuations of $\frac{1}{2\times10^5}$ or 0.2% per pixel result. Increasing the magnification by a factor of 10 (e.g. from 100 nm pixels to 10 nm pixels) yields shot noise fluctuations of only 0.02% per effective 100 nm super-pixel after binning.

Experimentally the magnification was modified by placing an imaging lens at a focal length, f, away from the camera, the resulting magnification being given by $\frac{f\times m_{obj}}{f_{obj}}$ where the m_{obj} is the specified magnification of the objective (60×) using a lens of focal length f_{obj} = 180 mm. The value f_{obj} specifies the focal length where the aberrations are minimised, however we find that using focal lengths of different lengths does not have a significant effect on the contrast or shape of the PSF.

As there is electrical noise associated with reading the charge off the pixels on the chip, images with very low photons counts are dominated by this source of noise. Analysis by a previous group member determined that images are essentially shot noise limited for photon counts greater than 20% of the saturation level. As a rule of thumb, the illumination power density in each iSCAT channel was tuned so that the average photon count was 60-80% of the saturation level.

In all cases, detection paths were enclosed to exclude both stray sources of light and air currents. Cameras were mounted to the optical table at the end of a lever arm of 5 - 10 cm, which was found to significantly suppress vibrations from electronic equipment transmitted through the table.

3.1.3 Illumination approaches

Non-scanned illumination for fast imaging

For fast imaging, a small area was illuminated with high average power density by focusing a collimated beam onto the sample. A perfectly collimated Gaussian beam filling the back aperture of the objective yields a focused point-like spot with a diameter roughly equal to the diffraction limit, or 200 nm. A larger illumination area can be achieved by under-filling the back aperture, which we denote "slim-field" illumination to distinguish from wide-field illumination and point-like illumination. In this work high speed tracking experiments were performed with a collimated beam of $\sim$2 mm diameter, resulting in a FWHM of $\sim$5 μm at the sample, as illustrated in Figure 3.2 a. The ratio between the peak pixel intensity and minimum pixel intensity within the recorded region of interest was no more than 2, yielding comparable localisation precision at the edges and centre of the image. An output power of $\sim$6 mW was necessary to achieve a few nm spatial precision at 50 kHz, corresponding to a power density at the sample of 20-30 kWcm^{-2}.

The image quality in slim-field mode is determined by the intensity profile of the illumination beam, which should be smooth and constant over time. To this aim, the output of the 638 nm diode laser was cleaned and turned into a Gaussian-like mode by coupling into a single-mode fibre. This additionally served the role of transforming all beam instabilities due to laser pointing and mode hopping into intensity fluctuations, which can be accounted for by normalisation.

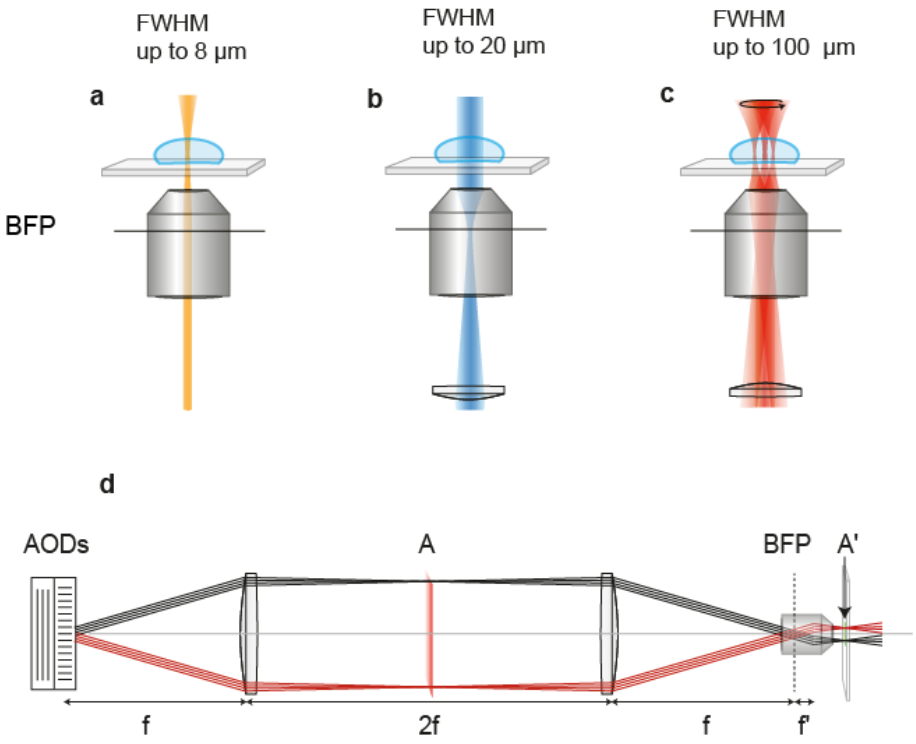


Figure 3.2: Schematic showing the illumination methods for a) the fast iSCAT channel; b) fluorescence channel and c) the wide-field iSCAT channel (showing only the final lens in the 4F relay system). d) The telecentric relay system used in the wide-field iSCAT channel. AODs = acousto-optic deflectors; BFP = back focal plane of the objective; A = area scanned with the AODs; A' = scanned area in the image plane.

Non-scanned wide-field imaging

For fields of view larger than approximately 8 μm FWHM, an alternate illumination approach is required. One option is to use Koehler illumination, where the beam is focused onto the back focal plane, resulting in the rays throughout the cross section of the beam passing parallel through the sample. This method is commonly used in wide-field fluorescence and other wide-field imaging techniques such as differential interference contrast and phase contrast, where it is advantageous that the plane of the light source is completely defocused at the image plane.

Koehler was used for the fluorescence channel to illuminate an area of $\sim$ 10 μm

FWHM, roughly equal to the field of view of the camera. Figure 3.2b illustrates the diameter of the fluorescence beam as it travels through the objective to become collimated at the sample. The epi-fluorescence configuration is shown for clarity though in practice, the excitation source was displaced laterally across the back focal plane of the objective to achieve total internal reflection illumination at the glass-water interface.

Koehler illumination yields even intensity across the sample, but is not feasible in iSCAT detection where the reflected beam is imaged, as interference from different parts of the beam results in high intensity fringes that significantly deteriorate the image quality.

Scanned wide-field imaging

An alternative to wide-field detection that is not subject to unwanted interference fringes is to scan a point-like beam across the sample. We use a pair of orthogonally-mounted acousto-optic deflectors (Gooch and Housego) arranged in a telecentric relay imaging system that is conjugate to the back focal plane of the microscope objective (Figure 3.2 d). Two AODs were scanned at different fixed frequencies much faster than the exposure time of the camera to produce even illumination in the recorded image. To ensure that the pattern scanned by the beam was the same for each image, the function generators were triggered at the start of each frame and scanned for a set number of cycles determined by the exposure time of the camera. Failure to synchronise the data acquisition resulted in time-varying beat patterns in the images caused by the drift in phase between the two orthogonal beam deflection units operating at different frequencies. The frame-grabber was used for external triggering of both the start of the camera exposure and the AOD scanning.

The AOD alignment was achieved in three steps. First, the collimated output from the laser was directed in a plane parallel to the optical table. Second, one AOD

was placed in the beam path and then the angle of the crystal element was adjusted so that the output of the first diffraction order was maximised to about 70% of the incident power. As diffraction is most efficient when the incident polarisation is parallel to the acoustic wave propagation, the laser was mounted such that the polarisation matched the AOD orientation. Third, the remaining AOD was positioned and its output power optimised by adjusting the angle of incidence between the face of the crystal element and the first order diffraction from the first AOD. The two adjustable mirrors were placed immediately after the AODs to compensate for the change in height and direction associated with the AODs, and thereby ensure that the non-scanned deflected beam travels in a plane parallel to the table. The main determinant of the image quality in the scanned channel was the diameter of the focused beam, as illumination diameters larger than 1 μm yielded interference fringes similar to those observed with non-scanned wide-field illumination. Adjusting the diameter of the collimated beam to 4-5 mm before entering the AODs was sufficient for eliminating such interference.

3.2 Construction of the microscope

Building an iSCAT microscope requires careful alignment of both the incident and detected beam paths. The microscope was constructed by setting up the slim-field channel first and aligning the other channels on top of the established beam path. The construction procedure consists of a preliminary rough alignment, followed by systematically adjusting the tilt and position of the incident beam with feedback on the camera, to ensure optimal alignment. For all additional channels, the incident beams were aligned along the established path and the camera and detection optics were placed as described for the slim-field channel.

Alignment of the iSCAT beam path

The procedure for defining the beam path and positioning the essential iSCAT optics is as follows:

1. Using either the collimated, fibre-coupled output of the slim-field laser, or a HeNe laser, the beam is reflected off two adjustable mirrors, so that the output after the two mirrors travels in a straight line along the length of optical table, and level with the plane of the table.

2. The polarising beam splitter (for separating illumination/detection paths) and dichroic mirror (for separating iSCAT/fluorescence paths) are added along the beam path in that order. Any deflections introduced by the two optics are corrected for with the two adjustable mirrors, to ensure a straight and level path after the final optic.

3. A vertical mirror is placed after the dichroic mirror such that the laser beam is deflected by a 90 degree angle from the plane of the table towards the ceiling. For rough alignment, the laser is blocked and an assistant is called upon to hold a string at ceiling height, while a weight is attached to the end of the string and held directly above the vertical mirror. The string is manually translated across the ceiling to find the position where the weight does not swing when released. The assistant draws a target on the ceiling, which defines the vertical beam path. Unblocking the laser, the angle and rotation of the 45 degree mirror is adjusted so that the beam hits the target on the ceiling.

4. A long focal length lens (e.g. f = 750 mm) is placed at distance f from the position where the objective back focal plane will be (in our setup, this is 4 cm above the 45 degree mirror) and the height and position are adjusted to ensure that the beam is centred on the same spot on the ceiling (with a slightly larger spot size due to divergence of the beam).

5. The objective is mounted in a holder that is attached to the z adjustment stage, and the whole unit (stage + objective) is placed above the 45 degree mirror, and translated until the beam - now collimated - hits the target on the ceiling. Once the stage is in the correct place, it is carefully screwed into the table, taking care to apply even pressure to all mounting points so that no tilt is introduced.

6. An iris is placed immediately before the 45 degree mirror, and another is placed a short distance along the path of the (weak) reflection of the incident beam off the PBS. A target is also placed at a long distance along this beam path. This provides two points of reference defining the beam path up to the PBS, and another two points of reference defining the path between the PBS and the objective (if we include the target on the ceiling), which allows the correct beam path to be reinstated in case of any changes in alignment, for example due to relaxation of optics.

7. The sample stage is screwed onto the table, such that the objective is centred within an aperture on which the coverslip rests. Immersion oil is applied to the objective and a coverslip is placed on the sample stage, then a quarter waveplate is mounted between the 45 degree mirror and the objective such that the returning light can be visualised after the PBS by placing a piece of paper in the beam path. The focus on the objective mount may need to be adjusted to collimate the returning beam.

Fine tuning the alignment

At the completion of these steps, the returning beam has a symmetric, Gaussian shape, and focuses concentrically when the sample stage on which the coverslip sits is moved up and down. If this is not the case, it is likely that the coverslip is not flush with the sample stage, possibly due to an air bubble in the oil.

To finely tune the alignment, the detection path is set up by adding a camera at the desired distance from the PBS (the distance must be long enough such that a lens of focal length f mm can be later inserted). As the PBS may slightly deflect the beam path from the plane of the table, we use a single adjustable mirror to ensure that the path after the mirror is parallel with the table, and hits the camera perpendicular to the chip. The height of the camera is adjusted such that the beam hits the centre of the camera.

The position of the beam is then observed on the camera as the sample stage focus is moved up and down. Any small displacement in position can be corrected by adjusting the x and y tilt on one of the adjustable mirrors (placed in step 1) until the detected beam position remains constant when the stage is moved up and down. This adjustment should not produce a noticeable displacement of the beam path from the targets. At this point, the height of the stage is adjusted so that the returning beam is collimated, and a lens is placed at roughly the correct focal distance from the camera, and the exact position is translated until the reflected beam is focused to a minimal spot size on the camera.

Troubleshooting

If the fine alignment step requires significant adjustment, and the resulting beam path deviates noticeably from the initially marked targets, this most likely indicates that either the stage or the objective is not parallel to the table. If the stage is not adjustable, tilt should not be a significant. In any case, the tilt of the stage can be corrected in each dimension by iteratively translating a coverslip over several mm and correcting the tilt of the sample stage. determining whether there is a change in focus. The focus can be determined by spin coating the coverslip with gold nanoparticles, or simply using a coverslip that has not been cleaned.

If the objective is not aligned with the vertical axis, the position of the objective

will have been set incorrectly to compensate. The angle of the 45 degree mirror can be adjusted such that the beam travels along the objective axis by removing the objective and resting a high quality (flat) mirror on the rim around the objective aperture. The incident beam will be reflected by the mirror and can be visualised on the front side of an iris placed along the illumination beam path. If the objective mount is tilted, the returning beam will not overlap with the incident beam. The tilt and rotation of the 45 degree mirror are adjusted until the incident and returning beams exactly overlap. Then the alignment proceed is followed from step 4 onwards.

3.2.1 Stabilisation of the objective-sample distance

Focus stabilisation was implemented by coupling the output of a 405 nm diode laser onto the fluorescence excitation beam path with a 425 nm dichroic mirror. A lens and a translatable mirror were added before the dichroic to focus the beam onto the back focal plane and to translate the position of the beam until the totally internally reflection beam returned along the path. A half mirror was placed in the returning beam path, between the dichroic mirror and the translation stage, and detected on a CCD camera (Thorlabs DCC1545M). A cylindrical lens was inserted to expand the vertical dimension of the beam to fill the chip.

The lateral position of the beam changes linearly as a function of the distance between the coverslide and the objective, and can be used to determine the position of the slide (i.e. the z position) relative to the desired focal plane. The centroid position was calculated and converted to a voltage that was fed to a piezo controlled stage (Thorlabs, NFL5 Series NanoFlex), allowing z stabilisation within $\pm$ 2 nm of the target at 20 Hz. The accuracy with which the z position could be determined was optimised by expanding the beam over the full chip in the dimension perpendicular to lateral motion, thus increasing the number of photons detected beyond the saturation level of a single pixel.

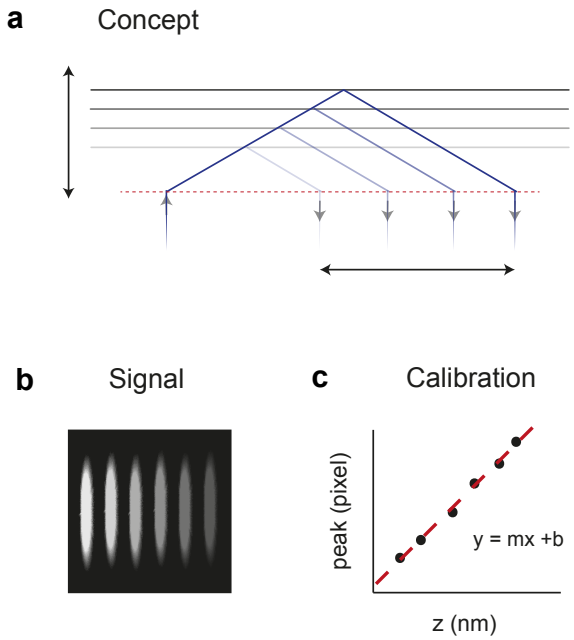


Figure 3.3: a) Changes in the distance between the objective and the coverslip result in lateral displacement of a totally internally reflected beam. b) The beam is imaged onto a camera, using a cylindrical lens to expand the beam in the dimension perpendicular to the lateral motion. c) The centroid position of the beam is measured while stepping the objective position with a piezo driver, and the resulting data is fitted with a linear function to generate a calibration.

3.2.2 Calibration of tracking in the axial dimension

In many biological situations it is desirable to be able to track molecules in three dimensions. With iSCAT it is theoretically possible to achieve axial localisation precisions equal to or better than the lateral precision [129] as information about the z position is encoded in the detected contrast. In this way iSCAT is analogous to a Michelson interferometer with two interfering beams that travel along the same path, wherein the detected intensity is dependent on the differential pathlength.

An iSCAT microscope differs from this simple case in that both the reflected field and the scattered field have an additional Gouy phase component as a result of passing through a point of lateral confinement. The Gouy phase shift arises when a beam

passes through a focus, causing the phase to shift by $-\pi$ radians compared to plane or spherical wave travelling the same distance. The rate of the Gouy phase shift of the incident beam is given by $\phi^G(z') = -tan^{-1}(\frac{\lambda}{\pi\omega_0^2}z')$ where ω_0 and z' refer to the $\frac{1}{e^2}$ beam radius at focus and the position of the sample relative to the focus ($z\prime = 0$), respectively. For the scattered field, a phase shift of $+\frac{\pi}{2}$ develops, with positive sign arising from the inverse phase evolution from a point particle compared to a point aperture or focus. In the far field, it can be shown that the difference in Gouy phase between the reflected and scattered fields is given by $\Delta\phi^G(z') = \pi - tan^{-1}(\frac{\lambda}{\pi\omega_0^2}z')$ [130].

The scattered field acquires an additional phase shift relative to the incident electric field, related to the oscillation of the induced dipole. The scattering phase, ϕ_{scat}, can be calculated from the complex valued polarisability, α, of the gold nanoparticle label by the relation $\phi_{scat} = tan^{-1}\frac{Im(\alpha)}{Re(\alpha)}$. The expression for the total phase difference is therefore a sum of the phase difference due to the optical path length, the relative Gouy phase evolution of the scattered and reflected beam and the scattering phase. The latter two terms contain a number of parameters that need to be experimentally determined, including the scattering phase and the beam waist of the incident beam. One could envision carrying out a calibration in which the contrast of a particle is measured as the particle is moved to various heights above the coverslip. In practice, this presents a considerable experimental challenge due to the difficulty of controlling the z position of a particle over a range of a few 10s of nm.

One approach that has been applied to determining the Gouy phase and scattering phase parameters is to measure the contrast of gold nanoparticles of various sizes (and hence centre z positions) as a function of the objective-coverslip distance. This approach showed promise but showed a systematic deviation between fits and measured data, potentially due to differences in the scattering phase as a function of particle size. Another as yet untested approach is to use spacers of known

height to position gold nanoparticles at various z locations, however the effect of the refractive index of the spacer material on the optical path length difference and the scattering amplitude may require a complicated analysis. Devising and carrying out an accurate experimental method to calibrate the Gouy phase would be a highly valuable contribution to iSCAT microscopy.

In the absence of a calibration to determine z from the iSCAT contrast, we have used the fluorescence PSF to determine the z coordinate. This approach is simpler as the fluorescence PSF depends solely on the distance between the particle and the objective. A number of fluorescence detection methods have been developed in the literature and include multiplane detection [131, 132, 133], astigmatic focusing [134, 135, 136] and PSF engineering [137, 138]. For ease of implementation we have used astigmatic focusing, in which a cylindrical lens is inserted into the detection path such that the ratio of the x and y dimensions of the PSF varies depending on the height of the emitter. A calibration was acquired using fluorescent beads, by stepping the piezo that controls the sample-to-object distance and measuring the FWHM in the x and y dimensions. The calibration data is shown in Figure 3.4, using a 1000 mm cylindrical lens inserted approximately 200 mm in front of the camera chip.

3.2.3 Data acquisition and visualisation software

Data was acquired from using home-built LabVIEW software written by a previous member of the group. In brief, the two iSCAT cameras were run at specified frame rates and viewed by sampling images at 20 Hz. For high speed imaging at frame rates above 1 kHz, reading individual frames sequentially becomes unstable, so images were written to a ring buffer with a typical size of 200 frames, and transferred to RAM in blocks of 40 frames. At the completion of the specified number of frames, the data was written to the hard drive. Saving initially to RAM allows for much

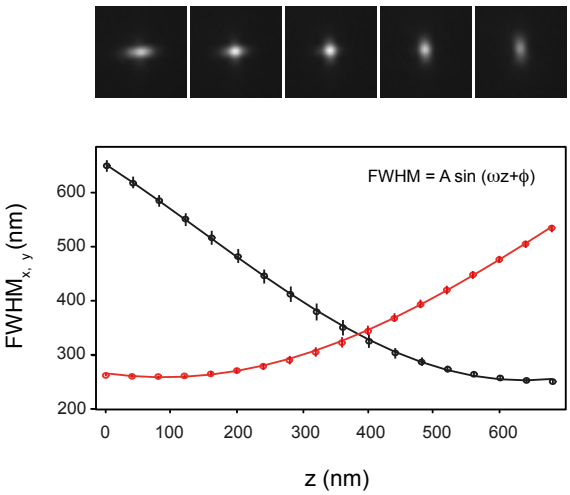


Figure 3.4: Calibration of particle height based on astigmatism of the fluorescence PSF. Data was recorded with 580 nm fluorescent beads, at 100 fps, waiting 2 s per step. The piezo on the sample stage was fed a voltage corresponding to a step size of 40 nm. Imaging of the reflected TIRF beam on the camera used for autofocusing confirmed even step sizes and negligible drift. A sine function was fit to each curve using a nonlinear fit method with minimisation of square errors, to determine parameters A, ω and ϕ.

faster data transfer than writing each frame to the hard drive, however it limits the filesize to 1.2 GB on our computer. As available RAM is commonly fragmented, automatic consolidation of contiguous segments was performed prior to recording.

The visualisation software contains options for collecting and applying various backgrounds in real time. A dark count background was collected prior to recording, and was subtracted from every frame to account for variable pixel dark offset levels. We divide the background subtracted image by a flat field image to remove inhomogeneities in intensity. The flat field image was obtained by collecting 100 images while manually moving the sample stage, and calculating the median value of each pixel. Movement of the sample ensures that only features arising from the illumination beam and the detection optics are subtracted.

3.3 Data fitting

3.3.1 Nanoscopic localisation and tracking

The data fitting procedure consisted of a pre-processing background removal step, followed by detection of potential particles, partitioning of the image into regions around each particle and localisation of the centre of each particle using a 2D Gaussian function using a Levenberg-Marquardt nonlinear fitting algorithm. The preliminary background subtraction step makes use of the fact that sources contributing to constant scattering signal can be removed by subtracting the median value of each pixel through the sequence of recorded images. This results in a stack of images where the only deviations from the flat, reflected light intensity arise from mobile scattering particles, and any motion of the sample. For the supported lipid bilayer experiments in Chapter 5, residual sample motion is undetectable and particles can be recorded on a shot noise limited background. In experiments on cells (Chapter 6) and in droplet bilayers (Chapter 4) a small background remains after median stack subtraction.

After subtraction of static features, particle detection and fitting was performed using a home-made program written in LabVIEW, described in reference [139]. In brief, particle detection was performed by finding the superposition of local maxima, with pixels exceeding three times the standard deviation of pixel values. Candidate particles were then segmented into regions of interest corresponding to 1×1 μm^2, which for a magnification of 100× corresponded to 9×9 pixels (effective pixel size of 106 nm). A two-dimensional Gaussian function with 6 parameters Gaussian fit parameters (amplitude, x, y, σ_x, σ_y, offset) was then fit to each segmented region and candidate particles satisfying the contrast upper and lower bounds were used as input parameters for the consecutive frame. Poor localisations were rejected on the basis of their FWHM and eccentricity. Here the eccentricity is defined as $\sqrt{1-(\frac{\sigma_{lower}}{\sigma_{higher}})^2}$

where $\sigma_{lower/higher}$ refer to the lower and higher of the standard deviations of the PSF in the x and y dimensions.

In most of the experiments in this thesis, the density of gold nanoparticle labels, or unlabelled nano-objects, was low enough that trajectory linking was trivial and could be performed by defining a region of interest containing the same particle and no other particles for the entire recorded image sequence. When higher densities occurred, particle trajectories were reconstructed using a greedy algorithm that minimized the distance between detected particle positions in consecutive frames. Tracking experiments on neurons were complicated by the series of frames where the particle could not be detected. To connect trajectories in the case where frames were missing, a modified algorithm was written that connected segments if the distance between the positions was less than $10\times\mathrm{D}\times\mathrm{m}$, where D is the average frame to frame displacement, m, is the number of "missing frames" between successful localisations, and the value 10 was the maximum value found to correctly assign links while avoiding incorrect linking.

3.4 Characterisation of setup performance

3.4.1 Optomechanical stability

As we use iSCAT to measure small nanoscopic motion, it is critical that the microscope is mechanically stable. For this reason, the microscope was constructed on an optical table with active stabilisation and all power sources and the computer were mounted off the table and where necessary, isolated from the floor by vibration damping material. To quantify the stability, we recorded a single immobilised particle on a coverslip and determined the position of the particle in every frame. To minimise localisation precision error, we used a $\phi = 40$ nm gold

nanoparticle which gives a high contrast.

Figure 3.5 shows the measured x and y position of the particle, the localisation error, and a Fourier transform of the displacement in x and y. Examining this data we can confirm that there is no detectable drift in x or y over the timescale of the measurement (1 second). The largest vibrations in the x and y dimension have amplitude <0.6 nm RMS and occur in the frequencies between 100-140 Hz. As this value is typically much smaller than the localisation error for the work in this thesis, we can disregard the effect of vibrations in determining the position of tracked particles.

Defining the localisation accuracy as the standard deviation in the position of an immobilised particle, a $\phi = 40$ nm gold particle illuminated at 638 nm has an error of 1.5 nm in x and 1.1 nm in y, or an average of 1.3 nm. The localisation accuracy is slightly poorer in the x dimension than the y dimension, due to vibrations coupling more strongly in the x dimension. This is likely due to mounting of the objective on a single lever arm, with the greatest amplitude of vibrations being along the imaging x dimension. The same measurement of $\phi = 40$ nm gold and $\phi = 20$ nm gold nanoparticles at 532 nm illumination yields an average localisation error of 0.7 nm and 2.2 nm respectively, where the accuracy is higher due to the higher contrast near the plasmon resonance.

3.4.2 Localisation accuracy

The distribution in the measured position of a static particle is equivalent to the localisation accuracy in an experiment which is shot noise limited, such as tracking on supported lipid bilayers in Chapter 5. A number of factors related to the sample can potentially deteriorate the localisation accuracy, including: the presence of background noise that is not subtracted by the median stack; changes

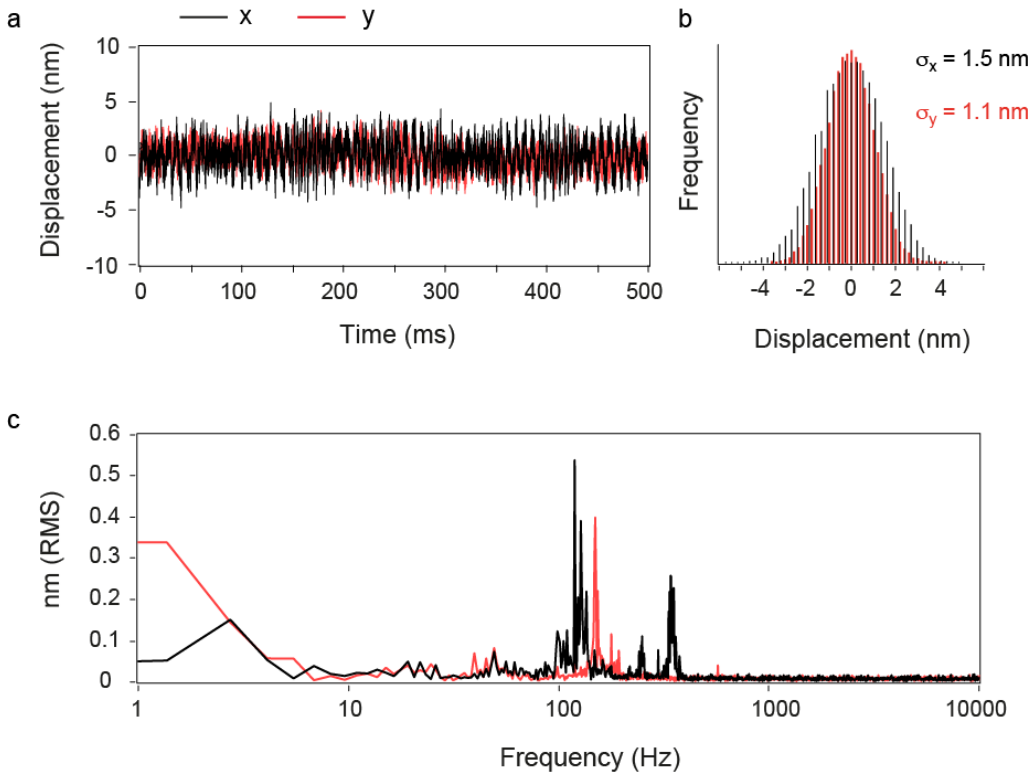


Figure 3.5: a) x and y coordinate of an immobilised $\phi = 40$ nm gold nanoparticle imaged at 20 kHz. b) Distribution of displacements from the mean position. c) Fourier transform of x(t) and y(t).

in the contrast of the scattering object (for example, due to growth or dissolution of a nanoscopic membrane domain) or motion in the z dimension; and changes in the PSF which also occur as a result of motion in z. The localisation error can be estimated on a frame by frame basis using the covariance matrix, which is calculated as a byproduct of the nonlinear fitting process. The covariance matrix provides a means to determine how variability in each of the fit parameters propagates to the error between the Gaussian function and the measured data. The error in each parameter, a_i may be defined as $\sigma(a_i) = \sqrt{C_{i,i}MSE}$ where C is the covariance matrix and MSE is the mean square error, which provides an estimate of the noise variance in the signal. Mathematically the MSE is calculated as $MSE = \sum_{k=1}^{n} \frac{(x_k - y_k)^2}{n-m}$, where n is the number of data samples (i.e. pixels in the

fitted region of interest), m is the number of parameters, x_k is the measured intensity and y_k is the fitted intensity of the k^{th} pixel. As systematic differences between the shape of the PSF and a 2D Gaussian also contribute to the discrepancy between the fit and actual data, this method overestimates the true localisation error.

Typical distributions of localisation errors for the experiments in Chapters 4 and 6 are shown in Figure 3.6. The error distribution for detection of $\phi = 40$ nm gold on neurons is relatively wide, reflecting the variation in contrast (and FWHM) with the height of the particle above the coverslip. In the data shown, the distribution is bimodal as the particle is predominantly located at one of two distinct heights. For nanoscopic membrane domains, the error depends on the contrast of the domain, which varies with the volume of scattering material, or equivalently with the radius of a domain. We would expect the localisation error to scale inversely with the contrast. This scaling, however, assumes that the localisation error is solely determined by the SNR. If the PSF deviates slightly from a 2D Gaussian, however, the estimated localisation error is non-zero, even in the case of infinite SNR. This minimum "error" due to the non-Gaussian PSF shape is responsible for the sub-linear increase in localisation error that we measure as a function of nanodomain contrast.

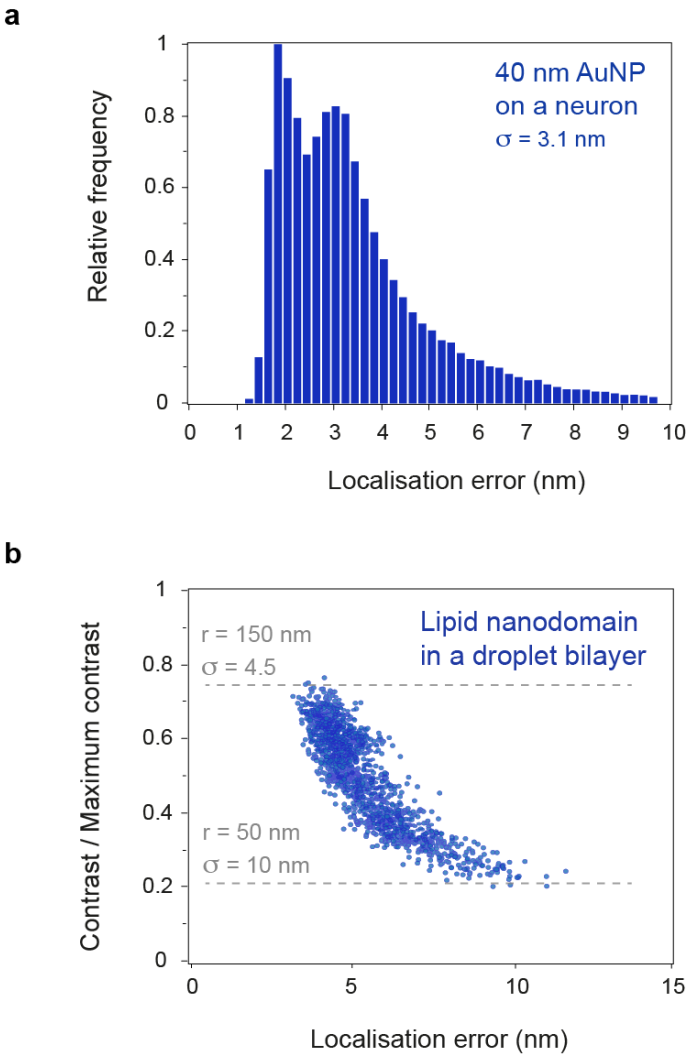


Figure 3.6: a) Localisation error distribution for a typical trajectory of $\phi = 40$ nm gold on the distal segment of an axon. b) The localisation error for nanodomains depends on the contrast of the domain. Localisation errors are shown for domain sizes ranging from the diffraction limit (150 nm radius) to the smallest domain (50 nm) that can be detected with a minimum SNR of 3.

Chapter 4

Label-Free Imaging of Lipid Nanodomains

4.1 Introduction

Since the introduction of the lipid raft hypothesis, the exact nature and dynamics of these nanoscopic objects has been highly controversial. The current definition of rafts as small (5-200 nm) and transient domains says more about the technical barriers confronting efforts to observe and study rafts, than it does about the properties of rafts themselves. While raft formation is thought to be driven by phase separation of the lipid components, many questions remain about the size of such rafts, the forces responsible for their formation and the time scales of growth, fission, merging and diffusion.

Before examining the dynamics of nanoscopic domains, we first describe the energetics that can lead to phase separation in mixtures, such as lipid membranes.

4.1.1 Phase separation in mixtures

A phase is a region of space with physical properties that are everywhere uniform. A mixture of components may either exist in a single-phase state or in a state that contains two or more phases (with a maximum number of phases of $N-2$ where N is the number of components) [140]. The equilibrium state of the system is determined by a balance of enthalpy and entropy, as given by the Gibbs free energy.

$$\Delta G = \Delta H - T\Delta S \tag{4.1}$$

To illustrate how the enthalpy and entropy determine the degree of mixing, we consider a simple system of two species, A and B, which are initially separated by a barrier, analagous to the example presented in [141]. If the barrier is subsequently removed, does mixing occur?

First we consider the case where 'like' species prefer to interact, such that the average interaction energy between like molecules A,A and B,B is lower than the interaction energy between unlike molecules. We write this case as $\frac{H_{A,A}+H_{B,B}}{2} < H_{A,B}$.

From enthalpy considerations alone, we would expect that the region of A remains together, and so does the region of B. The probability of this occurring, however, is much lower than a randomly mixed state, i.e. entropy favours mixing. The final state depends on entropy gain from mixing relative to the difference in enthalpy between $H_{A,B}$ and the average of $H_{A,A}$ and $H_{B,B}$. If $H_{A,B}$ is extremely unfavourable, it is possible that the two regions remain separate into a two phase system.

If $H_{A,B}$ is only somewhat higher than $H_{A,A}$ and $H_{B,B}$, or if the temperature of the system is high (yielding a large entropy term, $T\Delta S$), the two species may partially mix, resulting in a two phase system of mostly A and mostly B. If the temperature

is so high that the entropy term dominates, random mixing will be seen, resulting in a single phase system.

We now imagine that $H_{A,B} < \frac{H_{A,A}+H_{B,B}}{2}$ and that,as in the previous case, the entropy term makes a significant contribution to the free energy. Then, in order of increasing difference between the two sides of the equation, we would see a system that is: randomly mixed, more than randomly mixed, and finally a checkerboard pattern (with the maximum number of A and B interactions).

In biological membranes, there are hundreds or thousands of lipid species, with the difference in interaction energies being very small in many cases [142]. Furthermore, certain lipids have preferred stoichiometries, for example sphingomyelin and cholesterol have been shown to adopt stoichiometries of 2:1 [143, 144]. While the complexity of lipid interactions leads to potentially hundreds of phases, interestingly only two phases - a liquid ordered phase and liquid disordered phase - are observed in vesicles that are extracted from native membranes [145]. It is important to note, however, that such vesicles are formed by chemical treatment of the membrane, which removes a considerable fraction of the protein content and possibly alters the remaining lipid and protein species. Whether these membrane extracted vesicles necessarily represent the phase behaviour of live cells is not known.

4.1.2 Macroscopic phases vs domains

In the example above, we have assumed that there is an energy cost along the boundary region between two phases. For example, assuming like-like interactions are favoured and we have a state consisting of two phases - pure A and pure B - those phases will exist as two macroscopic regions. Or, if entropy and enthalpy compete, some lipid A will mix into the bulk region of lipid B and vice versa, but

the system will still have two macroscopic phases (phase 1 = mostly A, and phase 2 = mostly B) separated by one boundary.

We now imagine that the boundary energy is comparable to the interaction energy between A and B. In this case, it can be entropically favourable for the system to exist with small regions of phase A inside phase B, or vice versa. These regions, which we call microdomains or nanodomains, depending on their diameter, have the same properties as the bulk phases A and B. Such properties include the composition, the conformational freedom of lipid tails and also the bilayer thickness. Extrapolating this situation to the lipid composition of the cell, phases A and B will each be composed of a mixture of lipids. The dynamics and energetics of such systems where boundary energy is low are modelled in a recent paper by Frolov [146], the results of which we use in this chapter.

4.1.3 Current methods for detecting micro- and nano-domains

Fluorescent dye labelling approaches have provided the most promosing methods for observing lipid domains. The motion of entire domains can be directly visualised using fluorescent labels that preferentially partition into a specific phase [40, 147, 42, 148], an approach that has been successful for micron-sized domains, but inevitably fails on the tens to few hundreds of nanometers scale due to limitations in phase specificity, the limited residence time of a label, and the achievable optical resolution. The fluorescent probe is itself an additional component that can perturb phase behaviour, either directly, or through photo-oxidation [43, 149], and presents a particular concern at the high concentrations required for sensitive detection of small domains. An alternate approach is to use environment sensitive dyes, which report on phase separation regardless of the domain size [76, 77, 78, 80]. Even spatially resolved methods, however, do not offer temporal

resolutions sufficient to study the dynamics of individual domains. As such, we have dynamic information on large domains, and static information on small domains, but no dynamic information on nanodomains, even in artificial systems.

An alternate approach to detecting the emission of added fluorescent dyes is to detect intrinsic differences in how the ordered and disordered phases interact with light. The refractive index, for example, is an ideal target for iSCAT microscopy, as it relates to the contrast of an object. iSCAT is sensitive to very small changes in refractive index, down to the level of a single unlabelled protein in solution [118, 117]. Furthermore, the achievable time resolution with iSCAT is far superior to fluorescence imaging methods, as described in Chapter 2. We know that the phases in bilayer membranes have different refractive indices, as this property has previously been exploited to detect lipid domains, without labels, via the method of optical ellipsometry [150]. Unlike optical ellipsometry or other label-free techniques, iSCAT is inherently a spatially resolved technique, and hence this method provides a viable alternative to fluorescence imaging, while at the same time circumventing the limitations and potential artefacts of fluorescent labelling methods.

4.2 Materials and methods

Model lipid compositions: The phase behaviour caused by the diverse lipid composition in cell membranes can reproduced with simple model membranes containing only three lipids - a high melting temperature (T_m) lipid, a low T_m lipid and cholesterol - which form phase separated lipid domains across a wide range of biologically relevant cholesterol concentrations [151]. Commonly used low-T_m lipids include singly or doubly unsaturated glycerophospholipids. High T_m lipids used in model membrane studies typically include saturated glycerophospholipids

or sphingolipids. The difference in properties between high and low T_m lipids largely determines the line tension of domains, and can be selected to give macroscopic of nanoscopic domains. For example, membranes formed with biologically abundant low-T_m lipids, such as 1-palmitoyl-2-oleoyl-sn-glycero-3-phosphocholine (POPC) or 1-stearoyl-2-olyeoyl-sn-glycero-3-phosphocholine (SOPC), yield nanometer-sized domains that can be detected via FRET [152], fluorescence anisotropy [153], electron spin resonance methods [154] and small angle neutron scattering [73]. On the other hand, strongly perturbing low T_m lipids, such as 1,2-dioleoyl-sn-glycero-3-phosphocholine (DOPC) or 1,2-diphytanoyl-sn-glycero-3-phosphocholine (DPhPC) are often used to generate micron-sized domains which are easier to study optically as they can be directly visualised with fluorescent dyes [155], [156].

We used various combinations of high T_m and low T_m lipids to yield bilayers with the desired phase(s) and line tension. The structures of all lipids used in this chapter are shown in 4.1. DPhPC, DOPC, POPC, bSM, and Chol were obtained from Avanti Polar Lipids. The carbocyanine lipid analog, DiI-C18 was obtained from Invitrogen. ATTO-488 DPPE was obtained from ATTO-TEC Lipids and used without further purification, dissolved in chloroform at 50 mg mL^{-1} and stored at -20 °C until use. All other reagents were obtained from Sigma-Aldrich.

Droplet Interface Bilayer Formation: We employ Droplet Interface Bilayers (DIBs) as an artificial membrane model with phase-separated lipid mixtures, shown in 4.2. DIBs are formed at the interface between two lipid monolayers, surrounding an aqueous droplet and a planar hydrogel film respectively. DIBs are robust, long-lived, defect-free, show unrestricted diffusion, and are compatible with high resolution optical microscopy [157]. [158, 157].

DIBs were prepared by DPhil student John Danial, following the protocol previously reported by the Wallace group [159]. Briefly, 400 nl droplets of 90 mM

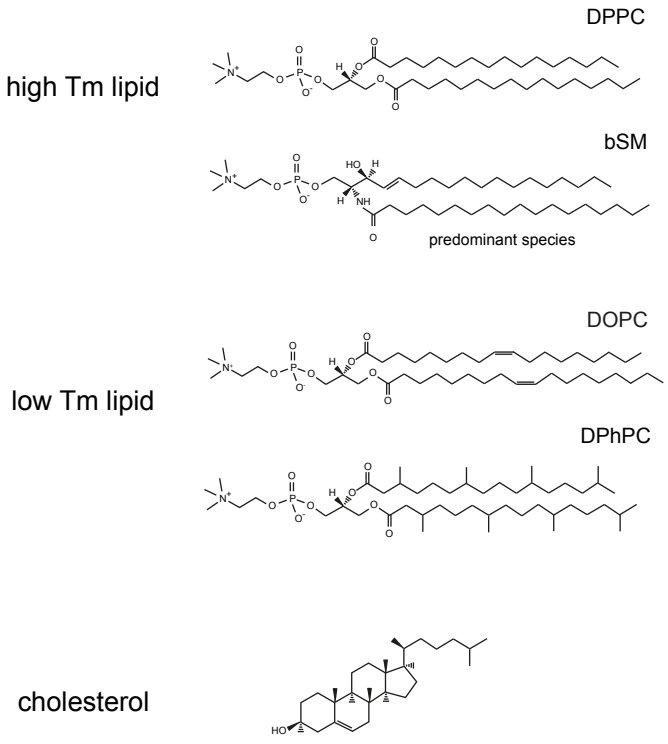


Figure 4.1: Structures of lipids used to create phase separated mixtures in DIBs.

4-(2-hydroxyethyl)-1-piperazineethanesulfonic acid (HEPES) were incubated for 40 minutes in a solution of the required lipids in hexadecane plus 10% [v/v] silicone oil (AR 20) at a concentration of 8.7 mg ml^{-1} to form a lipid monolayer at the oil-water interface. This concentration is significantly below the solubility limit for our lipid mixtures. Meanwhile, 140 μl of 0.75% [w/v] ultra low melt agarose was spin-cast onto a plasma-cleaned coverslip at 4000 rpm for 30 s. The agarose-coated cover slip was sealed with a micro-fabricated poly(methyl methacrylate) (PMMA) device [159]. 180 μl of 2.8% [w/v] low melt agarose was used to seal the gap between the coverslip and device. The device was filled with the aforementioned lipid/oil solution. Incubated droplets were transferred to the device after 20 minutes to form a bilayer upon contact with the agarose substrate. Based on our previous work [160], we estimate a maximum bilayer hydrocarbon content of 9.2%.

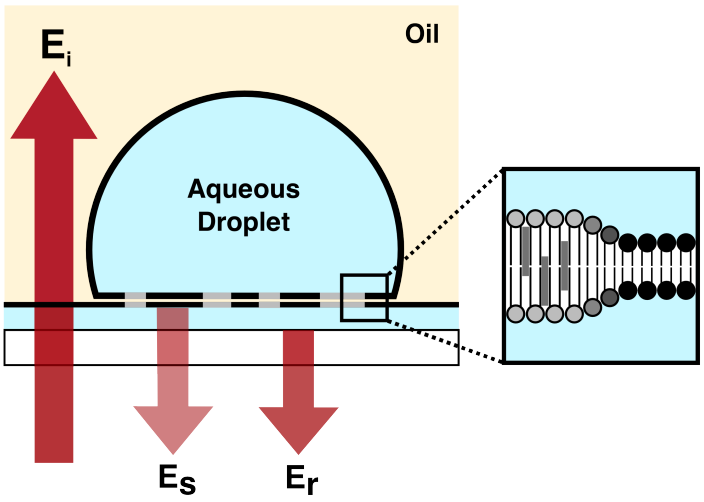


Figure 4.2: Schematic of a droplet interface bilayer (DIB) showing ordered (light grey) and disordered (black) phases. The incident, reflected and scattered light fields (E_i, E_r, E_s) are indicated in red.

Finally, the device was heated (46 °C) above the transition temperature of the high melting point lipid (in this case, brain sphingomyelin), cooled to room temperature and imaged using iSCAT and/or TIRF microscopy. While higher temperatures will promote faster mixing, they were also found to promote dehydration and on occasion to cause the droplet to burst.

When imaging droplets with iSCAT we observed closely spaced variations in intensity at the edges of the droplet (Figure 4.3), consistent with interference from light reflected off the top surface of the droplet and the light reflected from the coverslip. In droplets with small volume (10s nL), these fringes were also apparent in throughout the droplet. To minimise the amplitude of these patterns, we prepared droplets of large enough volume that the distance to the top of the droplet was greater than the coherence length of the laser, such that mobile domains could be tracked on a background of constant intensity. The largest

volume that could be held in the droplet preparation device was 800 nL. Domains close to the circumference of the droplet were discarded in analysis, as their contrast depends on the varying phase of the reflected field.

Experimental Setup: The experimental setup is described in Chapter 3. An illumination power density of 2 $kWcm^{-2}$ was used for imaging nanodomains at constant temperature (Figure 4.10), while a power density 10 times higher was used in order effect a temperature rise within the droplet and drive a phase separated mixture towards the single phase (Figure 4.6)

Tracking: S_o nanodomains were tracked by a home-written Gaussian fitting script in LabVIEW. The time-median value of each pixel was subtracted from the image prior to fitting, yielding a shot noise limited image. The trajectories were divided into 100 frame intervals, and the average contrast, average FWHM, and diffusion coefficient for each interval was calculated. To calculate the diffusion coefficient, a line with zero intercept was fit to the mean squared displacement (MSD) vs time lag, Δt, for time lags up to 20 frames (50 ms). The diffusion coefficient, D, is then given by slope/4. The data has been grouped by contrast and averaged for each 0.1% contrast interval.

Microdomains (FWHM $>$ 600 nm) were delineated by thresholding the image to the half-maximal intensity. The background subtraction could not be performed as previously described, due to the fact that microdomains did not move fast enough such that they could be subtracted from the background image by dividing the image stack by a temporal median image. The roughness of the agarose substrate was eliminated prior to thresholding by applying a high-pass filter (7 pixels). Domains in the thresholded, binary image were tracked by centroiding. The radius was found from the area of the domain, assuming a circular geometry.

L_o nanodomains were tracked by the imageJ Trackmate [161] plugin, which has been optimised to detect a high density of particles. The quoted lifetimes are

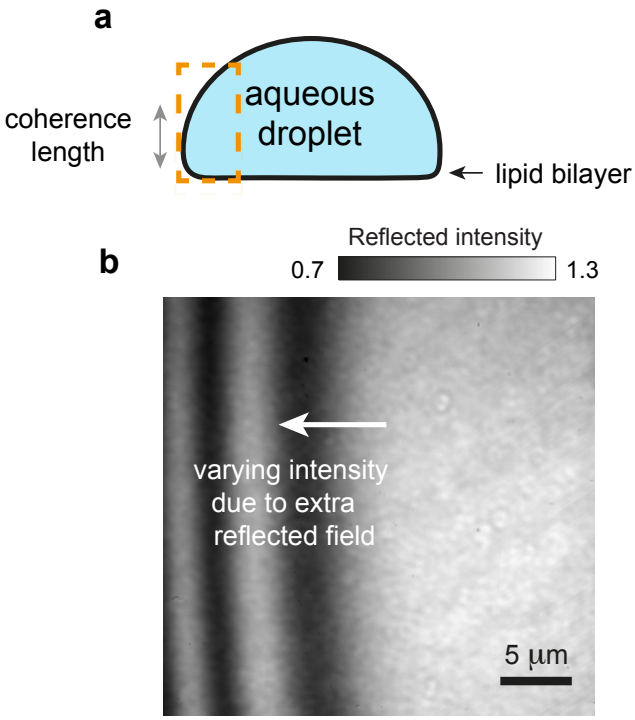


Figure 4.3: a) Schematic of a droplet, indicating the coherence length of the laser. b) A raw iSCAT image of the edge of a droplet, corresponding to the area within the dashed rectangle in a. The arrow indicates the region where the contrast of domains cannot be determined, due to varying background intensity from the interfering reflected fields.

proportional to the lengths of the tracks returned by Trackmate. For determining diffusion coefficients, FWHM and contrast, the data was divided into 50 frame intervals, or 100 ms. The data from all sub trajectories was binned into 0.2% contrast intervals, in order to display the binned HWHM and diffusion coefficients as a function of the contrast.

4.3 Results

4.3.1 Proof of concept 1: label-free detection

To validate the iSCAT method for detecting domains without labels, we prepared a lipid mixture in droplet bilayers as described in the methods above and allowed the droplet to cool to below the phase separation temperature to reach a state of macroscopic phase separation. A small amount of fluorescent dye was added, so that domains could be visualised in the fluorescence channel of our microscope. Figure 4.2 shows the resulting images in the fluorescence and iSCAT channels.

Domains are clearly visible in the iSCAT image, with a contrast of 2% (S_o domains) and a signal to noise ratio for a single 10 ms frame of 10-15, limited by unevenness of the agarose substrate. The droplet bilayer was formed from a binary mixture of DOPC and (brain) sphingomyelin (bSM) at a molar ratio of 1:1, with 1 mol% Atto488 labelled 1,2-dipalmitoyl-sn-glycero-3-phosphoethanolamine (Atto488-DPPE), which forms macroscopic solid ordered (S_o) and liquid disordered (L_d) phases.

4.3.2 Proof of concept 2: detection of nanodomains

A transition from the two phase region to the one phase region of the phase diagram can be brought about by a change in either the lipid composition or the temperature. As temperature is easier to control in real time than composition, we applied heat to effect a phase transition. We formed a DIB from a $1:1:1$ ternary lipid mixture of DPhPC, bSM and cholesterol, which partitions into L_o and Ld phases at room temperature (Wallace group, unpublished finding), but exists only in the liquid disordered phase above 38 °C. We heated this droplet to 45 °C for 10 minutes to allow thorough mixing of lipids, then immediately transferred the device to the

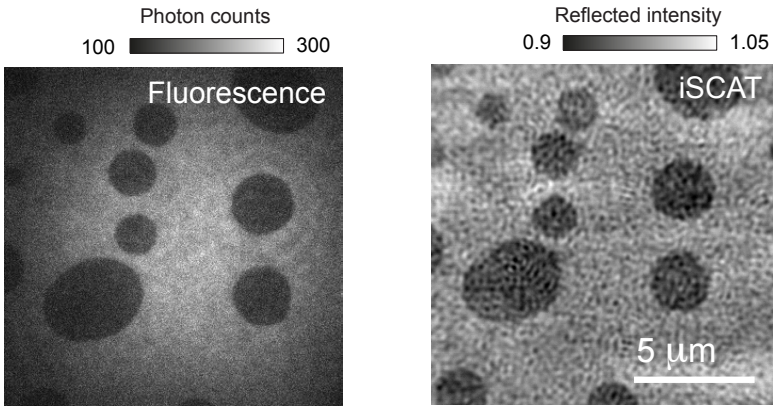


Figure 4.4: Detection of lipid domains using iSCAT and TIRF microscopy. 100 ms TIRF (left) and iSCAT (right) images of a DIB containing solid-ordered (S_o) domains within a bulk L_d phase. (1:1 DOPC:bSM plus 1 mol% Atto488-DPPE).

microscope and allowed the droplet to cool while imaging under iSCAT. We observed the appearance of nanoscopic domains (Figure 4.5) that grew in size as the sample cooled, and merged upon meeting. The fact that domains were observed to merge indicates that line tension is present, which can only be explained by these domains being a distinct phase. We can rule out non-ideal mixing, or structured compositions within a single phase as the source of these nanoscopic entities. Figure 4.5 shows a timelapse sequence of nanodomains appearing.

4.3.3 Control experiments

In all experiments we observe random contrast oscillations in the background, with RMS of 0.2% within a 300×300 nm area. To determine the source of these oscillations, we performed control experiments using a droplet bilayer composed of lipids that form a single phase, and using an agarose substrate in oil (no lipids or droplet). In both experiments we observed the same oscillations, indicating that the agarose is the source of the time varying background. While the oscillations

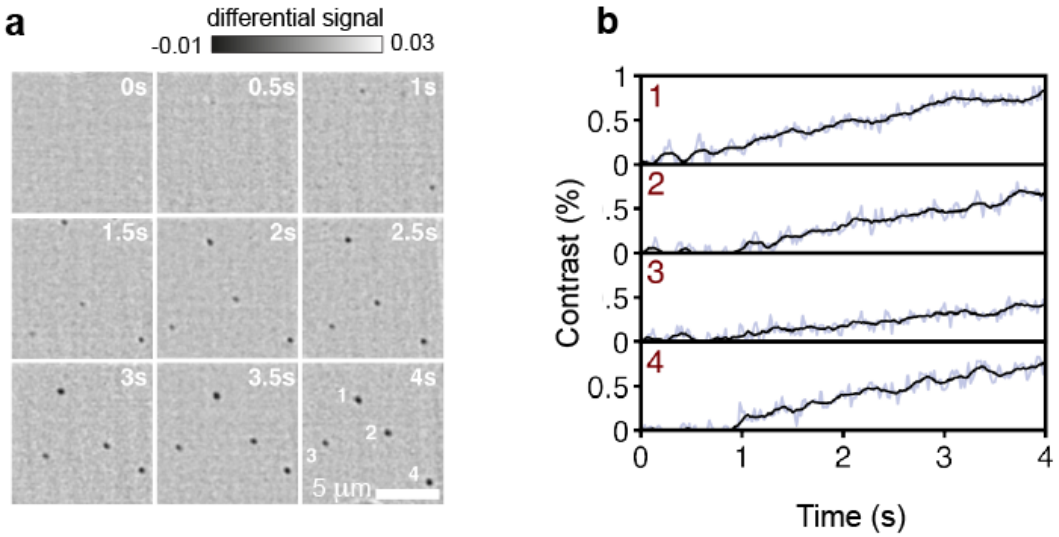


Figure 4.5: a) Time-lapse sequence of iSCAT images of L_o nanodomains appearing from a uniform L_d phase upon cooling of a droplet below the phase transition temperature. b) Time traces showing the average pixel contrast within a 900×900 nm window centred on each nanodomain shown in a. Values before the appearance of the domain are representative of the background fluctuations at the position where the domain first becomes visible. Images were recorded at 50 Hz using 445 nm illumination with power density of 0.2 kWcm^{-2}.

are small, they unfortunately limit the minimum sensitivity to several times greater than that determined by shot noise (RMS of 0.04% within a 300×300 nm area for a 40 nm effective pixel size used in these experiments.)

4.3.4 Determining the size of nanodomains

Using the above method, we observed domains that emerge from a bilayer of uniform contrast, or equivalently, composition. As the appearance of these domains was very rapid, however, we were not able to accurately determine the characteristics of their PSFs in order to estimate their size. To slow down the process, we applied a more gradual change in temperature. We also improved the heating method, using the illumination laser to locally heat the sample, thus avoiding small but for our purposes, significant, mechanically drift and distortions to the optics due to heat-induced expansion.

We noted that when heating large domains, they decreased in size until they disappeared and we only captured a single domain with the field of view. Whereas cooling the sample resulted in nucleation at a high density of sites. We can explain these results via line tension. In the former case we start with domains of high line tension, which are unlikely to divide as this would increase the total line length. On the the other hand, starting from a single phase, the line tension is initially zero, so at the point of domain nucleation there is no energetic preference for reducing line length. Heating, rather than cooling was both a faster experiment to perform, and allowed us to track single domains, without merging or fission, for long periods of time. This allowed us to very precisely measure domain FWHM and contrast for a monotonically decreasing domain. The measured values for several domains are shown in Figure 4.6.

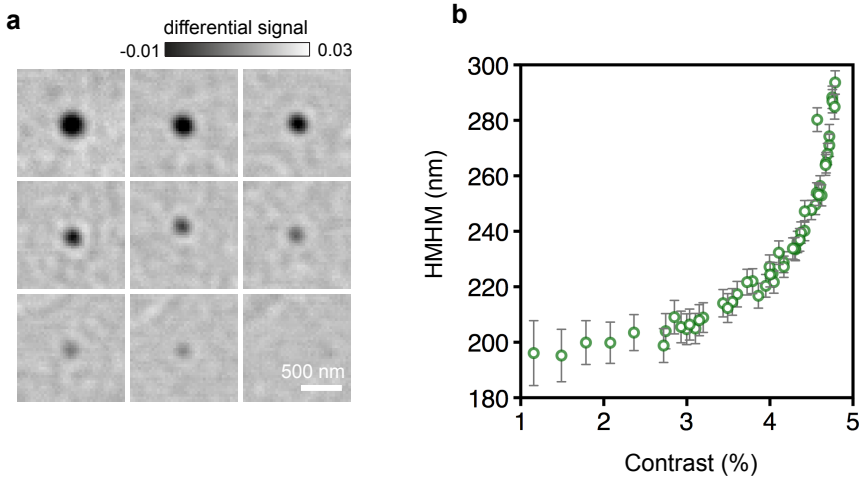


Figure 4.6: (a) 15 s, timelapse sequence of iSCAT images showing shrinking S_o nanodomains in a DIB (1:1 DOPC:bSM. (b) HWHM vs contrast for the same dataset as shown in (a). Error bars show the average error in the HWHM, based on the covariance of the Gaussian fitting parameters. The data have been appended from separate movies, rather than to attempt to follow the domain across a typical travel of several tens of micrometers. Images were recorded at 2 kHz using 662 nm illumination with power density of 13 kWcm^{-2}. Frames were binned to 100 Hz before fitting.

We found it easier to work with domains in the solid ordered phase, as the high line tension creates an energetic barrier to merging events, due to the large energy cost required to deform the edges of the domain. Liquid ordered domains, on the other hand, have a much lower line tension and consequently a lower kinetic barrier. As such we prepared DIBs with S_o domains (DOPC:bSM 1:1, plus 1 mol% Atto488-DPPE). Upon application of high laser power, the measured FWHM decreased and plateaued at the diffraction limit. Below this size, the contrast of domains continued to decrease, but there was no measurable change in FWHM. As the contrast scales roughly with the mass of scattering material within the diffraction limited spot, this indicates a continued change in domains size. The fact that the change in FWHM is not detectable across the range from 2% contrast to the detection limit indicates that these domains are significantly smaller than the diffraction limit in size. We can also identify the contrast and corresponding FWHM at which domains first become smaller than the diffraction limit by the point where the contrast begins to decrease. This decrease in contrast indicates that the domain occupies an areas smaller than the diffraction limited volume.

We have previously measured noise levels of only 0.024% (after subtraction of all static background features) by imaging at 2kHz and averaging to 10 Hz [118]. Therefore it should be possible to detect very small domains, with contrasts down to 0.1% while maintaining a signal to noise ratio greater than 4. However, in the current experiments, we observe random contrast fluctuations from the agarose hydrogel, which are likely due to density variations and mobility of the hydrogel. These fluctuations set a small, but non-subtractable background level of 0.1 - 0.2% RMS. We therefore set a threshold detection limit of 0.5% contrast.

Size Determination from the FWHM

From the shape of Figure 4.6 we assume that the minimum FWHM measured (387.6 nm, for illumination at 662 nm) is the PSF of our microscope. By deconvoluting the measured FWHM with a Gaussian PSF, we can determine the radius of domains.

While this method can be applied to the entire data set, the error becomes very large for small radii, where nm fluctuations in the measured FWHM yield large variations in the calculated radius. The reason for this is that the function of FWHM plotted against radius approaches a vertical asymptote as the radius tends towards zero. We disregard this unreliable data by setting a cutoff in the relative error (i.e. error/radius) of 10%, which applies for radii down to 70 nm.

Size Determination from the Diffusion Coefficient

The mobility of an object diffusing within the membrane can be described by the continuum, hydrodynamic equations for diffusion of a cylindrical object in a two dimensional sheet, analogous to the Einstein-Stokes equation for diffusion in an isotropic (three dimensional) medium. The two dimensional system is more complicated to solve, as two different viscosities are involved, namely the viscosity of the membrane and of the aqueous environment above and below the plane of motion. Whether the diffusion is dominated by drag forces within the membrane, or by the drag between the diffusing object and the solvent, depends on the ratio of the viscosities and the size of the object and can be expressed by the quantity $\epsilon = \frac{r}{\lambda}$ where r is the radius of the object and $\lambda = \frac{\eta}{2\mu}$ with η, μ the viscosity of the solvent and membrane respectively. In the limits where ϵ is very large ($\epsilon >> 1$) or very small ($\epsilon << 1$), Saffman and Delbrück demonstrated that the hydrodynamic equations reduce to simple analytic forms in their seminal paper published in 1975

[162]. In the large ϵ limit, the diffusion coefficient is proportional to the inverse of the radius. This expression is frequently used to fit diffusion coefficients measured for domains of several tens of microns in size. In the small ϵ limit, the diffusion is less sensitive to object size, scaling with the inverse logarithm of the object radius. This expression applies to objects the size of proteins, however there is some debate about whether it accurately describes diffusion on the molecular scale [163]. In between the small and large limits - that is precisely in the region that spans the size of lipid rafts - no simple analytic expression exists. While the Saffman Delbrück equations are by far the most widely used models for describing diffusion in the membrane, the error between the limiting forms and the full hydrodynamic solution diverges to infinity in the region of 10s to 100s of nm [164], so it is wise to avoid applying either limiting form to the diffusion of nanodomains.

A few years after the work of Saffman and Delbrück, Hughes, Pailthorpe and White derived the complete solution, valid across an unrestricted range of radii [165]. This solution has no analytic expression, and requires considerable computational power to evaluate. An approximate analytic expression that closely reproduces the complete solution was recently calculated by Petrov and Schwille [166]. In the assumption that nanoscopic domains can be accurately modelled as solid, cylindrical inclusions, and the discrete molecular nature of the membrane can be ignored, then the Hughes, Pailthorpe and White / Petrov Schwille form should describe the observed diffusion as a function of radius.

There is concern, however, about the validity of this continuum hydrodynamic model, especially when approaching molecular length scales. In particular, the fact that the membrane surrounding is not infinitely divisible, but composed of molecules with finite dimensions, and that domains themselves are neither rigid nor incompressible, cast doubt about the applicability of this model for describing the diffusion of nanodomains and smaller. It has also been pointed out that the

height difference between the ordered and disordered phase, may have a significant affect on the 3D hydrodynamics in the aqueous environment [163]. In an attempt to create a more realistic model of nanodomain motion, Guigas and Weiss used a "dissipative particle dynamics" model to replicate how the random impact forces are dissipated by the molecular modes of motion of lipids within domains [167]. According to dissipative particle dynamics, which has been thoroughly described in [168, 169], the authors model each domain by a small number of particles, each of which is composed of 4 beads, the first bead representing the hydrophilic head and the remaining beads representing the hydrophobic tail regions of a lipid. Bending, stretching and repulsion potentials are calibrated to reproduce realistic diffusion coefficients. This method is less computationally intensive than full molecular dynamics simulations, allowing simulations to be performed on time and length scales inaccessible to atomistic simulations while aiming to reproduce the vibrational and rotational modes of the molecular system. Calculating the dissipation of forces as a function of mode frequency, yields the semi-empirical equation 4.2. We find that the Guigas-Weiss model fits our dataset well (green trace in Figure 4.7) ($\chi^2 = 2.957$, $\eta_c = 0.00505 Nsm^{-2}$, $c = 1.377\mu$m where η_c is the solvent viscosity and c is an empirical constant of the model).

$$D = k_B T \frac{tan^{-1}\frac{c}{r}}{8\pi\eta_c r} \tag{4.2}$$

Evans and Sackmann show that a similar deviation from the hydrodynamic model also results if domains experience a frictional drag force from the substrate [170]. We note that no friction is detected is detected in our experiments with droplet bilayers, and so we do not consider this to be a viable physical model. Tracking of both nanoscopic and macroscopic domains is Brownian at all length scales, as shown in Figure 4.7 a. These results are in agreement with previous work in the literature where the presence of the hydrated agarose substrate did not affect protein diffusion

in DIBs [160].

To test the models described above, we measured the diffusion coefficient of solid ordered domains in the range of 70 nm radius (determined by deconvolution of the FWHM) up to 1.5 μm, and evaluated the quality of fit of the diffusion model. As domains were slowly changing in size, we presented the diffusion and size at 50 ms intervals. We decided to measure solid ordered domains due firstly to the previously mentioned ease of tracking, and secondly because the assumptions of the continuum diffusion equations (rigid, cylindrical domains) better describe solid ordered domains than liquid ordered domains, which are composed of individually mobile lipids and have oscillating edges due to lower line tension.

We found that the continuum diffusion model fits the data for large microdomains, but underestimates the diffusion of domains with radius below 500 nm. The Dissipative model of Guigas and Weiss, on the other hand, fits the data within the error bars of each data point. While the Evans and Sackmann model also fits our data (χ^2 =3.002) we can rule this model out as our data indicates no frictional drag.

Using the Guigas-Weiss scaling of the diffusion coefficient with domain radius, we are able to estimate the size of domains much smaller than the diffraction limit from the measured diffusion coefficient alone. Given that the contrast is related to the amount of scattering material, and therefore to the radius, we sorted the diffusion values by their corresponding contrast, and calculated the average diffusion and radius in intervals of 0.1% contrast to obtain Figure 4.8. The fastest measured domains, with diffusion coefficient of 1 $\mu m^2 s^{-1}$ correspond to a radius of 50 nm.

The Diffusion-radius scaling further allows us to calibrate the contrast as a function of radius, shown in Figure 4.8. We note that the contrast increases with radius up to 160 nm. This value, determined from the diffusion coefficient and Guigas-Weiss scaling, is consistent with the expected plateau in contrast for domains above the size of the diffraction limit.

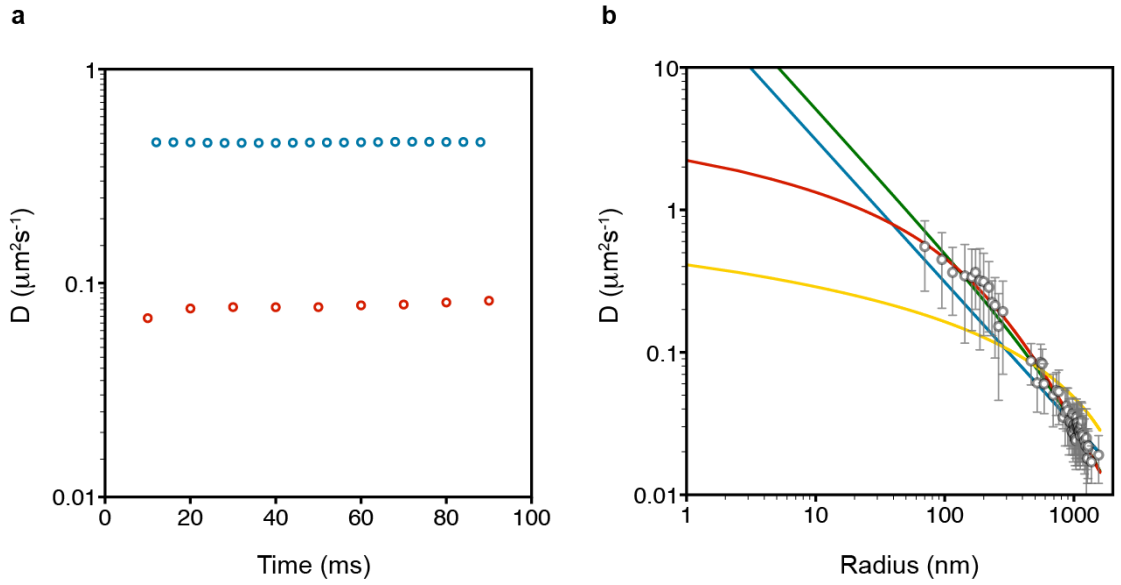


Figure 4.7: a) Tracking of nanodomain (blue) and microdomain (red) diffusion shows invariance with respect to time lag. b) Comparative fits of various diffusion models for S_o domains ranging in size from $\sim$ 100 nm to 2 μm: Hughes-Pailthorpe-White/Petrov-Schwille (blue), Guigas-Weiss (green), Evans-Sackmann (red) and large limit Saffman-Delbrück (yellow). All data shown was recorded at 500 Hz using 662 nm illumination at a power density of 2 kWcm^{-2}.

4.3.5 Dynamic observation of liquid ordered nanodomains

Although S_o / L_d phase coexistence does play a limited role in vivo [171, 172], it is nanoscopic L_o / L_d phase coexistence that is the hallmark of lipid rafts. Ternary lipid mixtures of sphingomyelin, phosphatidylcholine, and cholesterol result in coexisting liquid phases, but nanoscopic domains are expected only for compositions where the line tension is low [146].

Quaternary lipid mixtures, pioneered by Feigenson and co-workers, provided us with a model system with highly controllable line tension, which has been shown to result in domains of different domain size [73]. We exploited quaternary mixtures of DOPC, POPC, bSM and cholesterol to create L_o nanodomains with compositions ρ:(1-ρ):1:1, where ρ is the relative fraction of DOPC and POPC in

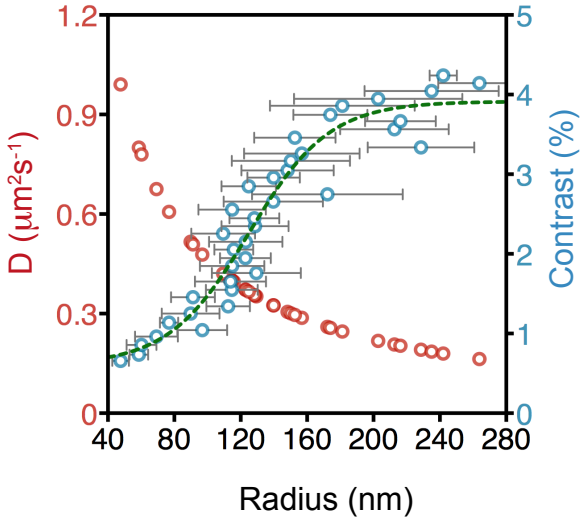


Figure 4.8: Diffusion coefficient (red) and contrast (blue) of S_o nanodomains as a function of theoretical radius, via the diffusion vs radius calibration. The radius has been determined from a fit to the microdomains S_o diffusion data, using the Guigas-Weiss model. Contrast increases with increasing radius and can be approximated by a sigmoid (dotted line). Error bars show the values of the radius corresponding to $\pm$ 1 standard deviation in the measured diffusion coefficient. All data was recorded with 532 nm illumination with a power density of 20 kWcm^{-2}. Images were collected at 4 kHz, and binned to 400 Hz before fitting.

the mixture. By increasing the ratio of the biologically abundant phospholipid POPC, with respect to the highly perturbing non-abundant lipid DOPC, we observed a shift from microscopic to nanoscopic domain size similar to that reported previously [73], as well as a gradual increase in the amplitude of edge fluctuations. Example images of domains at the different compositions are shown in Figure 4.9.

Only microdomains can be distinguished by TIRF, whereas both nanodomains and microdomains are visible in iSCAT as ρ is varied (Figure 4.9). For $\rho \leq 0.7$, both nanodomains and microdomains with fluctuating boundaries were present and we could reveal fusion events between nano and microdomains (Figure 4.10, example a).

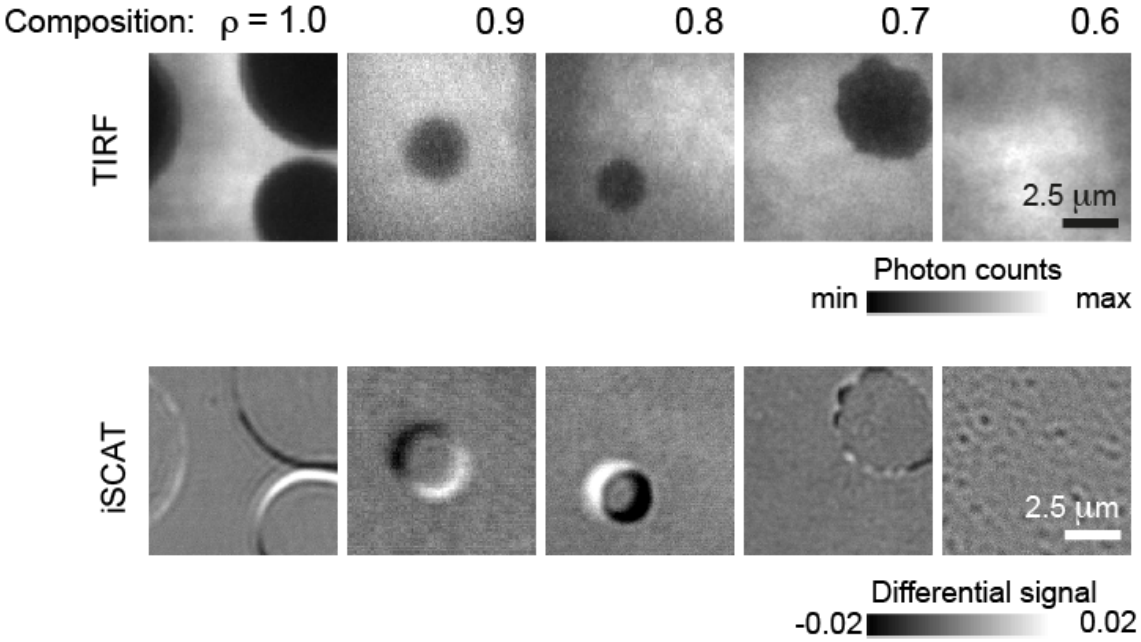


Figure 4.9: TIRF and iSCAT images for quaternary mixtures of DOPC, POPC, bSM, and cholesterol in ratios ρ:(1-ρ):1:1 mol%, with the fraction, ρ, varying from 1 to 0.6. DiI was also added (1 mol%) for fluorescence imaging. iSCAT images were collected at 500 Hz using 662 nm illumination and binned to 100 Hz. TIRF images were collected at 100 Hz and binned to 10 Hz.

For $\rho = 0.6$ we observed nanodomains appearing, merging and disappearing (Figure 4.10, example b, c, d). Coalescence between domains was common, and by tracking individual domains we were able to determine a nanodomain lifetime of 220 $\pm$ 6 ms (Figure 4.11b). As the lifetime is related to the domain size, the lower limit of the distribution of lifetimes is determined not by the nanodomains themselves, but by the noise of our measurement

In contrast to S_o domains, all L_o nanodomains detected had the same HWHM within measurement error (Figure 4.11), consistent with the nanodomains being significantly smaller than the diffraction limit. In order to determine the size of these domains it is necessary to use a property that varies with domain radius, the two options being the diffusion coefficient and the contrast. Either method requires a calibration that relates the measured property to the radius of a domain.

The frequent merging of domains at this composition made it difficult to determine diffusion coefficients of L_o microdomains, and hence we could not calibrate the domain size in the same manner as described previously for S_o domains. We considered using the S_o calibration, however this is likely to be imprecise for the L_o phase, where the individual lipids within a domain are in motion as a fluid.

On the other hand, all that is needed to calibrate the contrast is the maximum measured value of contrast, which can be determined from any domain larger than the diffraction limit. This value can be equated to the contrast of a domain which is the same volume as the PSF. The calibration can then be derived by scaling the function relating contrast and radius for S_o nanodomains (shown in Figure 4.8), by the the ratio of maximum contrasts for each phase. Calculated in this way, the distribution of L_o domain radii ranges from 50 - 200 nm, shown in Figure 4.11, where the lower limit is set by the detection limit of the technique. We note that these calculations rely on the assumption that there is only one nanodomain per diffraction limited area.

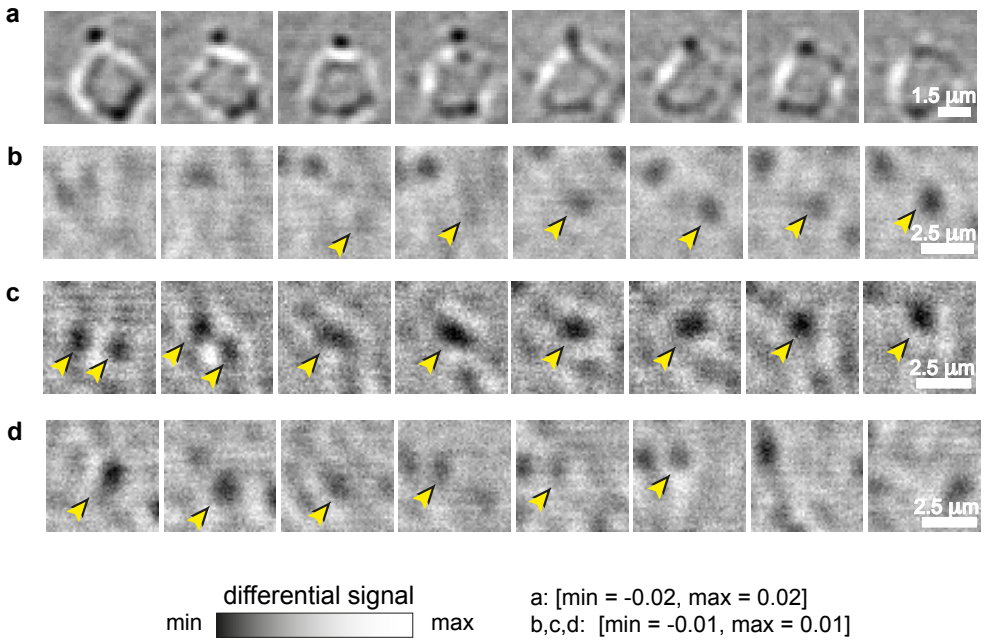


Figure 4.10: Image sequences showing L_o nanodomains appearing, merging and dissolving. Images were recorded at 500 Hz using 662 nm illumination at a power density of 2 kWcm^{-2}. Image sequences shown have been frame binned to 50 fps. $\rho = 0.6$.

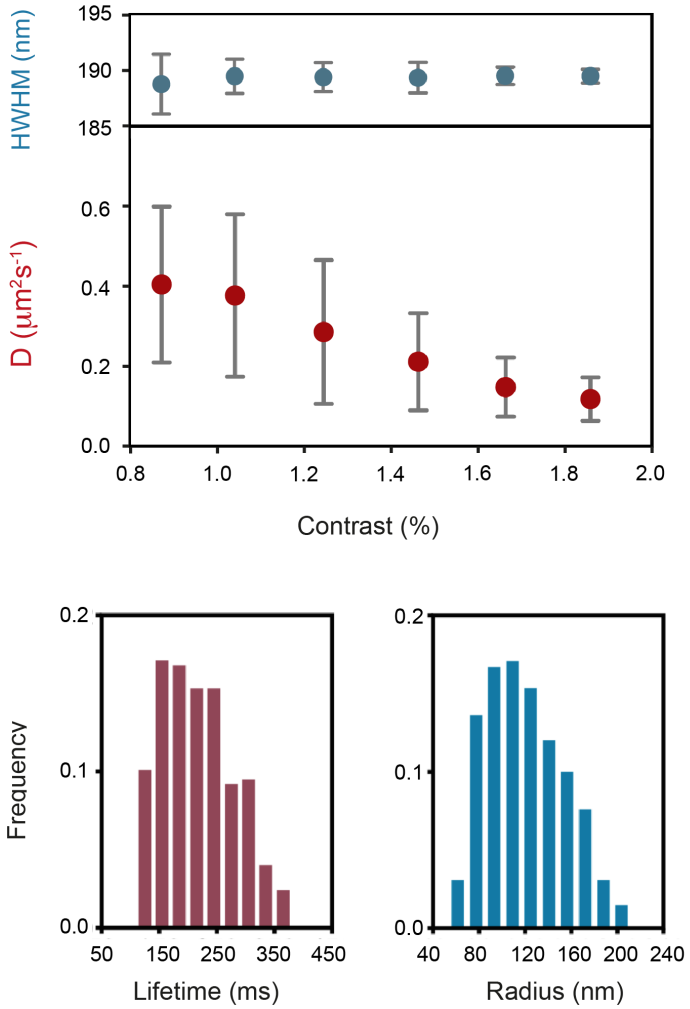


Figure 4.11: Top: Measured diffusion vs. contrast and HWHM vs. contrast for ρ = 0.6. Left: Distribution of lifetimes of nanodomains for $\rho = 0.6$ (749 domains). Right: Distribution of measured radii for ρ = 0.6. Error bars are the standard deviation of the data within each contrast bin. Images were recorded at 500 Hz using 662 nm illumination at a power density of 2 kWcm^{-2} and frame binned to 100 Hz before fitting.

4.4 Discussion

Our results represent the first direct observation of fluctuating nanoscale domains, and indicate several interesting possibilities regarding the potential role of lipids in orchestrating membrane organisation on short time and length scales.

Entropic trapping of nanoscopic domains

If line tension is sufficiently low, mathematical models indicate that dispersions of nanoscopic sizes can be entropically favourable [146]. Depending on the balance of the decrease in the entropy that results from domain merger compared to the decrease in boundary energy, the trapped state can be stable (fluctuating nanodomains exist for infinite times), metastable (fluctuating nanodomains exist for finite times of hours to days, gradually ripening into one macroscopic domain), or unstable (over seconds, nanodomains merge to form one macroscopic domain). Theoretical modelling determined that the boundaries between these regimes occur at domain radii of 40 nm, 40 - 100 nm, and greater than 100 nm, for a moderate line tension of $\gamma = 0.2$ pN, within the range of typical values measured for L_o domains in a L_d bulk phase. The domain lifetimes for this syetm vary from 0.05 s to several hours, depending on the diffusion coefficient, and the height of any repulsive barrier when two domains approach one another (for example, due to accommodating the height differences of the surrounding phase) [146]. Our observations of domain radii below 200 nm closely matches the modelled upper limit of 100 nm. The small discrepancy in the maximum stable domain size might be explained by a difference in line tension, or by a number of simplifications that have been made in the model, including the assumption that the composition of a domain does not evolve as the domain grows and is homogeneous from the centre to the edges. The measured lifetime of 200 ms falls towards the lower end of the bounds of the model, consistent with a low repulsive barrier and fast diffusion.

A mechanism for coordinating signalling events?

The small and transient nanodomains we have observed in this model membrane resemble the raft structures that biologists have been searching for in cells [173]. As such, we consider the possibility that living cells contain a similar dispersion of small, entropically-trapped, liquid ordered domains. We then ask whether such nanodomains could be biologically relevant - in particular, is their lifetime long enough to fulfil the assumed roles that lipid rafts play in signalling processes?

Many of the protein-protein interactions underlying signal transduction are on the scale of seconds [174]. For example, in T cell activation the turnover rate of the kinase activity of Lck is estimated to be 0.02-2 molecules per second [175], and the half-life of the interaction between Zap70 and phosphorylated T cell receptor-chain is about 8 seconds [32]. A direct comparison with the $\sim$200s ms lifetimes we have observed for nanodomains of 50-200 nm radius indicates a discrepancy.

Before coming to an immediate conclusion, however, it is necessary to consider the differences between our system and the plasma membrane of living cells, and how these factors affect domain lifetimes. To highlight one important difference, the size of rafts in cells has been established to be less than 20 nm diameter [173], which is five times smaller than the smallest size we have observed. Such small domains would necessarily have a very low line tension if they were to be entropically trapped [146]. The proteins in the cell membrane are also though to decrease the line tension of nanoscopic domains. We then ask, how line tension affects domain dynamics. Using the model proposed by Frolov, it follows that line tension results in a greater likelihood, of domain fission i.e. a shorter domain lifetime. The impact of merging is less straightforward to calculate [1], but if the nanodomains remain disperse with a

[1]The lifetime of domain merging depends on a combination of competing factors - namely the domain size, the area fraction of the liquid ordered phase, the diffusion coefficient and the line tension. We note that for very small domains any kinetic barriers to merging, such as the membrane deformation required, are insignificant [146].

constant size distribution, we may assume that the rates of merging and fission are equal.

In summary, we expect sub 20 nm domains to exist for much less than 200 ms before merging or dividing. Smaller regions of lipids and proteins within a domain, however, may exist together for longer than this timescale. It has also been established that raft-associating GPI-anchored proteins interact through their ectodomains, which may stabilise raft domains in cells[32]. It is therefore difficult to say whether phase separation of the lipid bilayer yielding entropically trapped nanodomains does indeed explain the organisation within the plasma membrane, or whether protein interactions are the driving force.

Matter transfer and signal amplification

If the plasma membrane is a dispersion of entropically trapped nanodomains, a number of interesting implications emerge from the dynamics of this system. When domain size is small, fission and fusion of domains are the primary modes of matter transfer, rather than domain ripening [146], which is much slower. This suggests that nanoscopic phase separation may allow highly efficient molecular trafficking [146].

In addition, it has been suggested that the cell composition may be located close to a phase separation boundary as a means for the cell to instigate dramatic changes in structure, with only an infinitesimal change in composition or temperature. This is clearly useful for amplification of small signals. Our findings suggests another mechanism by which large changes in domain size and properties could occur. As the stability of the entropically trapped state is very sensitive to line tension, a small change in this parameter could be a means to trigger the growth of metastable nanodomains into large phase separated regions. Simulations have shown that the interface between the ordered and disordered phases is enriched in cholesterol, which

has been proposed to reduce line tension [176], and whose concentration is known to be highly regulated in the cell membrane [177].

How do nanodomains form *in vivo*?

While we have observed that lipids alone are capable of forming nanodomains in model membrane, various other mechanisms have been suggested by which rafts may form in vivo. These include: nucleation of L_o domains around proteins [178]; stabilising L_o / L_d domain coexistence by membrane curvature [179, 180]; and critical fluctuations, where line tension is close to zero and fluctuations of L_o and L_d phases occur with minimal energy cost [181, 182]. Several more mechanisms of membrane heterogeneity that do not involve phase separation have been posited, including solubilisation of islands of distinct composition by surfactant-like proteins and/or lipids that reduce line energy close to zero. It is possible that phase behaviour in cell membranes involves multiple of these proposed mechanisms.

Current limits to the method

As outlined in section 4.3.3 the lower limit of sensitivity is determined neither by the iSCAT method nor the equipment, but by background noise caused by motion of the sample. As such, development of a protocol for studying bilayers on solid supports such as mica, could allow the detection and tracking of domains much smaller in size, allowing visualisation of the early stages of nanodomain formation as well as improving the accuracy of the relationship between domain size and mobility.

We note that a new fluorescence imaging technique - inverse FCS - has recently been developed [183] that could allow the visualisation of nanodomains in the size range of 10s of nm. While this technique has not yet been applied to the visualisation of domains, it could achieve sensitivities far in excess of standard FCS

as detection relies on labelling of the disordered phase, overcoming limitations with low partitioning of dyes into the liquid ordered phase and short residence times. It would be valuable to compare the domain sizes and diffusion coefficients from both inverse FCS and label-free iSCAT.

The ultimate limitation with iSCAT (or any diffraction limited method) would be the difficulty in determining whether more than one domain is present within a diffraction limited volume. The contrast for iSCAT detection simply relies on a difference in light scattering between phases, and although this is a primary advantage of this label-free method, it also presents a significant future challenge for applying this technique to real cell membranes.

4.5 Summary and outlook

By exploiting the differences in light scattering from different lipid phases we have used iSCAT microscopy to achieve dynamic imaging of lipid nanodomains, for the first time. We observe nanodomain formation, dissolution and dynamic coalescence - behaviours that have been hypothesised, but never observed, and are critical to the proposed functions of lipid rafts.

The ability to image membranes and model lipid bilayers without labels opens up many interesting possibilities, such as studying the dynamics of membrane assembly and repair, and the fusion of vesicles with membranes. In addition, the facile combination of iSCAT with TIRF imaging provides future opportunities for investigating how specific lipids and proteins associate with ordered domains, and for studying the effects of lipid organisation on the mobility and interactions of signalling molecules - crucial to understanding the earliest stages of signalling pathways in cells.

4.6 Contributions

This work is partly based on the following publication: de Wit, G, Danial, JSH, Kukura, P and Wallace, MI. Dynamic label-free imaging of lipid nanodomains. Proc Natl Acad Sci USA, 112: 12299-12303, 2015.

Experimental work was carried out using the setup described in Chapter 3. Droplet Interface Bilayers were prepared by John Danial. Data analysis of nanodomain diffusion and properties was performed by myself. All authors contributed to the interpretation of results.

Chapter 5

Single Particle Tracking in Model Membranes

5.1 Introduction

Single particle tracking based on detection of light scattered by nanometer size gold labels offers a combination of spatial precision and temporal resolution that is unique among optical techniques, providing the possibility to precisely study how molecules move and interact with their environment. When observed with high temporal resolution many molecules within the membrane display heterogeneous mobility that cannot be described by Brownian motion. A number of potential mechanisms have been suggested as the underlying cause of this anomalous diffusion, including transient binding to immobile molecules, formation of short-lived complexes, association with raft domains, spatial variation in membrane viscosity, and corrals created by the the membrane-adjacent cytoskeleton. Only by observing single molecules with a temporal resolution much shorter than the lifetime of transient events and with a spatial accuracy close to molecular dimensions is it possible to distinguish between these mechanisms.

In this chapter we investigate the mechanism and detailed spatio-temporal dynamics of anomalous diffusion in a simple, all-lipid model membrane. Specifically, we investigate the mobility of ganglioside GM1, a lipid of considerable interest in biological membranes due to its association with lipid raft domains [63], and its involvement in a number of important membrane processes, including endocytosis [184, 185], B cell signalling [186], and membrane domain formation [187, 188]. Moreover, GM1 has been shown to undergo anomalous diffusion in cells [189, 64, 65], which is thought to be important to its biological function. Elucidating the mechanism(s) of anomalous diffusion of GM1 is therefore important for understanding its specific functions, and may also elucidate general mechanisms utilised by the cell membrane.

While a number of potential biological mechanisms for anomalous diffusion have been proposed, it is important to note that SPT experiments are also susceptible to artefacts associated with large labels [190], substrate interactions [92], poor localisation precision [191], and the time resolution of the measurement [192]. Accurate interpretation of high speed SPT data therefore requires careful characterisation and comparison to control experiments. To investigate the existence of such artefacts we perform control experiments varying substrate and label size, and we characterise the localisation precision of our experiments. With the unprecedented combination of speed and precision that is possible with iSCAT microscopy, we aim to identify the underlying mechanism of anomalous diffusion in a simple bilayer membrane for the first time.

5.2 Methods

Summary: We use iSCAT to track GM1 molecules in supported lipid bilayers composed of 1,2-dioleoyl-sn-glycero-3-phosphocholine (DOPC) with trace amounts of GM1 (0.03 - 1 mol%). A spatial accuracy of 0.7 nm and 2.2 nm was achieved using ϕ = 40 nm and 20 nm gold nanoparticles respectively, with a simultaneous 20 μs temporal resolution. As a benchmark system, a bilayer composed of 1,2-dioleoyl-sn-glycero-3-phosphocholine (DOPC) with a GM1 composition of 0.03% was formed on a glass substrate and GM1 molecules were labelled with 40 nm AuNP. In subsequent experiments, the following parameters were independently varied:

- Substrate - glass vs mica;
- Label size - 40 nm vs 20 nm gold nanoparticle;
- GM1 tail - native (nt-GM1) vs di-oleoyl (DO-GM1);
- GM1 headgroup - native (nt-GM1) vs dipalmitoylphosphoethanolamine (DPPE) and;
- GM1 concentration - 0.03 to 1 mol%.

Labelling: Specific labelling of GM1 was accomplished by incubating streptavidin-coated gold nanoparticles with biotinylated Cholera Toxin B subunit (CTxB), which acts as a ligand to the GM1 oligosaccharide headgroup, binding up to 5 GM1 molecules. For control experiments, biotinylated DPPE was coupled with streptavidin gold.

Materials: The compounds 1,2-dioleoyl-sn-glycero-3-phosphocholine (DOPC), 1,2-dihexade- canoyl-sn-glycero-3-phosphoethanolamine-N-(cap biotinyl) (DPPE), and GM1 bovine brain ganglioside (GM1) were purchased from Avanti Polar Lipids (Alabaster, AL). DO-GM1 was prepared as described before [193]. Biotin-labelled

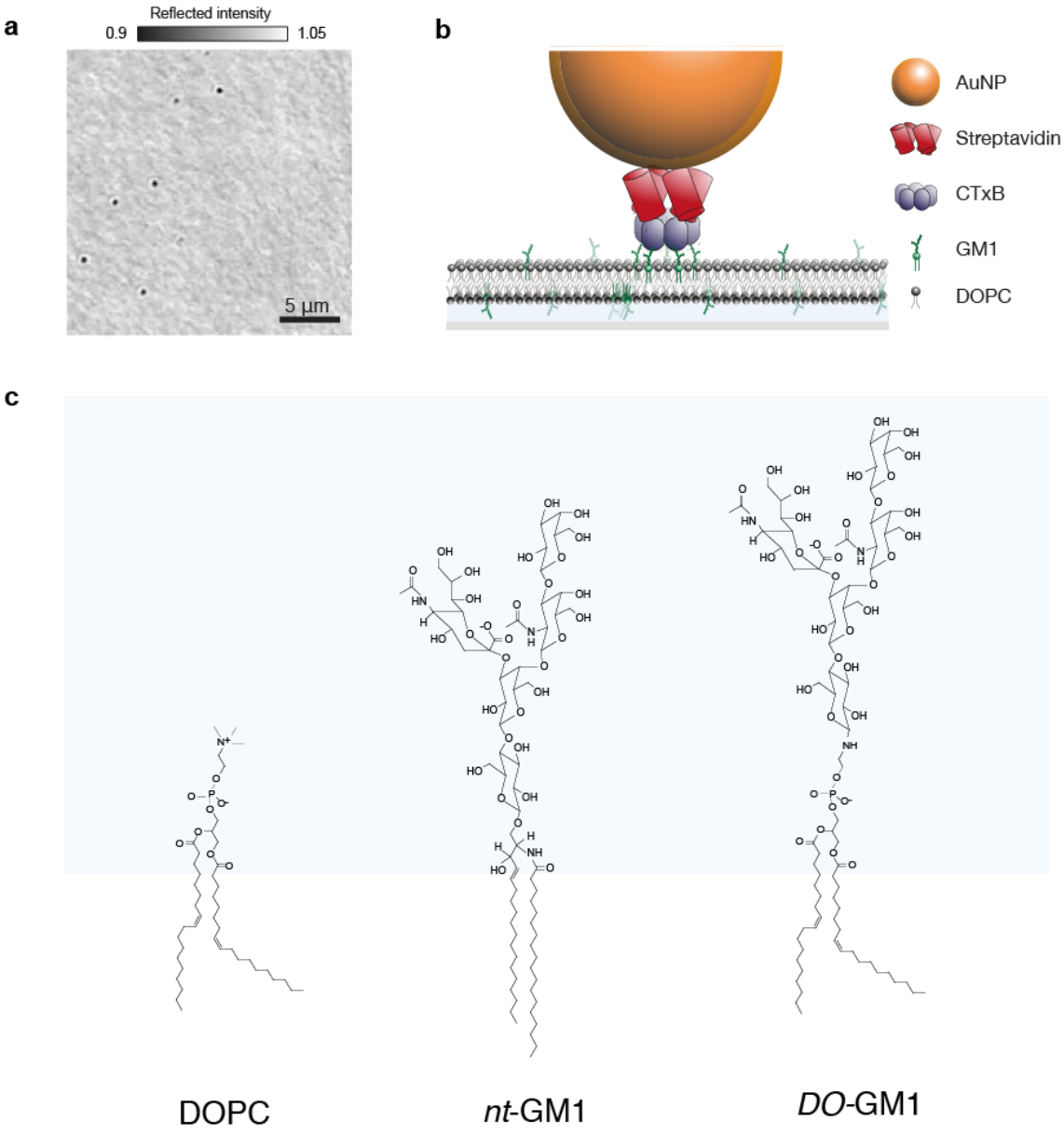


Figure 5.1: (a) Representative interferometric scattering image of $\phi = 20$ nm AuNP/CTxB/GM1 receptor complex diffusing on a supported lipid bilayer. (b) Schematic of the GM1 assay. (c) Chemical structures of DOPC, native GM1 (nt-GM1) and di-oleoyl GM1 (DO-GM1).

cholera toxin B (CTxB) subunits from Vibrio cholera were purchased from Sigma-Aldrich and reconstituted with water to give a solution containing 0.05 M Tris buffer, pH 7.5, 0.2 M NaCl, 3 mM NaN_3, and 1 mM sodium EDTA.

Conjugation of gold nanoparticles: Gold nanoparticles (AuNPs) functionalised with streptavidin were purchased from British Biocell International, diluted to a concentration of 9×10^{10} particles/ml and incubated with a 10-fold excess (enough to cover the surface area of the AuNP 10 $\times$) of biotin-CTxB at room temperature for 1 h. Excess CTxB was removed by centrifuging the AuNP/CTxB sample for 2 min at 14000g and resuspending the pellet in bilayer buffer (10 mM HEPES, pH 6.8, 200 mM NaCl and 2 mM $CaCl_2$). On the basis of a streptavidin contact area of 25 nm^2, and assuming that streptavidin covers 50% of the surface area of a AuNP, we estimate that there are 25 CTxB per $\phi = 20$ nm AuNP and 100 CTxB per $\phi = 40$ nm AuNP. For DPPE tracking experiments, streptavidin-functionalised AuNPs were added directly to the bilayer. We rule out nonspecific binding of the gold nanoparticle to the membrane, as particles not functionalised with CTxB did not interact with GM1-containing SLBs but were easily washed away.

Substrate preparation: No. 1.5 borosilicate cover glass (Menzel-Gläser) was etched in 2:1 H_2O_2:HCl for 10 min, followed by thorough rinsing with ultrapure water (Merck Millipore). The clean substrates were dried with a gentle stream of nitrogen and etched with oxygen plasma for 8 min at 50 W power immediately prior to vesicle deposition (Diener Electronic, Plasma System Femto). Mica substrates were prepared by bonding a 22 mm square sheet of mica (Agar Scientific) to a clean cover glass using optical adhesive (Norland Optical Adhesive 61). Immediately prior to vesicle deposition, the mica was cleaved leaving a thin, optically transparent layer adhered to the cover glass.

Vesicle preparation: Small unilamellar vesicles (SUVs) were prepared by the vesicle extrusion method. Lipids in organic solvent were mixed in a glass vial and

the solvent evaporated first under a gentle stream of nitrogen for 5 min and then under vacuum for 30 min. The dried lipid film was resuspended to a lipid concentration of 1 mg/mL in bilayer buffer. Lipid suspensions were vortexed for 1 min, hydrated at room temperature for 30 min and then passed 21 times through a 100 nm polycarbonate membrane using a mini extruder (Avanti Polar Lipids), resulting in clear suspensions of SUVs. SUVs were stored at 4 °C and used within 24 h.

Supported lipid bilayers: We use supported lipid bilayers (SLBs) as a well understood and reproducible model membrane [194]. SLBs were prepared in sample chambers, assembled by placing a CultureWell silicon gasket (Grace Bio-Laboratories) onto the glass or mica substrate. SLBs were formed by adding 20 μL bilayer buffer followed by 10 μL of the 1 mg/mL SUV suspension to the 30 μL sample well and incubating for 5 min. Landing of vesicles and eventual formation of the bilayer was visualised in real time using the wide-field (30 μm $\times$ 30 μm) iSCAT channel. Excess SUVs were rinsed away by extracting most of the supernatant solution and replacing with bilayer buffer several times. Then 2.5 μL of AuNP/CTxB or AuNP/streptavidin solution was deposited and allowed to incubate for 5 min. Excess AuNPs were rinsed away with 1 mL bilayer buffer prior to imaging.

Imaging setup: Imaging was performed on an iSCAT microscope consisting of a wide-field channel (445 nm illumination, with beam scanning over a sample area of 50 μm $\times$ 50 μm) and a fast channel (532 nm illumination, under-filling the objective to produce a FWHM of approximately 4 μm.) The magnification in the fast channel yielded an effective pixel size of 106 nm. An incident power of 20-30 kWcm^{-2} was used for data collection at 50 kHz with 10 μs exposure time.

Data acquisition: Due to the fast movement of the AuNP/CtxB/GM1 receptor complexes and the small field-of-view in the high speed imaging channel, the data on

receptor mobility was acquired by an automated custom trigger-sequence operating in real-time. This automation removes the potential for selection bias introduced by user-triggering, and allows a higher throughput than manual acquisition. The triggering sequence operates by polling every millisecond whether a subset of frames (50 images per ms) contains a diffraction limited spot with contrast and size between set bounds, and if these conditions are satisfied begins recording for 50,000 frames.

MSD analysis: To examine the time dependence of particle mobility quantitatively, we calculated the mean-square displacement (MSD) as a function of the time interval [54]. Using the relationship MSD $\propto \Delta t^{\alpha}$, we can classify the motion of the particle based on the value of the anomalous diffusion coefficient α, with $\alpha = 1$ indicating Brownian diffusion and $\alpha \neq 1$ indicating anomalous diffusion. A logarithmic plot of the diffusion coefficient versus time has the slope (α - 1) and thus provides a convenient representation of the nature of the motion: a slope of zero indicates Brownian diffusion, while negative and positive slopes represent sub- and superdiffusion, respectively.

5.3 Results

5.3.1 GM1 diffuses anomalously in SLBs on glass substrates

Native GM1 molecules labelled with $\phi = 40$ nm AuNP-CTxB were tracked in the benchmark assay consisting of an SLB (0.03 mol% GM1) formed on a plasma-cleaned glass coverslip. Figure 5.2 shows a sample trajectory recorded at 50 kHz, the corresponding time traces of the x and y coordinate and the average diffusive plot of all recorded trajectories.

All of the AuNP/CTxB/nt-GM1 complexes exhibited anomalous diffusion, with periods of confined motion on 10s of ms time scales. The time-dependent mobility exhibits a negative slope up to 10 ms, where the diffusion coefficient plateaus at 0.09 μm^2 s^{-1}. This agrees with error bars with the value measured independently by fluorescence correlation spectroscopy of 0.14 μm^2 s^{-1} [65].

5.3.2 Effect of substrate: Brownian diffusion is restored on mica

To investigate the potential role of membrane-substrate interactions, we tuned the interactions by using freshly cleaved mica instead of plasma-cleaned glass coverslips. Analysis of the time-dependent mobilities of the $\phi = 40$ nm AuNP/CtxB/GM1 complexes indicated Brownian motion for all time-scales longer than 100 μs. Trajectories recorded on mica were typically shorter ($2\times$ 10^4 vs 5×10^4 data points) than those acquired on glass due to the faster movement of the probe across the field of view.

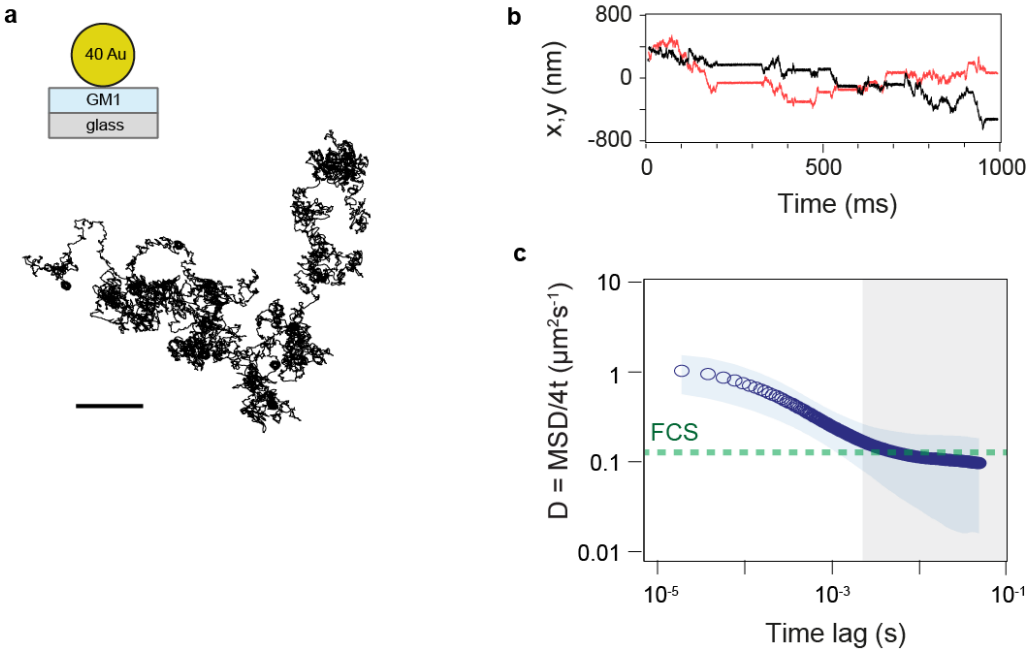


Figure 5.2: Diffusion of $\phi = 40$ nm AuNP-CTxB-labelled nt-GM1 in an SLB formed on a glass substrate. a) Sample trajectory and b) corresponding time traces x(t) and y(t). c) Time-dependent mobility of all acquired trajectories. The open circles represent the mean behaviour, and the blue shaded area is the standard deviation resulting from inhomogeneous broadening. The grey shaded out region denotes the typical time scales probed by fluorescence SPT experiments. The dotted green line shows the macroscopic diffusion coefficient measured by fluorescence correlation spectroscopy [65]. Scale bars: 200 nm. Total number of frames used for the log-log plots: 2.05×10^6. Number of data points per trajectory: 5×10^4.

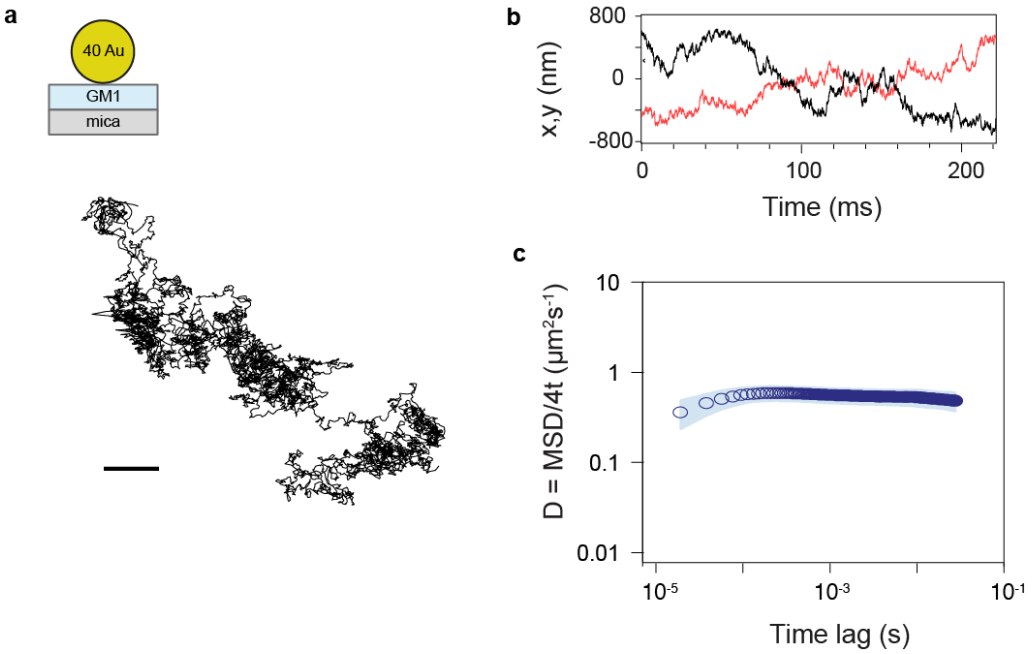


Figure 5.3: Brownian motion of GM1 in supported lipid bilayers on mica substrates. a) Sample trajectory and b) corresponding time traces x(t) and y(t). c) Time-dependent mobility. Number of data points per trajectory is 2×10^4 on average. Scale bars: 200 nm. Total number of data points used for constructing log-log plots is 3.1×10^5.

5.3.3 Effect of label size: Diffusion is affected on short time intervals only

Tracking was also performed with a $\phi = 20$ nm gold label to investigate the existence of any label size - dependent behaviour, which could be attributable to crosslinking of the gold nanoparticle to the membrane. Examination of the time-dependent mobility indicated comparable behaviour of $\phi = 20$ nm and $\phi = 40$ nm AuNP-labelled GM1, both showing subdiffusive lateral motion on the 20 μs to 10 ms time scale and Brownian diffusion at longer times (Figure 5.4).

Interestingly, a difference in the slope of the time-dependent mobility is evident in time lags up to 100 μs where the $\phi = 40$ nm AuNP label shows an approximately flat slope, while the $\phi = 20$ nm AuNP label shows a negative slope. If cross-linking was occurring to a greater extent for $\phi = 40$ nm AuNP labels, a slower mobility would be expected for all time delays. The difference in mobility at short time lags is therefore likely to be a measurement artefact, as discussed in Section 5.4.3.

5.3.4 GM1 structure modification: unsaturated tails restore Brownian diffusion

To further investigate the reason for anomalous diffusion, we modified the potential for interleaflet coupling between GM1 hydrocarbon chains by replacing the native GM1 (nt-GM1) with an analogue (DO-GM1) that has the unsaturated glycerophospholipid 1,2-dioleoyl-sn-glycero-3-phosphoethanolamine (DOPE) in place of the naturally occurring sphingosine base.

Tracking the motion of DO-GM1 on plasma-cleaned glass substrates using $\phi = 40$ nm AuNPs revealed purely Brownian diffusion at delays > 100 μs. Upon examination of individual trajectories for DO-GM1 on glass, we found only

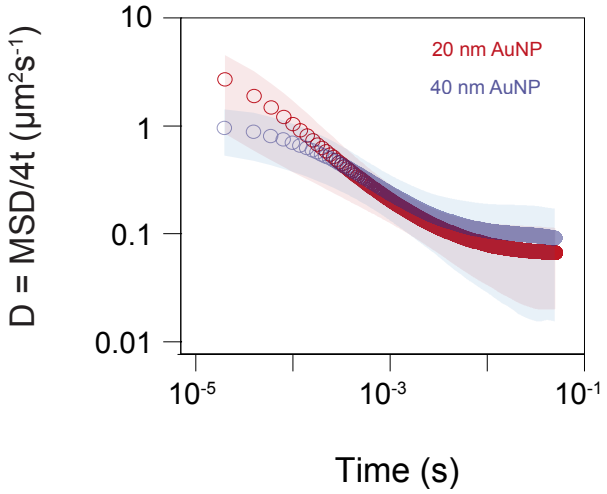


Figure 5.4: Time-dependent mobility of GM1 measured with $\phi = 20$ nm and $\phi = 40$ nm AuNP labels. The open circles represent the mean behaviour of all acquired trajectories, and the shaded area is the standard deviation resulting from inhomogeneous broadening. $\phi = 20$ nm AuNP data is shown in red, and $\phi = 40$ nm AuNP data is shown for comparison in blue. The total number of frames used for the log-log plots: 1.75×10^6 ($\phi = 20$ nm AuNP) and 2.05×10^6 ($\phi = 40$ nm AuNP). Number of data points per trajectory: 5×10^4.

extremely rare and short-lived binding events that under a macroscopic diffusion analysis were representative of Brownian motion.

Replacing the GM1 lipid with a simple phospholipid DPPE, containing two saturated tails, but lacking the glycolipid headgroup similarly restored Brownian motion.

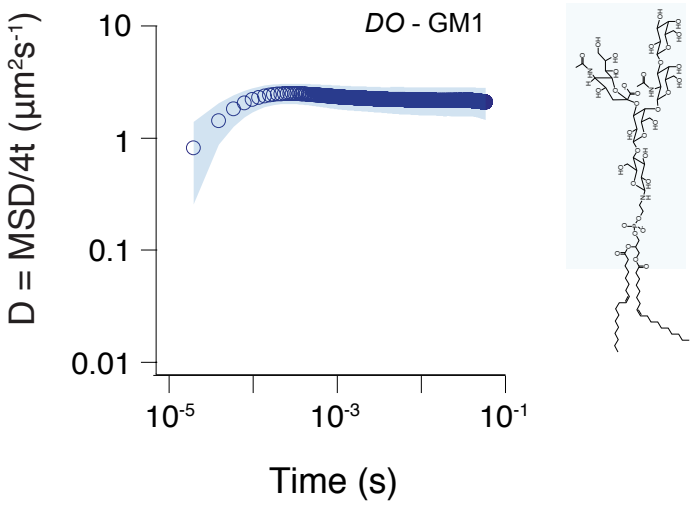


Figure 5.5: Brownian motion of GM1 with modified lipid tail groups in supported lipid bilayers on glass substrates. Time-dependent mobilities of $\phi = 40$ nm AuNP/CTxB/DO-GM1 on glass. Number of data points per trajectory: 2×10^4. Total number of data points used for constructing log-log plots is 1.07×10^6.

5.3.5 Effect of varying GM1 concentration

Model membranes containing GM1 have been shown to form nanoscopic clusters (radius = 8 nm) [195] at GM1 concentrations between 1 - 4%. To investigate the potential effect of clustering of GM1 on single molecule mobility, we varied the GM1 concentration and examined whether this has an effect on the fraction of time the particle is confined.

If confinement is caused by trapping within clusters of GM1 molecules, we would expect that raising GM1 concentration would result in an increase in the fraction of time the particle is confined. We note that this holds whether increased concentrations of GM1 results in growth of cluster sizes or in an increase in the number of clusters. To test this hypothesis, we determined this fraction for all GM1 concentrations measured (0.03 - 1 mol%). A confinement event was defined as when

the label travels less than 50 nm in 10 ms, as inferred from D = 1 $\mu m^2 s^{-1}$ of free diffusion, that is, an average travel of 200 nm in 10 ms. We found that the fraction of confinement is essentially independent of GM1 concentration, with the average of all concentrations being 0.72±0.03 (Figure 5.6). The lack of any concentration dependences indicates that GM1 clusters are either not involved in confining single GM1 molecules, or that they are not the limiting factor determining trapping.

In contrast, all control experiments exhibited a negligible confinement fraction and zero slope at Δt >100 μs in the corresponding log-log plots of diffusion coefficient versus time. The control experiments included the following: tracking biotinylated 1,2-dihexadecanoyl-sn-glycero-3-phosphoethanolamine (DPPE) in DOPC bilayers with streptavidin-functionalised AuNPs on plasma-cleaned glass substrates in the absence and presence of nt-GM1 (1.0% DPPE, 1.0% GM1); DO-GM1/CTxB at various receptor concentrations on plasma-cleaned glass (0.03 and 1% DO-GM1); and nt-GM1/CTxB on freshly cleaved mica (0.03% GM1) (Figure 5.6).

To examine the transient immobilisation events in more detail we combined all confinement events for each GM1 concentration and superimposed the spatial distributions. At the 0.03% nt-GM1 concentration (Figure 5.7a), the combined spatial distribution was well described by a Rayleigh distribution, indicating that the confinement distributions were mostly Gaussian-like. This is consistent with a physical model wherein the GM1 molecule is immobile and the gold nanoparticle is localised within a cone angle determine by the linker flexibility. Given the spatial precision of our measurements, we cannot distinguish between a completely immobile pinning site and a region up to approximately 10 nm in diameter.

As the GM1 concentration increased 33-fold to 1.0%, however, the fit to the Rayleigh distribution deteriorated. To investigate the cause of this deviation, we studied the confinement events individually. In addition to Gaussian-shaped confinement events, we observed a distinct population of confinement events exhibiting two to

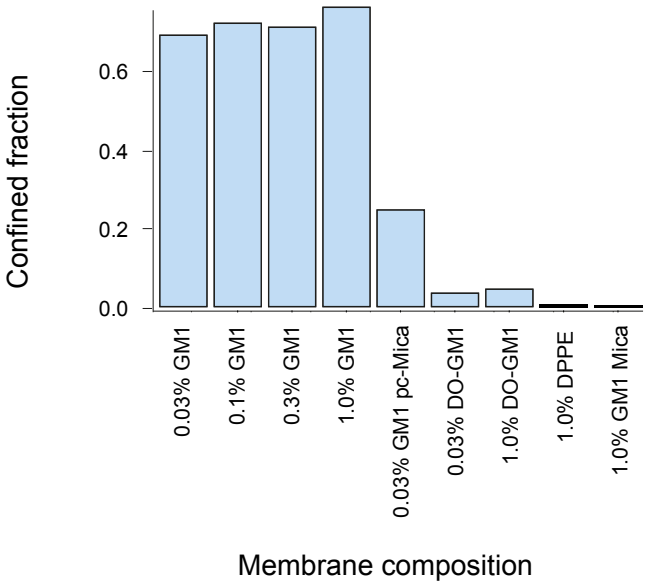


Figure 5.6: Fraction of time that GM1 is confined, for different nt-GM1 concentrations in DOPC SLBs on glass, synthetically modified GM1 (DO-GM1) on glass, DPPE with a biotin/streptavidin linker in the presence of nt-GM1 on glass, and nt-GM1 on freshly cleaved and plasma-cleaned mica. The minimum usable concentration (0.03%) was defined as the lowest concentration where specific binding of CTxB-labelled nanoparticles was still observed.

five binding sites that were revisited frequently (Figure 5.7d). The deterioration in the Rayleigh fit is likely explained by a greater number of these events.

To test this assumption, we separated the confinement events into two categories: Gaussian-like and ring-like. For classification, each confinement site was fit to a Rayleigh distribution and the coefficient of determination, R^2, was calculated. All confinement events with R^2 >0.95 were included in the averaged Gaussian-like sites. As the sites with low R^2 values contain both ring-like confinement events and other non-Gaussian shapes, the ring-like sites were selected by thresholding the standard deviation of distances from the confinement center of mass over the overall confinement to be smaller than 0.45. The optimum ratio was determined visually by inspecting the resulting averaged spatial distributions. Figure 5.7c

shows the super-imposed spatial distributions for all confinement events at 0.03% GM1, separated into Gaussian-like and ring-like categories.

Examining the Gaussian-like events only, we fit the super-imposed distributions for each GM1 concentration to a Rayleigh function. While we expected the fits to yield the same radius, interestingly, we observed that the radius scales with nt-GM1 concentration (Figure 5.7b).

5.4 Discussion

5.4.1 Minimum components for anomalous diffusion

The observation of anomalous diffusion as a function of lipid tail structure and substrate properties suggests that there are two critical components that control time-dependent mobilities for GM1 in SLBs: the existence of sites on the substrate capable of immobilizing GM1 molecules, and the presence of straight, elongated aliphatic chains in GM1 that allow a direct interaction between GM1 molecules in both leaflets.

Given the possibility of defects in SLBs, it is important to assess the possibility that anomalous diffusion is a result of bilayer imperfections. First, defects greater than a few tens of nanometers are readily detectable in iSCAT due to their different refractive index. The ability to distinguish a bilayer from the bare glass surface, or from deposited vesicles, has been exploited in previous work to examine the formation of SLBs [122]. If undetectable defects were responsible, we would expect to observe anomalous diffusion in all experiments, regardless of the lipid structure or substrate. Even if defects were more likely to form on glass than mica, or were related to the lipid headgroup, we would expect the same diffusive properties for DO-GM1 and nt-GM1, which is not the case.

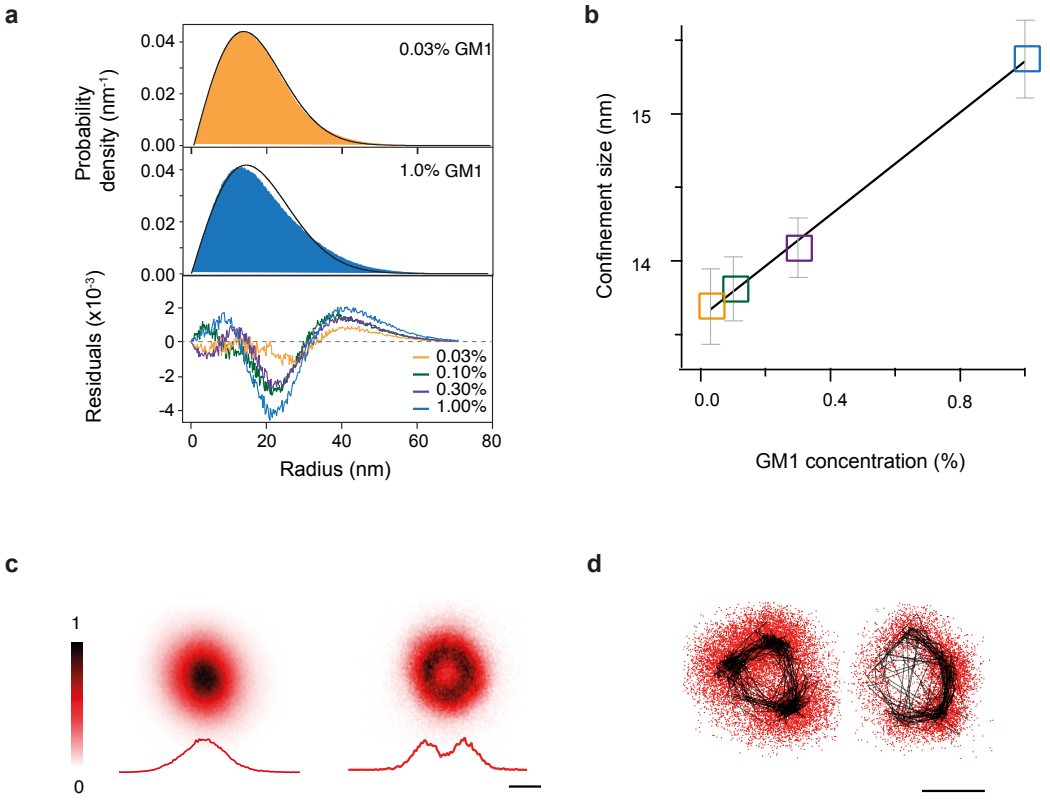


Figure 5.7: (a) Radial probability density plots and corresponding fits to a Rayleigh distribution for all confinement events recorded at 0.03% and 1.0% nt-GM1 concentrations and residuals from the the Rayleigh fits for all nt-GM1 concentration. The distribution histograms were computed from 2×10^6 data points in each case. (b) Radius of all confinement events, determined from the Rayleigh fits. Error bars are the standard deviation of the mean confinement size. (c) Gaussian-like (left) and ring-like (right) spatial distributions of confinement events at 0.03% GM1 on glass obtained by averaging 228 and 93 confinement events, respectively. Horizontal cuts through the distributions are shown for clarity. Scale bar is 20 nm. (d) Individual ring-like confinement events exhibiting 2 - 5 distinct binding sites. The black lines represent trajectories after averaging 25 consecutive frames, equivalent to 0.5 ms time averaging, and help visualise the stepping motion between GM1 receptor sites. Scale bar: 20 nm.

The relatively large gold nanoparticle label has also been suggested to induce time-dependent mobilities by cross-linking or unwanted label-membrane interactions. We emphasise that, with the exception of measurements of native GM1 on plasma-cleaned glass, all trajectories exhibited Brownian motion for all time delays, clearly indicating that even large labels ($\phi = 40$ nm) do not intrinsically produce anomalous diffusion. Nevertheless, care must be taken to avoid potential artefacts. For the majority of assays reported here, almost all labels diffuse freely initially, but become immobile within an hour after addition of AuNPs, likely due to accumulation of receptors on the label surface with time. The same behaviour is observed for both GM1/CTxB and for DPPE tracking and is thus likely a general consequence of receptor aggregation rather than substrate and leaflet coupling-induced transient binding.

5.4.2 Mechanistic model

Our ability to reveal the position of the label during confinement events with ~ 2 nm spatial accuracy or greater provides important clues to the nanoscopic origin of anomalous diffusion. In particular, we are able to address the question of whether confinement is caused by the GM1/receptor complex being bound within a region, or immobilised at a single point. If the confinement zone is due to a single pinning site that is nanoscopic in size, we expect to observe the spatial distribution to reflect the freedom of motion of the gold nanoparticle, determined by the linker length and flexibility. To illustrate this, it is helpful to consider the molecular details of the tracking assay 5.8. When drawn to scale, it is clear that for a nanoparticle label with a single immobilised CTxB subunit on the membrane, some flexibility remains due to the connection between GM1 and the center of mass of the particle. Simple geometric arguments suggest that such nanoscopic rocking of the label can induce variations in the center of mass on the order of 15 nm.

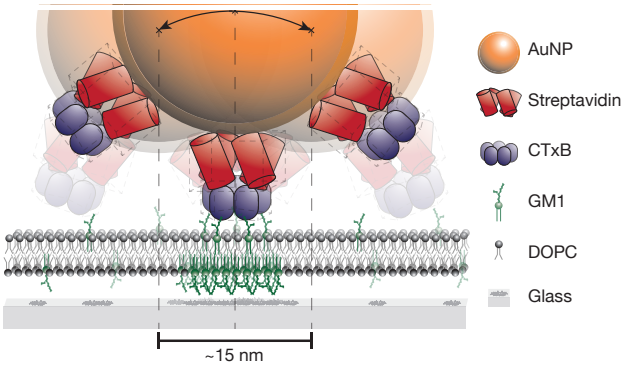


Figure 5.8: Schematic of the tracking assay during a transient binding event drawn to scale for a $\phi = 20$ nm AuNP. The curved arrow indicates the achievable nanoscopic rocking motion of the label and the dashed lines the achievable fluctuations in the center of mass of the label even for a completely immobilised CTxB.

If the centre of mass of the label can be localised on a timescale shorter than that of the rocking motion, such fluctuations result in a 2D Gaussian spatial distribution around the center of mass position, like that shown in the top image in Figure 5.7c. Spatial patterns resulting from the particle jumping between discrete positions, such as that shown in Figure 5.7d may be envisioned as occurring when a second surface-bound CTxB on the nanoparticle transiently binds to another GM1, which may be diffusing. Although the GM1/CTxB dissociation constant is very low ($K_d \sim 10^{-8}$), we observe this behaviour frequently.

We would expect that, on average, these multiply bound particles yield trajectories centred around an immobilised central CTxB. The radius would be comparable to the maximum motion of the center of mass of the label. If the lipid is immobilised on a molecular scale during confinement events, we would not expect the size to vary as a function of GM1 concentration. Our results, however, show a slight increase in radial density of all (combined Gaussian and ring) confinement events with increasing GM1 concentration. This is consistent with an increased probability of multiple membrane interactions with increasing GM1 in the bilayer. At low GM1 concentration (0.03 %) there is ~ 1 receptor in an area of 40 nm^2 meaning that other CTxB subunits on the

AuNP will rarely encounter any GM1 receptors upon approaching the membrane during nanoscopic rocking. As a result, we obtain an almost perfect fit to a Rayleigh distribution (Figure 5.7a). For higher GM1 concentrations, the deviation between the radial probability density histogram and the Rayleigh fit increases (Figure 5.7b and c). Even for Gaussian-like confinement events, an increase in nearby GM1 concentration should lead to an increase in the apparent confined area because nanoscopic rocking will result in the particle, on average, spending more time near the membrane surface due to transient binding with additional GM1, even if it does not lead to cross-linking and long-term multiple binding.

The tight lateral confinement on the <20-nm scale and the observation of ring-like confinement events both demand transient immobilisation of a single membrane-bound CTxB subunit on the nanometer scale. Given that transient binding requires both native GM1 lipid tail domains and a plasma-cleaned substrate as evidenced by the absence of confinement on mica and with DO-GM1, we propose that the most likely origin is clustering of GM1 on the lower leaflet in patches determined by non-uniformities in the underlying surface chemistry or physical roughness of the coverslip. The fact that the probability of confinement does not depend on GM1 concentration suggests that the density of substrate sites is the limiting factor in the number of confinements observed.

Spatial variations in the surface chemistry of glass could potentially be induced by the plasma cleaning process, which strongly increases the hydrophilic nature of glass [196]. Hydrogen bonding interactions with the substrate have been shown to be particularly pronounced for lipids with oligosaccharide headgroups [197], hence high densities of hydroxyl groups could feasibly immobilise GM1 lipids. Although in principle one could envision that a single pinned GM1 molecule is responsible for immobilisation of five CtxB-bound GM1 molecules on the outer leaflet, such a prospect appears energetically unlikely.

We also consider the possibility that physical roughness of glass could induce immobilised GM1 clusters. AFM studies show that KOH treated glass has a surface roughness of approximately 2 Å RMS [198]. The long, saturated acyl chains of GM1 might cluster in the lower regions of the surface, to accommodate the longer tail length of the GM1 lipids. Whether interleaflet communication is achieved by interdigitation of lipid tails, or by changes to the topography and electrostatic properties of the surface (with tails meeting at the bilayer midplane), transient nanoscopic confinements could occur.

In summary, we conclude that the lower leaflet is likely scattered with numerous <10 nm patches of high GM1 density with higher viscosity that communicate with the upper leaflet through transbilayer interactions, leading to transient ($\sim$ 10 - 100 ms) nanoscopic confinements.

5.4.3 Static and dynamic error at short time lags

Comparison of the diffusive plots for $\phi = 40$ nm gold and $\phi = 20$ nm gold labelled nt-GM1 on glass shows a significant difference for short time delays (100 μs), but essentially the same diffusive behaviour for delays longer than 100 μs. This implies that the $\phi = 20$ nm gold label moves faster on the shortest timescales. This could be explained by one of three possibilities: the GM1 receptor complex moves faster when it has a smaller label; the motion of the GM1 complex is the same in both cases, with the faster diffusion for $\phi = 20$ nm gold arising from greater flexibility of the label/linker; or the motion of GM1 and the label are the same in both cases, however the poorer localisation accuracy for $\phi = 20$ nm gold vs $\phi = 40$ nm gold (2.2 nm error vs 0.7 nm error, respectively) leads to apparent faster diffusion on short time lags.

If the number of length of confinement events was significantly greater for the

$\phi = 40$ nm gold-labelled GM1 compared to the $\phi = 20$ nm gold-labelled GM1, we would expect a lower macroscopic diffusion coefficient for the $\phi = 40$ nm gold, which is not the case. We can therefore rule out the first possibility. Regarding the second possibility, we would expect a larger range of motion for the freely diffusing $\phi = 40$ nm gold label, as the length of the label+linker is greater. This would lead to a higher diffusion coefficient for the $\phi = 40$ nm gold, which is the opposite of the effect observed. Therefore the primary effect must be due to the difference in localisation error. In single particle tracking, this error is named "static error" and has been described mathematically by Savin [192].

Another apparent anomaly is visible in the trajectories of GM1 in SLBs prepared on a mica substrate. While we would expect the diffusive plots to have a slope of zero for all time lags, indicative of Brownian motion, this is only true of time delays greater than 100 μs. As the delay decreases from 100 - 20 μs, the apparent diffusion coefficient becomes slower. Given that we observe no directed motion in the trajectories which could produce this super-diffusive trend, we consider the possibility of a second artefact that causes the true displacement over short length and time scales to be underestimated. Such an artefact has been previously described and is named "dynamic error" [192], referring to the error that arises when the particle moves a significant distance during the exposure time. This results in the time-averaged position being measured, which underestimates the diffusion coefficient. The effect is greatest for the shortest time lag, and decreases as the time lag grows relative to the exposure time.

Overall, we therefore expect the diffusive plots to reflect the net effect of dynamic and static error, with the exact slope of the curve on short time lags determined by the balance of these two artefacts. In particular, a slope of zero is not necessarily indicative of Brownian motion - the localisation error and exposure time as a function of time lag must both be evaluated, and ideally the data must be compared to a

control experiment in which the motion is known to be Brownian on all time scales.

The slope of the diffusive plot over short time delays has been an important component in the formulation of the picket-fence model. This predicts that lipid and protein diffusion is corralled by the actin-based cytoskeleton, resulting in time-dependent mobilities that are Brownian on sub-ms time scales when diffusion is free within the compartment boundaries, subdiffusive from 1-10 ms when molecules sense the boundaries and hop to neighbouring compartments, and Brownian again (with an order of magnitude lower diffusion coefficient) on time scales longer than ∼30 ms, at which point hop-diffusion is no longer observed [199].

Our results demonstrate the difficulty involved in distinguishing a transition from anomalous toward Brownian motion on short time scales due to contributions from static and dynamic errors, even with sub-nm localization precision and exposure times of only 10 μs. This implies that confident identification of the mechanism causing anomalous subdiffusion will also be subject to these effects.

5.5 Summary and outlook

Our results have important implications both for diffusion studies of membrane components at very high speeds and for the role of interleaflet coupling in transbilayer communication. The results presented here provide a general mechanism for communicating information related to structural and dynamic changes occurring on one side of a bilayer towards the other leaflet without the use of transmembrane entities.

This work also provides a benchmark system for comparison with other high speed particle tracking experiments. We have characterised the spatiotemporal dynamics of immobilisation due to interleaflet pinning, and in future could contrast these results with trajectories acquired on cell membranes to determine whether similar

behaviour is observed in more biologically relevant environments. We have also demonstrated that dynamic error and poor localisation precision can lead to apparent super-diffusive behaviour for 40 nm labels at short time lags. Similarly, poor localisation precision can lead to apparent subdiffusive behaviour at short time lags. It is important to consider these artefacts when using only the time-dependent diffusion to categorise single molecule motion.

Although GM1 is found only in the outer leaflet of the plasma membrane, and thus cannot be solely responsible for transbilayer communication, the results presented here provide a general mechanism by which an interaction between the cytoskeleton and the plasma membrane can limit receptor mobility in the outer leaflet even without the assistance of transmembrane components. In the future it would be important to address the question of how many lipids in each leaflet would suffice to transiently immobilize a gold nanoparticle across the leaflets. Furthermore, it would be important to investigate whether such transient immobilisation is found in asymmetric bilayers with composition similar to cell membranes and to determine the exact structural requirements for interacting molecules.

5.6 Contributions

This work is partly based on the following publication: Spillane, KM, Ortega Arroyo, J, de Wit, G, Eggeling, C, Ewers, H, Wallace, MW and Kukura, P. Interleaflet coupling and molecular pinning causes anomalous diffusion in bilayer membranes. Nano Lett. 14: 5390-5397, 2014.

Experimental work and the data analysis were performed by Dr. Katelyn Spillane, Dr. Jaime Ortega-Arroyo and myself. Specifically, I carried out the receptor titration experiments with $\phi = 20$ nm AuNPs and performed the super-resolution analysis of binding events. Measurements with $\phi = 40$ nm AuNPs on mica substrates and

with DO-GM1 were performed by Dr. Katelyn Spillane. The implementation of the high-speed data acquisition with automatic triggering was performed by Jaime Ortega-Arroyo. Dr. Ewers provided the DO-GM1 lipid and Dr. Eggeling measured the diffusion coefficient using fluorescence correlation spectroscopy.

Chapter 6

Mobility of Membrane Proteins within a Periodic Actin Network

6.1 Introduction

The cell membrane is often described as a two dimensional fluid, wherein the constituent proteins and lipids are free to move within the plane of the bilayer. While this is a useful model, it overlooks the effect of the significant fraction of transmembrane proteins that are bound to the cortical actin cytoskeleton, either directly or via peripheral actin-binding proteins. The membrane-anchored actin cytoskeleton is thought to control the mobility and spatial distribution of the remaining membrane constituents, via interaction of cytoplasmic domains of membrane proteins with the actin filaments and via collision with the immobile anchored proteins within the membrane.

The effect of actin on membrane diffusion has been difficult to observe on a spatially resolved level, due to the inherent difficulty in imaging the dense and dynamic actin network in live cells. The rate of diffusion in actin-free vesicles extracted from cell membranes and in reconstituted model membranes, is typically an order of

magnitude higher than that measured in cells, suggesting that the presence of actin significantly slows diffusion. The mechanism of actin's involvement has been difficult to study on its own, however, as the procedure for removing actin by isolating membrane vesicles results in the loss of a large fraction of membrane proteins [200, 99], and may therefore affect the diffusion not just by removing anchored molecules but also via the decrease in protein crowding and concomitant membrane viscosity.

A second approach to investigating the role of the membrane-adjacent cytoskeleton is by treating cells with chemicals that interfere with the polymerisation of actin, such as Latrunculin A [201] and Cytochalasin D [202]. Experiments have yielded inconsistent results, however, often reporting no significant effect on diffusion [203, 204]. Furthermore, chemicals that target different stages of the actin polymerisation processes differ in their effect. For example Umemura observed no effect on diffusion following treatment with Cytochalasin D, but a 50% increase in macroscopic diffusion coefficient for cells treated with Latrunculin A [84].

Alternately, one may infer the interaction of actin with the membrane by tracking single molecules at speeds fast enough to directly detect compartmentalisation of molecules within the individual spaces of the actin mesh. While single molecule trajectories recorded with fluorescent dyes at low frame rates often report Brownian diffusion [203, 204], trajectories recorded at 40 - 50 kHz with $\phi = 40$ nm gold labels consistently exhibit confinement of both lipids and proteins within apposed compartments of 30 - 700 nm [86, 84, 205, 88]. Electron tomography measurements of the actin mesh size in two cell types correspond to the compartment sizes measured by high speed SPT [88]. Rapid diffusion is observed within each compartment with diffusion coefficients for lipids, GPI-anchored proteins and transmembrane proteins in the range of 4 - 8 $\mu m^2 s^{-1}$ [86], similar to simple fluid-phase model membrane systems, while diffusion at time scales longer than the average residence time is roughly equivalent to measurements with fluorescent

dyes at comparable frame rates. As outlined in the introduction of this thesis, these high speed results apply to all measured lipids and proteins, suggesting a mechanism by which the effect of the actin boundaries is transmitted to even outer-leaflet lipids and lipid-anchored proteins. To explain this observation, Kusumi and coworkers proposed the membrane picket fence model, where transmembrane proteins anchored to underlying actin filaments acts as pickets that effectively compartmentalise the membrane, reflecting the arrangement of the underlying actin cytoskeleton. In this model, lipids and GPI-anchored proteins experience the effect of the pickets, while transmembrane proteins interact with both the pickets and with actin fence, which acts as a barrier to the cytosolic domain.

An obstacle to the widespread acceptance of this model is that it has been difficult to verify with any other techniques, as SPT stands alone in possessing a simultaneously high combination of spatial and temporal resolution necessary for direct observation of membrane compartments. The possibility that the observed behaviour is caused or amplified by the gold nanoparticle label remains a question to be proven or refuted. High speed (1 kHz) single molecule tracking of fluorescently labelled lipids and the GPI-anchored protein CD59 failed to detect actin corrals by examination of trajectories [67] . Analysis of the offset in the linear fit to the mean square displacement values as a function of time similarly showed little support for the existence of confinement on lengthscales of the size of actin compartments. The relatively slow frame rate and dynamic error, however, may have obscured the underlying motion [91]. Results consistent with the hop diffusion hypothesis have been reported in experiments in cells using FCS with variable spot size, but only for transmembrane probes [206]. GPI anchored proteins were observed to be trapped within smaller regions, corresponding to putative rafts [207, 206]. In contrast, a study of diffusion in free standing model membranes bound to actin at a variable density of sites showed a clear correlation between the picket density and a reduction in mobility of both lipids and proteins [90].

In summary, the exact mechanism(s) by which actin slows diffusion of various membrane proteins and lipids remains unclear due to the lack of any information about the spatial arrangement of actin filaments, and the trade-off between limited spatiotemporal resolution and potential artefacts associated with large labels. Whether the slower diffusion observed in live cells compared to membrane extracted vesicles and reconstituted membranes is directly correlated with the actin network, and the time and length scales on which actin controls diffusion are open questions with important implications for the mobility of molecules in cell membranes.

6.1.1 The periodic actin-spectrin cytoskeleton in neurons

Recently, a repetitive pattern of sub-membrane actin rings was discovered in the neurites of embryonic hippocampal neurons [26, 27]. The pattern is established within the first week of development in embryonic cell culture and is very stable over time. As such, this provides an ideal model system in which to investigate the effect of actin on membrane diffusion with exact knowledge of the size, relative position and geometry of the cytoskeletal fences.

The periodic ring structure was first identified using stochastic optical reconstruction microscopy (STORM) [26] in 2013, and later confirmed using Stimulated Emission Depletion (STED) [27]. The rings were found to be connected by spectrin tetramers, and spaced 180 - 190 nm apart along the entire length of the axon, with a periodicity strong enough that a Fourier transform of the super-resolution images reveal the ring spacing as well as higher harmonics. The initial experiments only observed actin rings in axons, however subsequent development of a new, actin-binding fluorescent probe, SiR-actin [208] indicated the ubiquity of the rings in dendrites as well [27], though the pattern was less consistent than in axons, and not observed in all cells.

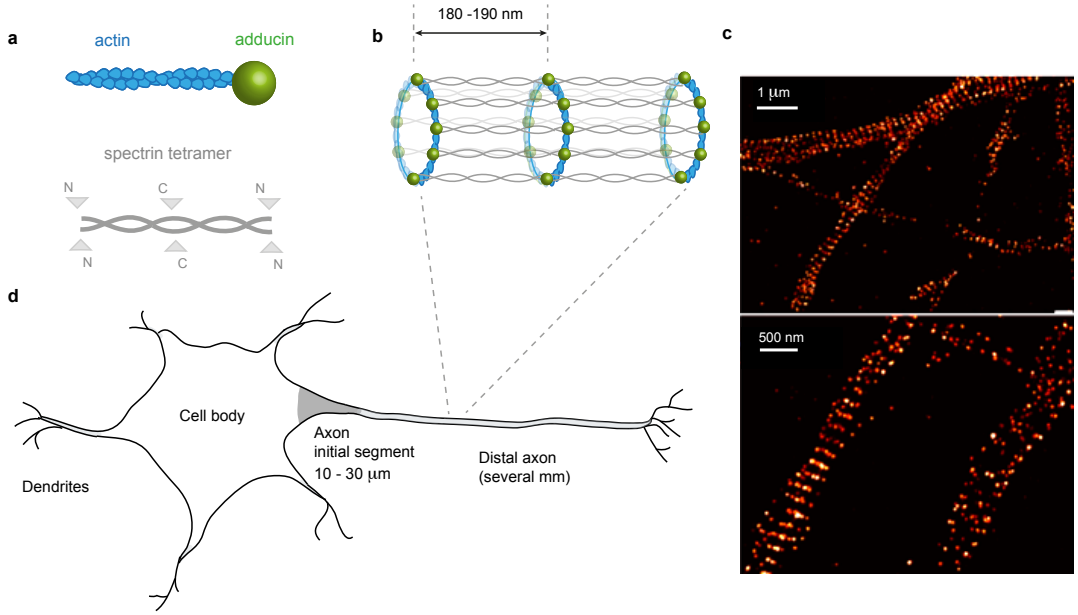


Figure 6.1: A schematic of the actin-spectrin cytoskeleton in neuronal axons and dendrites. Super-resolution STORM data is consistent with the cortical cytoskeleton of axons being comprised of short actin filaments that are capped by adducin at one end and arranged into a ring structure around the circumference of the axon. Spectrin tetramers connect to the actin filaments, forming the periodic 180 - 200 nm spacing. Figure adapted from Xu, 2013 [26]. c) Super-resolution images of the cytoskeleton obtained by labelling the β4-spectrin in a hippocampal neuron with anti-β4-spectrin- AF647, after permeabilisation of the membrane and cell fixation. Data acquired by David Albrecht and used with permission. d) A schematic of a neuron at a developmental stage between DIV 5 - 10, showing the cell body, the axon initial segment, the distal axon and the dendrites.

Based on multi-colour super-resolution imaging of the actin-linking protein spectrin, and the actin-capping protein adducin, Xu and coworkers proposed that the spacing could be explained by actin rings being interconnected with spectrin tetramers, a pattern that is known to occur in red blood cells. Actin and adducin were found to colocalise, while spectrin (stained at the C terminus) was 90 degrees out of phase, allowing a model of the actin-spectrin-adducin ultra-structure to be built, shown in Figure 6.1.

6.1.2 Aims of this work

In this work, we perform high speed tracking of single molecules at up to 40 kHz in embryonic hippocampal neurons, to directly correlate patterns in mobility of transmembrane and lipid-anchored proteins, with the underlying actin cytoskeleton. Based on the picket-fence model, we expect to observe fast, Brownian diffusion within compartments that are approximately 180 - 190 nm in size, with occasional hopping between compartments, resulting in a macroscopic diffusion coefficient at least an order of magnitude smaller than the microscopic value. We examine two transmembrane probes that differ only in the size of their cytosolic domain to gauge the relative influence of direct interaction with actin compared to interaction with immobilised pickets.

6.2 Methods

Summary: Embryonic hippocampal neurons were transfected to express recombinant membrane protein constructs including YFP or GFP moieties, which were used as epitopes for the binding of gold nanoparticles via nanobodies to the respective fluorescent proteins. Cells were imaged with iSCAT on DIV (Days in Vitro) 6 or 7, roughly two days after the ring structure first became visible. SPT trajectories were recorded with localisation accuracy of $\sigma = 3.1$ nm on average, at frame rates between 2 - 40 kHz.

Membrane Protein Constructs: Three different protein constructs were used, including two transmembrane proteins with a short and long cytoplasmic tail respectively, and a GPI-anchored protein that is attached to the outer leaflet.

The short transmembrane protein construct, named L-YFP-GT-46, is an artificial secretory protein containing a signal sequence, YFP, a consensus N-glycosylation

site, the transmembrane domain of the LDL receptor, and the cytoplasmic tail of CD46 [209]. The extended transmembrane protein construct, named L-YFP-TM-mHD-GT-46, was created by David Albrecht based on the same design as the L-YFP-GT-46 construct, but with an additional fluorescent protein (mHoneydew, a mutant version of RFP) inserted in the cytoplasmic tail domain. The outer-leaflet protein is a GFP attached to a GPI anchor.

The plasmids used to express the GPI-GFP protein and the L-YFP-GT-46 protein were a gift of Patrick Keller [210]. The composition of the plasmid DNA sequences are shown in the thesis of David Albrecht. [211].

Cell culture: The preparation and cultivation of primary hippocampal neurons from E18 Sprague-Dawley rats was performed by collaborators at Kings College London, following a simplified version of the method described in [212], described in detail in the PhD thesis of David Albrecht [211]. Briefly, the hippocampi were dissected out under a table-top microscope and incubated for 10 min at 37 °C in 0.05 % Trypsin ETDA (Life Technologies). The hippocampi were washed three times in 3 ml HBSS and transferred into a 15 ml falcon tube with 3 ml plating medium dissociated by mixing thoroughly with a 1000 μl pipette.

After attaching to the surface, the coverslips were placed into 6 cm dishes containing 300,000 cells, as a minimum number of cells were required for normal development and survival. Cells were maintained in a 37 °C humidified CO_2-controlled incubator and fed every 2-4 days by adding 0.5 ml of fresh neurobasal medium or by replacing 0.75 ml of the medium with 1 ml fresh neurobasal. On DIV 3 cytarabine was added at a final concentration of 5 μM to inhibit growth of dividing cells. Under ideal circumstances, neurons were viable for >8 weeks.

Transfection: Neurons were transfected with plasmid DNA on the 1st or 2nd day of *in vitro* cultivation (DIV) using Lipofectamine 2000 (Life Technologies), according to the manufacturer's instructions. Expression of fluorescent fusion constructs was

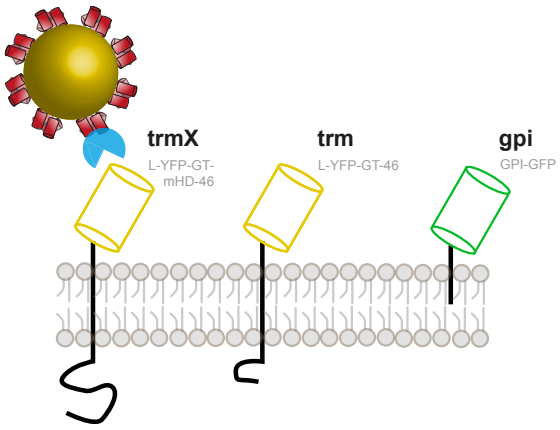


Figure 6.2: Labelling of recombinant protein constructs: GPI-GFP, L-YFP-GT-46 and L-YFP-TM-mHD-GT-46. Protein constructs were designed and expressed by collaborators as attributed in the text above.

detectable as early as a few hours after transfection and was usually stable for at least 72 hours and, in exceptional cases, more than 10 days after transfection, depending on the overall survival rate of the cultured neurons. Transfection efficiencies of 0-1% were commonly achieved, the variation largely depending on the particular neuron preparation and age of the culture. After DIV 10 transfection efficiency was greatly reduced and mortality due to the transfection reagent increased.

Gold Labelling: $\phi = 40$ nm streptavidin coated gold nanoparticles were incubated with biotinylated anti-GFP or anti-YFP nanobodies, depending on the target protein construct. The ratio of gold to nanobodies was calculated to yield 1-2 GFP/YFP binding sites per gold nanoparticle.

Imaging Procedure: Single particle tracking in live cells was performed in live-cell imaging buffer (145 mM NaCl, 5 mM KCl,10 mM Glucose,10 mM HEPES, 2 mM $CaCl_2$, 1 mM $MgCl_2$, 0.2% (w/v) BSA, 10 mM ascorbate) [213] at ambient lab temperature $\sim$ 23 °C. Cells were deemed healthy when they showed no significant morphological changes, prior to or during imaging.

Nanobody conjugated gold was added directly to the sample dish. First, the majority of the buffer medium was removed (to facilitate faster diffusion of gold to the cell surface), then 5 - 10 μL of 10 nM antiGFP-gold nanoparticles was added. In initial experiments, we observed the gold nanoparticles approaching and eventually binding to the cell, while on the sample stage. As the neurites cover a very small fraction of the total area of the sample dish, binding was relatively slow. We found that is was optimal both in terms of the speeding up the rate of gold binding and increasing cell survival, to return the cells to the incubator for 20 - 30 minutes after addition of gold, before imaging again with iSCAT.

Gold nanoparticle labelled proteins could be identified by a rapidly varying contrast that ranged from -40% to $+40\%$, and by their fast movement up and down the neurite. Usually, tens of particles were attached to each transfected cell. We did not observe any gold particles attached to non-transfected cells (which are visible in iSCAT but do not fluoresce). To remove background originating from the freely diffusing gold nanoparticles, the supernatant was replaced 3 - 4 times with fresh medium.

We note that while much attention in the field of neuron membrane organisation is devoted to the axon initial segment, a specialised part of the neuron involved in maintaining neuron polarity, we are unable to image this region with iSCAT due to the high scattering background in this region. Our work instead focuses on the peripheral neurites, where we have been able to achieve excellent signal to noise ratios and localisation errors comparable to imaging in SLBs (the localisation accuracy is shown in Chapter 3).

Figure 6.3 shows an example field of view containing several neurites, overlapping to form bundles at some locations. Tracking was performed on isolated neurites, where the gold particle could be clearly detected with high signal to noise ratio (typically 30 - 40 at the maximum contrast) after static background subtraction.

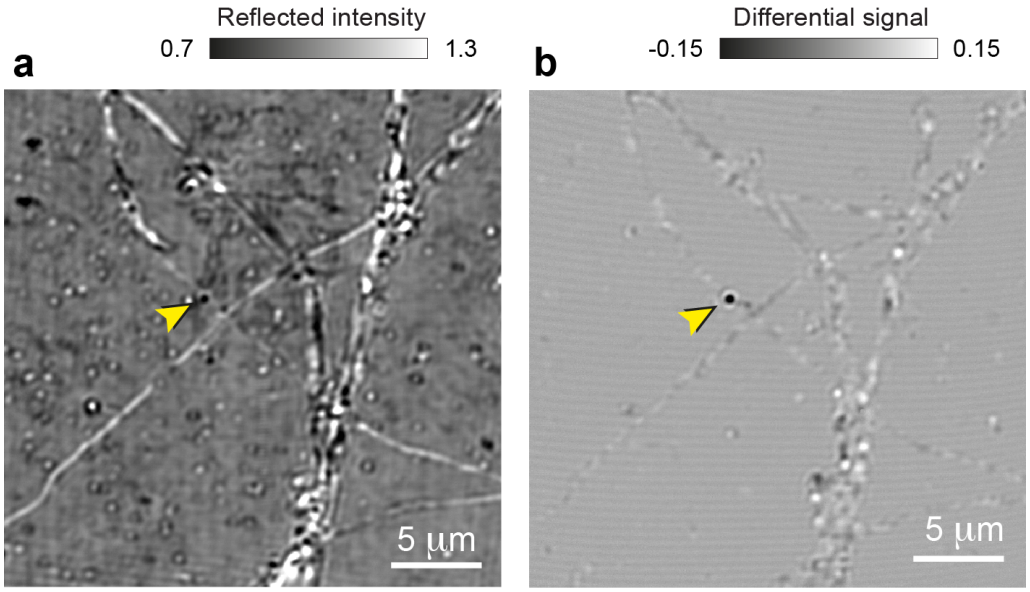


Figure 6.3: a) An example iSCAT image of the neuron cell culture, and b) The same field of view, after subtracting the median pixel value of a stack of images. Note all static features are subtracted, and the moving gold particle is easily detected. The gold particle is marked by an arrow in both the raw and background subtracted image images. Neurites that are not well attached to the surface and/or generate a high contrast, particularly bundles of overlapping neurites, also produce a non-zero background.

Gold nanoparticles were identified in the scanned illumination channel and the stage was moved to bring these particles to the centre of the non-scanned illumination channel, for recording at high speeds.

Data acquisition: Tracking was carried out according to the method described in Chapter 3. 3D tracking using astigmatism in the fluorescence detection path was also performed simultaneously with iSCAT tracking. The sample was focused at the position that minimises the average fwhm of the gold particle.

Following acquisition of iSCAT data, cells were fixed for subsequent super-resolution imaging, to confirm the integrity of the actin-spectrin network. Super-resolution imaging by STORM was carried out by collaborator David Albrecht at Kings College London.

Cleaning and pre-processing of high speed trajectories Trajectory data was cleaned by removing localisation events with an error >6 nm, where the error was calculated from the least squares fitting routine as described Chapter 3. Approximately 80 - 90% of frames met this criteria, the exact percentage depending on the background noise in each trajectory. Retaining the time coordinate of each valid frame, the diffusion coefficient and standard deviation were subsequently calculated over a running window of 5 ms (200 frames at 40 kHz). Only windows containing at least 30% valid frames were considered.

To analyse trajectories for periodicity corresponding to the actin ring spacing, each trajectory was oriented so that the x axis was aligned with the long axis of the neurite. Typically the neurite was approximately linear over the length of the trajectory (limited by the field of view of 4 μm). Where necessary, the trajectory was fragmented in time such that the region of the neurite traversed by the probe was approximately linear. The outline of the neurite could be approximated both from the trajectory and from the background image generated by calculating the median value of each pixel. As the mobile AuNP spends only a small fraction of the trajectory on each pixel, the background image contains only non-mobile contributions to the contrast i.e. the neurite. Conveniently the outline of the neurite was easy to detect in iSCAT, having a contrast of $\sim$0.15% as shown in Figure 6.3a.

6.3 Simulations

The picket fence model assumes that membrane proteins and lipids diffuse freely within a compartment with diffusion coefficient D_{micro}, but have a low probability of passing the actin fence. Knowledge of the actin fence spacing allows us to set up a simple model to examine diffusion within a 1D array of semi-permeable barriers.

Trajectories were generated by simulating a 2 dimensional random walk with impermeable boundaries ($P_{reflection} = 1$) at y = $\pm$ 200 nm (assuming a typical neurite diameter of 400 nm), and an array of semi-permeable boundaries ($P_{reflection}$ <1) spaced 190 nm apart along the x dimension. We set the microscopic diffusion coefficient to $D_{micro} = 5$ μm^{2}s^{-1}, which is within the range of 4.5 - 6 μm^{2}s^{-1} reported for a transmembrane protein with multiple membrane spanning domains [205]. Trajectories were simulated for two reflection probabilities to yield residence times of 7 ms ($P_{reflection} = 0.9$) and 34 ms ($P_{reflection} = 0.98$), spanning the range of reported residence times for lipids and proteins in the plasma membrane of an NRK cell with a similar mesh size of 230 nm [86]. Steps in x and y were simulated from independent random Gaussian distributions at time intervals of 25 μs (40 kHz) over a total time of 500 ms. Figure 6.4 shows a) logarithmic plots of the diffusion coefficient vs time lag for 20 simulated trajectories, (b) a sample xy trajectory $P_{reflection} = 0.98$ and 0.9, and c) the x coordinate of the sample trajectory displayed vs time.

To account for the effect of localisation error, a Gaussian distribution with $\sigma = 3.1$ nm was randomly sampled, and added to each step in the trajectory. The width of the distribution reflects the typical error from Gaussian fitting of the PSF of a $\phi = 40$ nm AuNP in trajectories recorded on neurons, as shown in Figure 3.6. The plots in Figure include this localisation error, which makes only a negligible difference to the clarity of fence boundaries in the trajectory or to the numbers in the diffusive plot. We note however that a localisation error of $\sigma = 16$ nm, typical

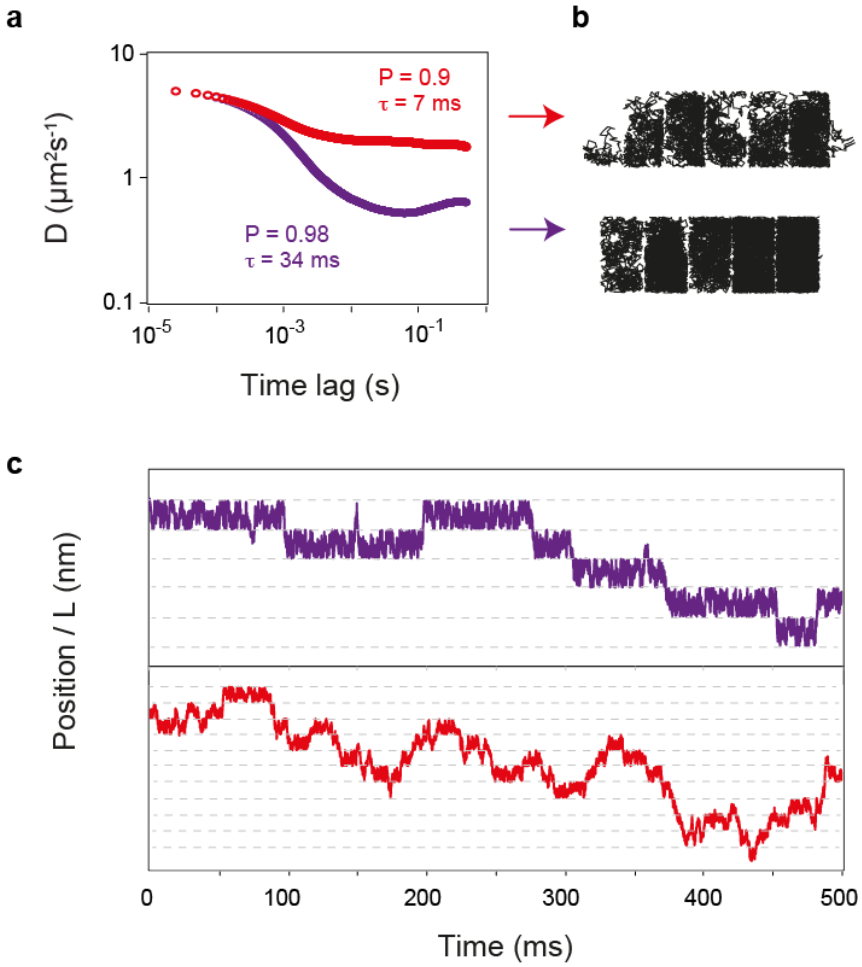


Figure 6.4: a) 1D diffusion coefficient plots of simulated trajectories of a probe diffusing with D_{micro}= 5 μm^{2}s^{-1} in a periodic array of semi-permeable barriers with spacing L = 190 nm for $P_{reflection}$ = 0.9 (red) and 0.98 (purple). The plots have been generated by averaging the diffusion coefficients vs time for 20 simulated trajectories. b) Example simulated trajectories with $P_{reflection}$ = 0.9 and 0.98. 100 ms (top) and 500 ms (bottom) of data are shown. c) The x coordinate as a function of time for the full trajectories shown in b). Grey dashed lines indicate the position of the actin fences.

of dark field scattering measurements on which the hop diffusion hypothesis is based, effectively blurs the actin boundaries in the trajectory, and yields an observed microscopic diffusion coefficient of $\sim$ 10 μm^{2}s^{-1} at the shortest (25 μs) time lag, double that of the actual microscopic diffusion coefficient. The dynamic error due to averaging of the detected position during the exposure time was not

considered, however this would lower the diffusion coefficient at the shortest time lags.

6.3.1 Autocorrelation analysis

The autocorrelation of the number of localisation events along one dimension provides a means of visualising periodicity in the density of the protein location. In neurons, we expect the density to be correlated every 190 nm, at the distance between actin rings. Applying this analysis to the simulated hop diffusion trajectories, the autocorrelation function shows periodicity at 190 nm, and multiples thereof. Figure 6.5c shows the density of localisation events along the x axis, and 6.5d shows the autocorrelation of this density function, for a sample trajectory reflected at actin fences with probability 0.9. There are also low frequency components in the autocorrelation function, which vary from trajectory to trajectory and reflect the random probability of escaping each compartment. The autocorrelation functions of the low and high mobility data subsets also show peaks every 190 nm. To test the validity of the autocorrelation analysis, we performed the same analysis on Brownian trajectories. As expected, the autocorrelation of Brownian trajectories showed no periodicity at multiples of 190 nm (Figure 6.5d).

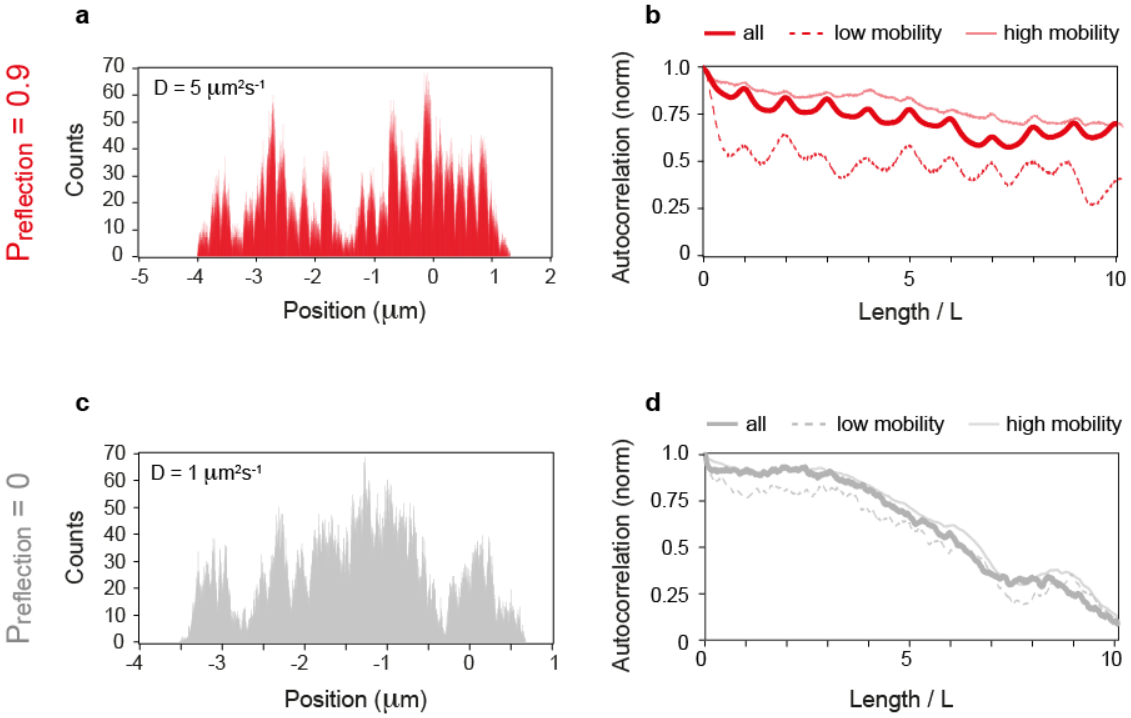


Figure 6.5: a) 1D density of localisation events along the x axis and b) autocorrelation function for a sample simulated trajectory of a probe diffusing with D_{micro}= 5 μm^{2}s^{-1} in a periodic array of semi-permeable barriers with spacing L = 190 nm for $P_{reflection} = 0.9$. c) 1D density of localisation events along the x axis and d) autocorrelation function for a sample simulated trajectory of a probe diffusing with $D_{micro} = 1$ $\mu m^2 s^{-1}$, consistent with the experimentally recorded microscopic diffusion coefficient of AuNP-labelled proteins diffusing in the membrane of neurons. The simulated trajectory length was 100,000 frames, comparable to the length of experimental trajectories. The low and high mobility traces indicate the autocorrelation of low and high mobility data points only, where the data points have been filtered according to the method described in Section 6.4.2 with thresholds <0.6 and >1.4 times the average standard deviation in position over a 5 ms time window.

6.4 Results

6.4.1 High speed tracking with iSCAT

To examine whether the trajectories of membrane proteins are compartmentalised by actin at 190 nm intervals, we recorded movies of the gold-labelled protein constructs with iSCAT at frame rates up to 40 kHz. The L-YFP-GT-mHD 46 transmembrane probe with an extended cytosolic domain (which we denote "trmX" for shorthand) is expected to be most confined, as in addition to interacting with protein pickets, it has an enhanced probability of interacting directly with the actin fences. Figure 6.6b shows an example trajectory of the trmX probe on the distal axon. In addition, this figure shows: c) the position of the protein along the neurite axis as a function of time; d) the density of localisation events along the neurite axis; e) and the autocorrelation of the density function, as well as a) the time-dependent diffusion plot for all trajectories recorded. The trajectory has been aligned so that the neurite axis corresponds to the x dimension.

The diffusive plot (Figure 6.6a), indicates that the trajectories of the trmX protein are confined, with a macroscopic diffusion coefficient approximately 10 times slower than the microscopic value of 1.1 $\mu m^2 s^{-1}$. Neither the xy trajectory nor the plot of x position vs time, however, show evidence of the protein being corralled within 190 nm compartments according to the hop diffusion model. This was unexpected as in previous high speed SPT studies with $\phi = 40$ nm gold labels, hop diffusion from one compartment to the next was identifiable by eye [86, 88, 205, 84]. It is also interesting that, despite not detecting compartmentalisation in the xy trajectory, the autocorrelation of localisation density suggests there is a weak periodicity at approximately 200 nm in this trajectory. We note that the periodicity of the autocorrelation function for most trajectories was less convincing than in this example, hence the evidence for periodicity, in general, is weak.

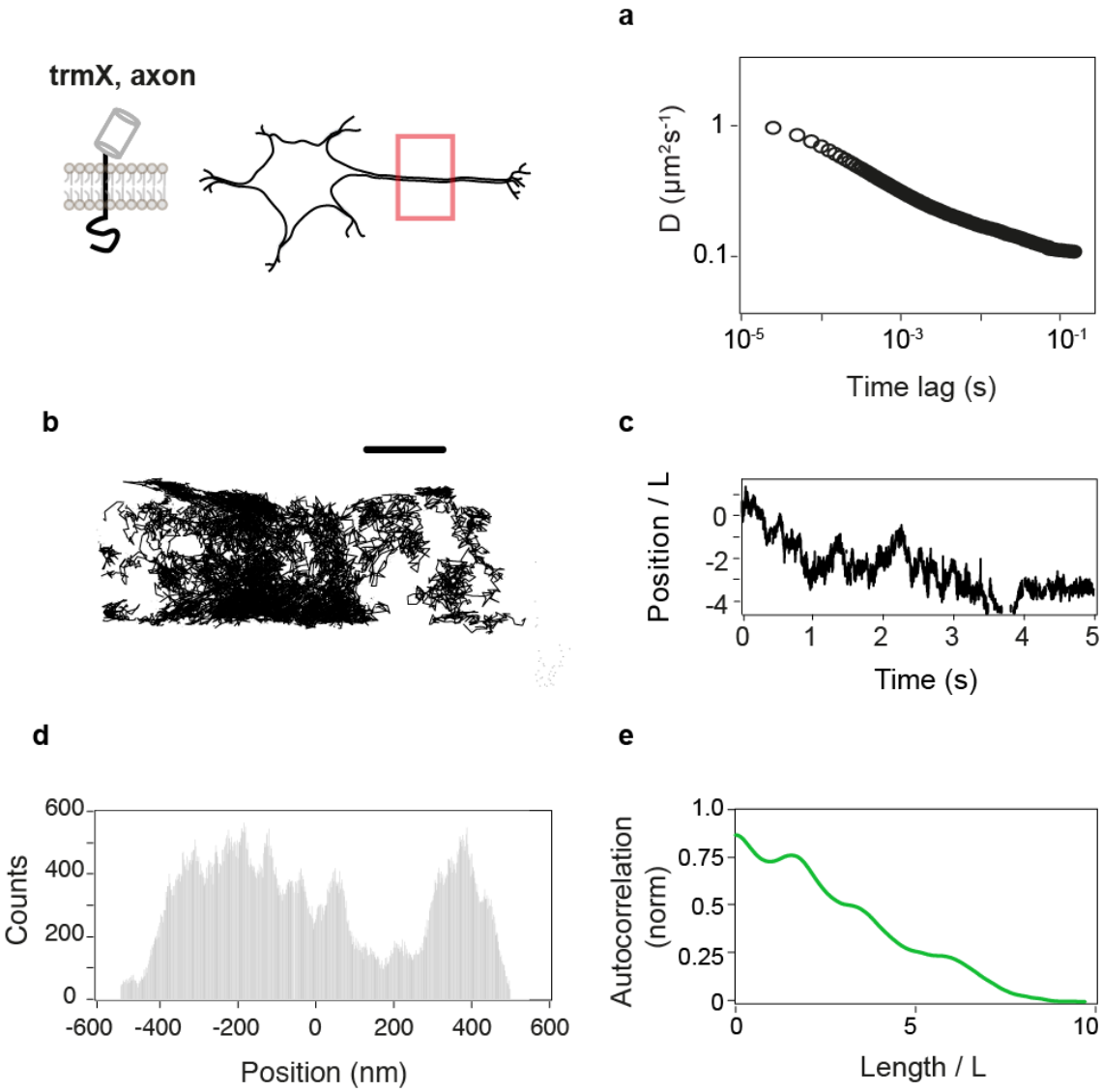


Figure 6.6: Example trajectory of the extended transmembrane probe, aligned such that the x axis coincides with the long axis of the neurite. a) Average diffusion coefficient vs time lag for all recorded trajectories (total 2×10^6 data points) on a log log scale. b) Trajectory of the trmX protein construct, recorded at 40 kHz. For clarity, every 10th frame of the total 1.5×10^5 data points is shown. c) The x coordinate of the trajectory shown, as a function of time. The positions of the actin fences, separated by L = 190 nm, are marked on the vertical axis. Only localisation events with error <6 nm are shown. d) 1D density of localisation events along the x axis and e) autocorrelation function of d).

If the trmX probe is easily able to pass over the actin fences, another mechanism of confinement must be responsible for slower diffusion on macroscopic length and time scales. One possible mechanism, investigated in Chapter 5, is transient binding. We can rule this out, however, as such events would be easily identifiable as flat line segments in the x(t) plot (Figure 6.6c).

An alternate mechanism for slowed diffusion over macroscopic length scales is protein crowding. Proteins that are immobilised by pinning to the actin cytoskeleton act as obstacles that impede the diffusion of mobile molecules by restricting the mean free path. In addition, there is an increase in local viscosity around protein obstacles due to hydrodynamic friction between the fluid membrane and the immobile protein and its associated lipid shell [214, 215]. Given that the cortical actin cytoskeleton binds a large fraction of membrane proteins [200, 99], and that protein pinning density has been correlated with the diffusion of mobile lipids and proteins [90], we would expect regions of slowed diffusion in the vicinity of the actin fences.

6.4.2 Spatial modulation in mobility

To investigate the potential for the actin fences to locally modulate diffusion within the membrane we calculated spatially resolved mobilities based on the range of motion within a 5 ms time window. This time interval was chosen to be several times shorter than the average compartment residence time, which can be estimated from the diffusion log-log plot as the time lag at which the slope becomes essentially flat. A protein observed at time intervals longer than this value will appear to diffuse with Brownian motion, consistent with the observation interval being longer than the compartment residence time. We note that setting the threshold for low and high mobility categories closer to the mean reduces the strength of the pattern, while using a longer time window results in wider stripes and less lone data points. The threshold levels and number of frames were chosen as a compromise to show

the density variations with reasonable signal to noise.

Specifically, we filter the data into low and high mobility localisation events, defined as those data points where the time-local standard deviation in the x coordinate over 200 frames (5 ms) was less than 0.6 × / greater than 1.4 × the average standard deviation for all 200 frame windows. Points with intermediate mobility values are discarded. We confirm that filtering the data into low and high mobility subsets does not produce artefactual periodicity in the autocorrelation function of Brownian trajectories (Figure 6.5).

Figure 6.7 shows low and high mobility localisation events in blue and yellow respectively, for two example trajectories of the trmX probe, located on the distal axon. Here the density of data points in the slow mobility category appears to occur in stripes, whereas the data points in the high mobility category appear evenly distributed along the neurite. To quantify the strength of the periodicity we aligned the stripes to be perpendicular to the axis of the neurite, by applying a linear correction to the coordinate x_i depending on the y coordinate y_i. The new value $x_{i,aligned}$ is given by $\frac{y_i - y_{min}}{(y_{max} - ymin)}\omega$ where ω was determined by eye to best align the stripes. All plots in Figure 6.7 are shown post-alignment.

The autocorrelation of the density per unit length was calculated for the low mobility and high mobility data, as shown in the blue and yellow traces on the right. There is a clear indication of periodicity in the low mobility data, with a spacing of $\sim$ 200 nm between peaks. On the other hand the autocorrelation of the high mobility data does not display any structure. We note that the data shown in part a) is the same trajectory as in Figure 6.6. The autocorrelation function of the low mobility data points indicates a much more pronounced periodicity at 190 nm than the autocorrelation of the entire data set (Figure 6.6e).

In the 12 trajectories recorded of the trmX probe, the strength of the periodicity varied, from clearly discernible peaks at 180 - 200 nm and higher harmonics, to no

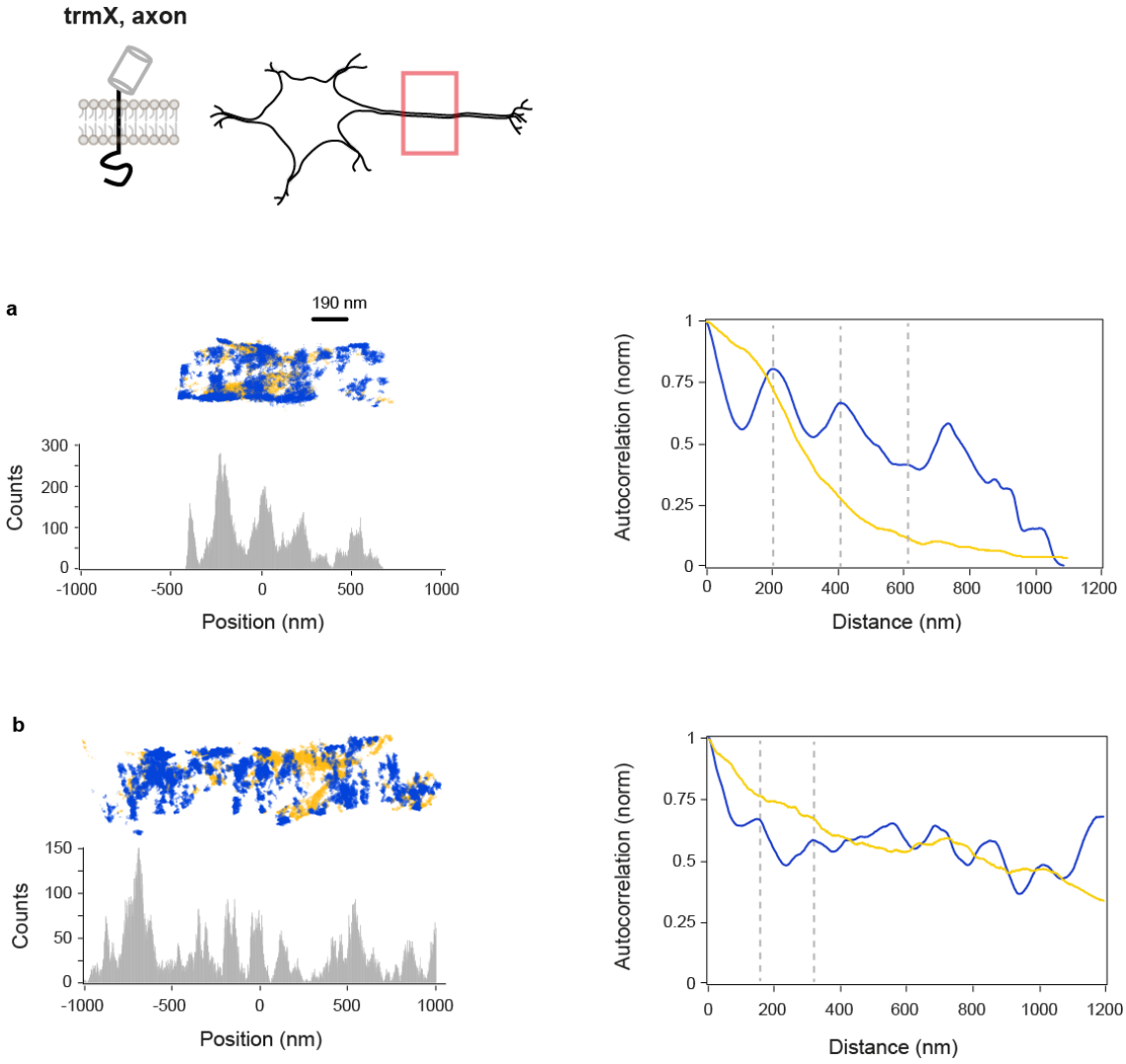


Figure 6.7: Modulation of mobility along the axon for a transmembrane probe with extended cytosolic domain (trmX). Two sample trajectories are shown and analysed as follows: (top left) locations of high and low mobility ($\sigma_{5ms} = 0.6\sigma_{(5ms,avg)}$ and $\sigma_{5ms} = 1.4\sigma_{(5ms,avg)}$ $1.5{\times}10^5$ data points; (bottom left) number of low mobility data points per 1 nm interval in x; (right) autocorrelation of the density of high and low mobility localisation events per nm length along the axon. High mobility data is displayed in yellow, and low mobility data in blue. 10 - 30% of the total number of data points meet the criteria for inclusion in each category, depending on the spread in the standard deviation for the particular trajectory.

detectable peaks in the 180 - 200 nm region. Part of the variation may be explained by curvature of the neurite, possible orientation with a component out of the xy plane. We sometimes observe peaks at separations a few 10s of nanometers shorter or longer than 190 nm, which could occur randomly, but may also be due to the probe interacting with only a subset of the fences.

6.4.3 Effect of cytosolic domain on mobility

To investigate the relative contribution of pickets vs fences, we tracked a modified transmembrane probe with a shorter cytosolic domain, L-YFP-GT-46, which we denote "trm" for shorthand. Given that the distance between the actin cytoskeleton and the membrane is typically a few nanometers, the trm probe is very unlikely to interact with actin directly. The membrane domain and extracellular domain of the trm probe are identical to the trmX probe, so if the diffusion is determined only by obstacles and viscosity of the membrane, then the same diffusion would be expected for the two probes.

Figure 6.8 shows two example trajectories, with mobility analysis and calculation of autocorrelation functions, for the trm probe on the distal axon. Comparing the autocorrelation functions of the trm probe and trmX probe, it is apparent that the periodicity of the trm probe is less well defined. This suggests that direct collision with actin does slow the larger protein. The low mobility data points are sometimes clustered in regions separated by 90 - 100 nm, i.e. two clusters per 180 - 200 nm. This is apparent in the colour-coded xy plot in example b). Perhaps due to the curvature of the neuron, the pattern does not appear in the autocorrelation plot. 90 nm periodicity is also apparent in the autocorrelation of example a). This could indicate regions of slowed mobility on both sides of each actin fence.

We note that there are more localisation events at the top and bottom of the neurite,

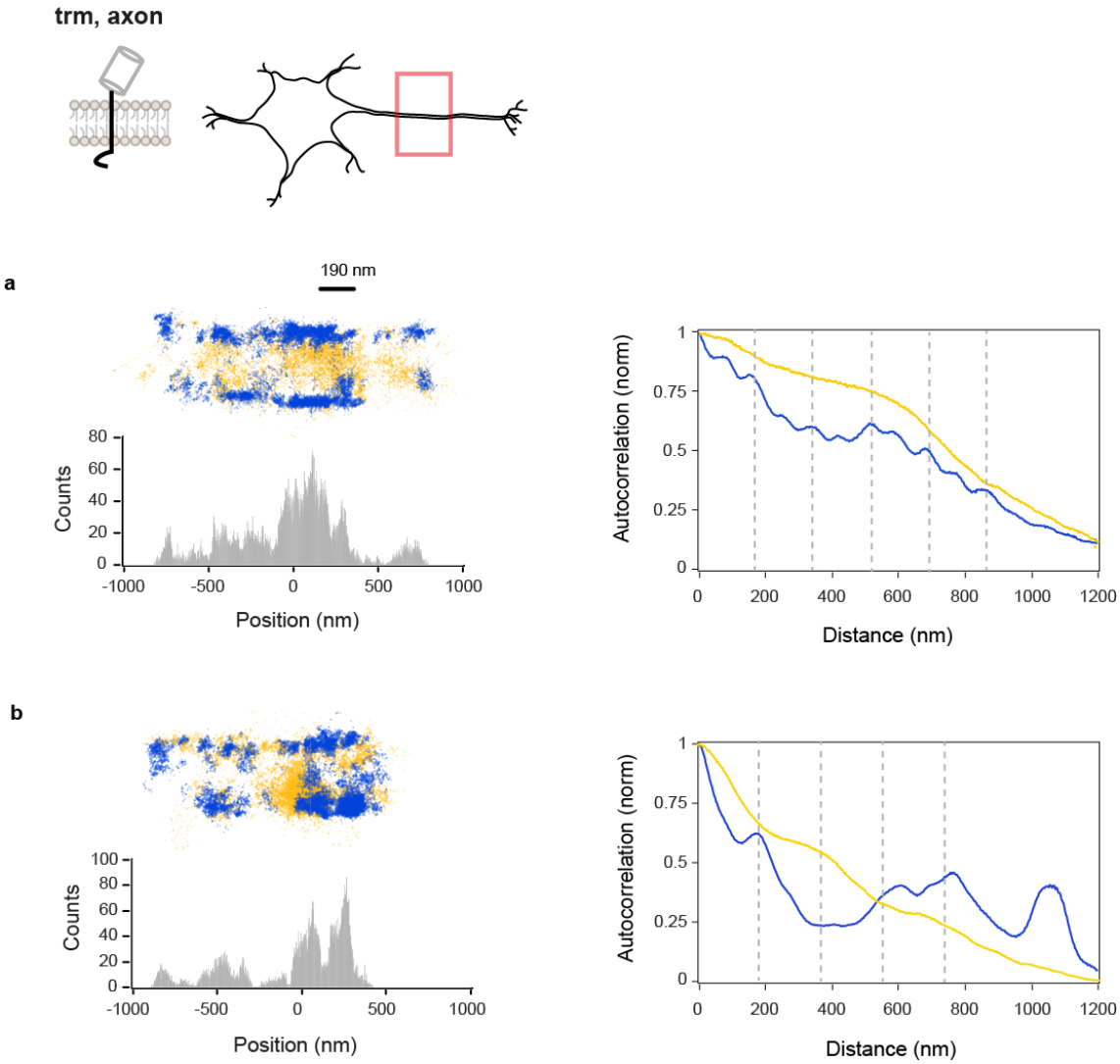


Figure 6.8: Modulation of mobility along the axon for a transmembrane probe with minimal cytosolic domain (trmX). Two sample trajectories are shown, following the same analysis as Figure 6.8. In brief, the figures show from top left in a counter clockwise direction: the slowest (blue) and fastest (yellow) data points; the density ρ_x of the slow data points, integrating across y; autocorrelation of the density functions for slow and fast data.

which is expected given the projection of the axon - the cross section of which is approximately a circle - onto a two dimensional plane. This effect is more visible in the trm dataset, probably because the density of data points is lower due to the probe spending less time in each compartment. Trajectories for the trm probe were also recorded at 20 kHz (vs 40 kHz for the trmX probe) resulting in a lower number of data points per compartment.

6.4.4 Mobility of a GPI anchored protein

The GPI-GFP protein is different in several respects from the transmembrane proteins: it resides only in the outer leaflet; consisting of a lipid anchor, it has a much smaller membrane footprint; it associates with lipid rafts; and it contains long, saturated acyl chains which are capable of interdigitation with cytosolic leaflet lipids. We first examined whether GPI-GFP diffusing on the distal axon

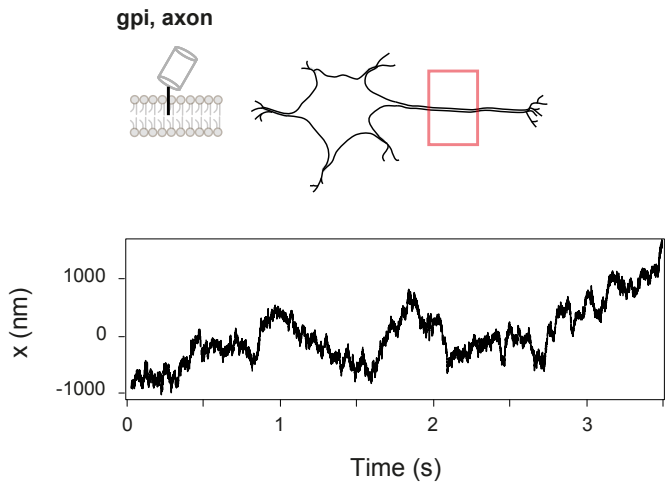


Figure 6.9: An example trajectory of the GPI-GFP protein construct labelled with $\phi = 40$ nm gold. The protein was tracked on an axon. The x coordinate of the trajectory is shown, including all localisation events with error <6 nm. No periods of transient immobilisation are present.

undergoes any periods of transient confinement, such as would be expected from interdigitation of lipid tails. Interestingly, we did not observe confined behaviour in any of the trajectories, one example of which is shown in Figure 6.10).

Figure 6.9 shows the density of localisation events and autocorrelation functions for two example trajectories of the GPI-GFP protein on the distal axon, neither of which indicate any clear evidence of a periodic modulation in mobility.

6.4.5 Comparison of mobility in axons and dendrites

The periodic cytoskeletal structure has been more difficult to detect in dendrites, where it has been observed in only a subset of cells (vs ubiquitous detection in axons) and often in patchy segments. Whether this is due to different binding efficiencies of the fluorescent markers in the axon and dendrite, or to the cytoskeleton being only partially formed in dendrites is not known. We performed tracking on dendrites to investigate any differences in mobility that might indicate weaker compartmentalisation in dendrites.

Figure 6.11 shows an example trajectory of the GPI probe (top) and the trmX probe (bottom) diffusing on a dendrite. As dendrites are much shorter than axons, the surface area of dendrites as a fraction of the total surface area of the cell was lower and consequently the probability of a AuNP binding to a probe located on a dendrite was small. As such we were only able to record a few trajectories which was not sufficient to make statistical claims about the difference in mobility between axons and dendrites.

We did, however, observe periodicity in the mobility, as observed on axons. The modulation in mobility for the GPI probe and the trmX probe on a dendrite is shown in Figure 6.11. The data was recorded at a slower frame rate of 2 kHz, using the scanned wide field channel (described in Section 3.1.3), which allowed for

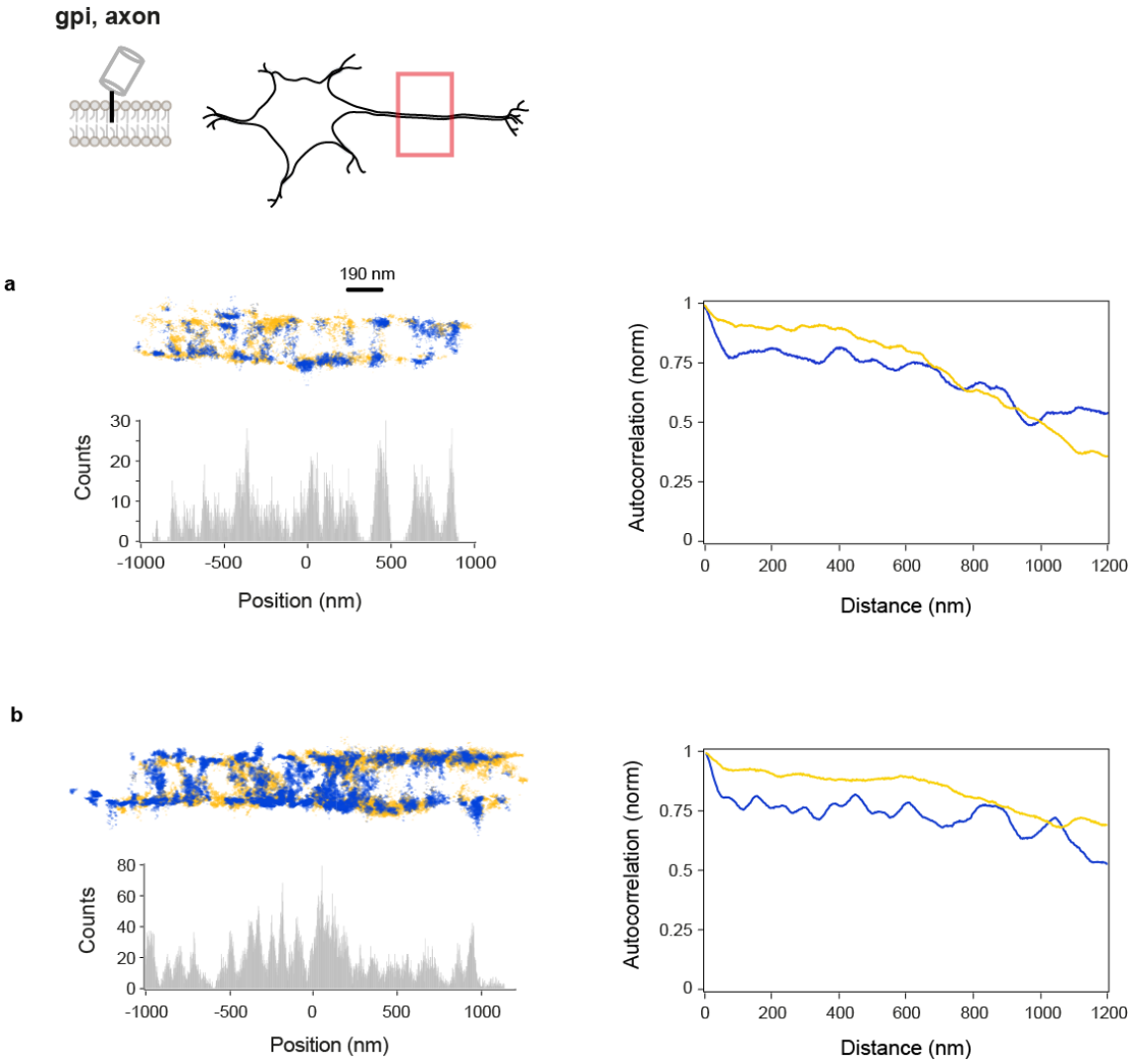


Figure 6.10: Modulation of mobility of GPI-GFP along the axon. Two sample trajectories are shown, following the same analysis as Figure 6.8. In brief, the figures show from top left in a counter clockwise direction: the slowest (blue) and fastest (yellow) data points; the density ρ_x of the slow data points, integrating across y; autocorrelation of the density functions for slow and fast data.

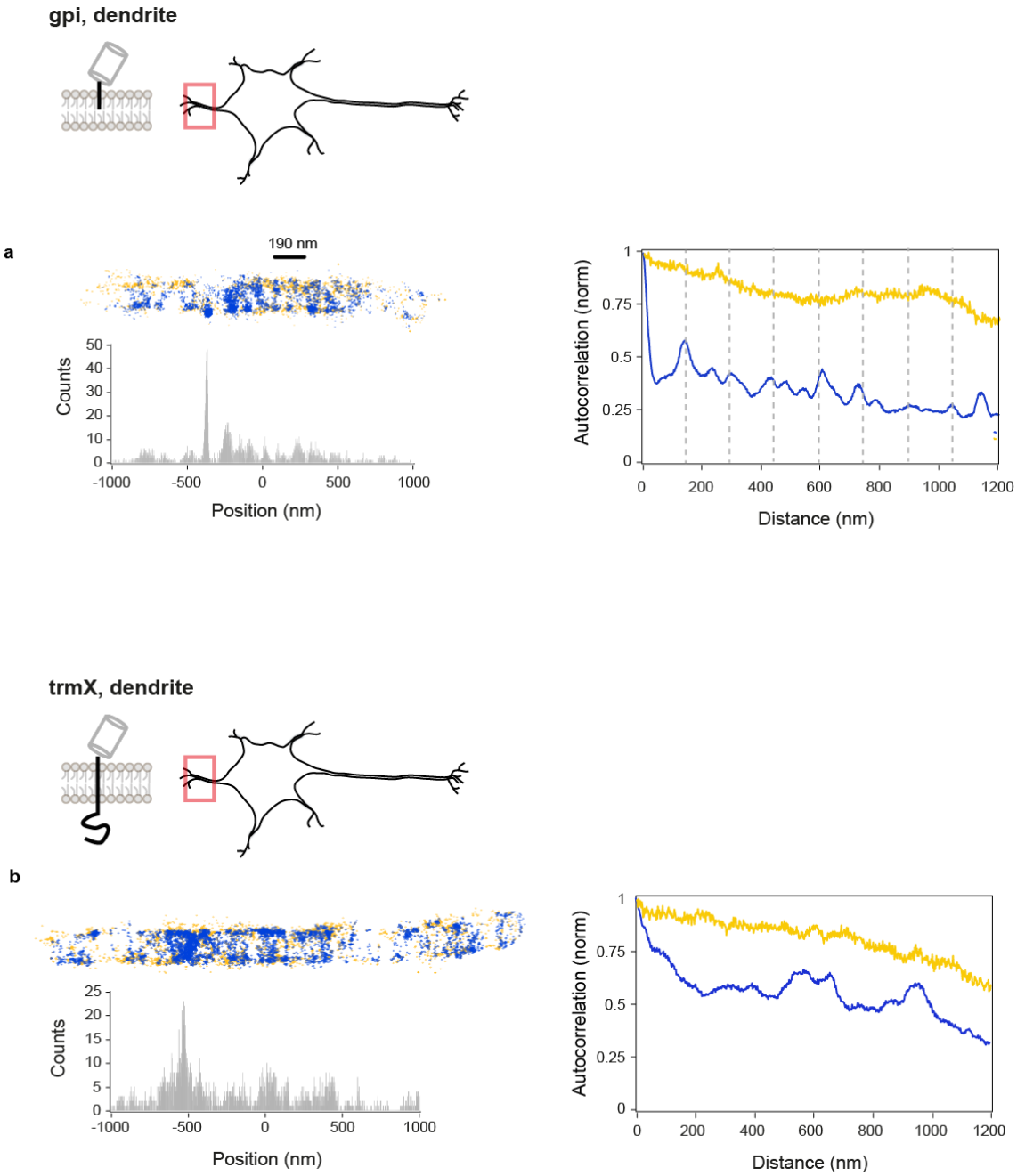


Figure 6.11: Modulation of mobility of the GPI-GFP and trmX probe on dendrites. Two sample trajectories are shown, following the same analysis as Figure 6.8. In brief, the figures show from top left in a counter clockwise direction: the slowest (blue) and fastest (yellow) data points; the density ρ_x of the slow data points, integrating across y; autocorrelation of the density functions for slow and fast data. Top gpi, bottom trmX.

illumination and detection of a larger field-of-view. The length of each trajectory is 10 s. The increased length of the trajectory assists in visually detecting periodicity in the mobility, which is apparent by eye in the relative positions of the blue data points in Figure 6.11a). The autocorrelation sometimes exhibited a series of peaks at 180 - 200 nm (Figure 6.11a, right) and higher harmonics, together with a number of additional peaks. The higher noise levels are likely due to the lower number of data points per unit length, as determined by the frame rate.

6.4.6 Diffusion analysis

The squared displacements for time intervals up to 20% of the length of each trajectory were calculated for all trajectories, for each membrane protein construct. Figure 6.12 shows the average 1D diffusion coefficient ($D = \frac{MSD_x}{2\tau}$) as a function of time lag for the three probes measured. The microscopic diffusion coefficients have values of 1.6 $\mu m^2 s^{-1}$ for the GPI-GFP protein, 1.5 $\mu m^2 s^{-1}$ for the trm protein and 1.0 $\mu m^2 s^{-1}$ for the trmX protein. Most of the change in the diffusion coefficient occurs up to a time lag of a few tens of ms, beyond which point the diffusion continues to decrease slowly, which may be explained by confinement of the probe on length scales of several μm due to cell debris in the sample or other obstacles blocking the diffusion over long distances, which we sometimes observe.

If the assumption that the probes diffuse with a uniform, fast diffusion coefficient within each compartment were true, the diffusion of the microscopic diffusion coefficient of the trmX and trm probe should be the same. However, we observe that the trmX protein construct has a lower diffusion coefficient than the trm protein construct for all time intervals. The GPI-GFP is the least confined at intervals beyond 1 ms, but exhibits diffusion coefficients intermediate between the small and large transmembrane proteins at shorter time lags.

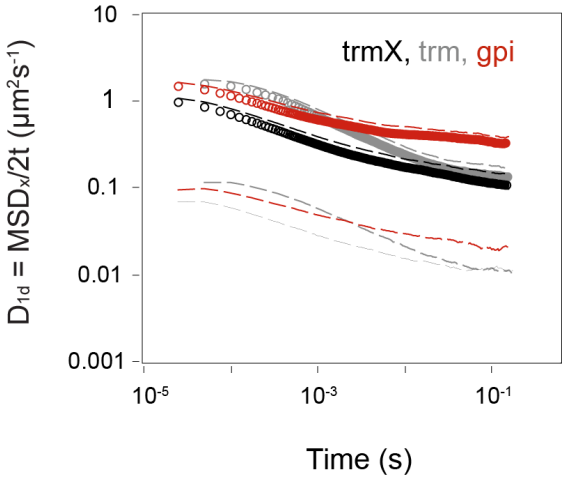


Figure 6.12: Time-dependent diffusion plots for the extended intracellular domain transmembrane protein (black), minimal transmembrane protein (grey) and GPI-GFP protein (red). The total number of data points in trajectories with each probe are: extended transmembrane probe (40 kHz) = 1.1×10^6, minimal transmembrane probe (20 kHz) = 5.2×10^5, and GPI-GFP probe (40 kHz) = 9.9×10^5. The error bars are the 75th and 25th percentile values.

We note that the microscopic diffusion coefficients are approximately 5 times lower than values reported in previous high speed studies examining a range of cell types [86, 88, 205, 84] at the same frame rate of 40 kHz. There have been no high speed studies on neurons, however, with which to directly compare our data. Furthermore, it is possible that the higher microscopic diffusion coefficients in the literature are an artefact of larger localisation uncertainty.

6.4.7 Tracking with fluorescent labels

Tracking was also carried out on fluorescently labelled protein constructs, at slower frame rates of 100 to 300 Hz, using either QDots or AlexaFluor647 as labels. The diameter of the functionalised QDots is approximately 20 nm, while AlexaFluor647 has molecular dimensions with a molecular weight of only 1158 Da. Data was recorded using a field of view of 50 μm, typically containing 10s of labels. Immobile particles were removed from the analysis, and all mobile particles were localised in each frame by fitting a 2D Gaussian function as described in [216].

Figure 6.13 shows an example localisation map of Qdot-labelled GPI-GFP probes on an axon. In this example and several other similarly recorded maps, the data exhibited a clear $\sim$ 180 - 200 nm periodicity which extends for 10s of μm.

The clarity of the pattern showed some dependence on the total number of data points, which varied depending on the achievable labelling density. While such data is not typically used to determine compartmentalisation by actin, the known periodicity of the actin rings in this case has allowed us to detect a correlation between the cytoskeleton and the pattern of localisation events in the membrane.

Interestingly, periodicity was not detectable with the AlexaFluor647-labelled proteins at similar frame rates. While this raises a potential concern that larger labels induce compartmentalisation that is not otherwise present, the lack of periodicity in the fluorescent dye-labelled trajectories could be explained by the fact that these trajectories are much shorter due to photobleaching, and the density of data points is therefore significantly lower. In fact, none of the high speed trajectories acquired with AuNP labels displayed clear periodicity in the localisation data either (for example, Figure 6.6). This is likely because the duration of a single AuNP trajectory is roughly 100 times shorter than the total duration of data contained within a QDot tracking dataset. As the motion of each

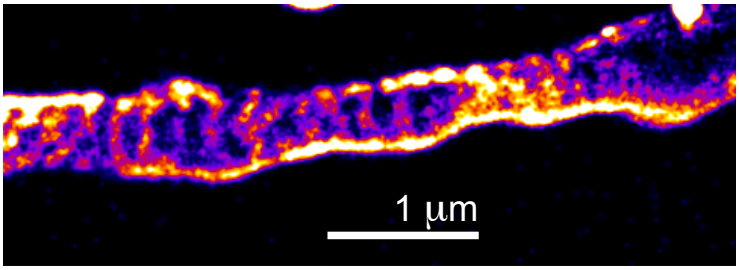


Figure 6.13: Spatial density map constructed from the localisation events of multiple QDot-labelled GPI-GFP probes on the distal axon, tracked at 200 Hz.

protein is random, longer recording times are more likely to show subtle patterns.

To analyse the effect of label size on diffusion, the median diffusion coefficients for the QDots, Atto647N and 40nm AuNP labels were calculated, based on the line of best fit through the median square displacement curve from data points 10 ms to 30 ms, or equivalently, $D_{2,4}$ at a frame time of 5 ms, typically used for fluorescent label tracking.

For QDots and Att647N, very similar median diffusion values were found. All trmX proteins had diffusion coefficients between 0.2 - 0.4 $\mu m^2 s^{-1}$, while the GPI-GFP protein had diffusion coefficients between 0.3 - 0.5 $\mu m^2 s^{-1}$ [211]. The minimal transmembrane probe was not imaged with fluorescent labels. For $\phi = 40$ nm AuNPs, the average diffusion coefficients based on median square displacements are 0.077 $\mu m^2 s^{-1}$ for the trmX probe and 0.128 $\mu m^2 s^{-1}$ for the GPI probe, approximately three times lower than those for the fluorescent labels. We note that part of the difference related to label size may be due to steric exclusion of the AuNP from the surface of the coverslip, which in turn restricts the range of motion of the labelled protein.

It is important to consider the potential effect of time averaging when comparing

trajectories recorded at fast and slow frame rates. For a particle that diffuses freely within a compartment, the average location of the protein over the exposure time approaches the centre of the compartment if the exposure time is less than the residence time in the compartment [87]. What effect this has in the trajectories acquired is difficult to say, as the high speed data suggests that diffusion is not equally rapid throughout the compartment. We note that time averaging the data recorded with AuNP labels should provide a means to test this effect, but as each single particle typically spent no more than 5 s within the imaging field of view, such analysis results in very few data points and we were not able to obtain a definitive answer to this question.

6.5 3D localisation

In addition to examining compartmentalisation of the membrane by the actin rings that make up part of the cytoskeleton, it would also be informative to know whether the membrane is compartmentalised in the orthogonal direction by connecting spectrin tetramers. We attempted to answer this question by modifying the setup for tracking in three dimensions. While several difficulties prevented us from reaching an answer on this particular question, the 3D tracking results are nonetheless informative for understanding the freedom of movement of the AuNP-labelled particle over the cell surface.

To determine the position of the label in x,y and z dimensions, we inserted a cylindrical lens in the fluorescence imaging channel to create a PSF whose FWHM in the x and y dimensions vary astigmatically with the height of fluorescent label above the coverslip. The modification to the TIRF setup and associated calibration of the heigh as a function of FWHM dimensions is described in detail in Section 3.2.2, and is based on the method outlined in [136].

Our aim was to be able to perform tracking simultaneously in the fluorescence and iSCAT channels. While dye-loaded latex beads or silica beads presented an optimum label in terms of providing strong signal in both the iSCAT and fluorescence channels, we found that these particles did not bind to live cells. Assays on fixed cells, on the other hand, showed strong binding, suggesting the beads have an insufficient zeta potential to approach the negatively charged surface of live cells.

Our second approach was to take advantage of the fluorescence properties of gold nanoparticles, which, when excited with blue or green illumination, emit a red-shifted fluorescence spectrum [217]. Using 462 nm illumination and detecting in the range from 505 nm to 605 nm, we were able to record short trajectories of a AuNP-labelled protein on a neuron, with z information accessible from the fwhm of the PSF. The disadvantage of this method is that very high laser powers were required (in excess of 20 $\mathrm{kWcm^{-2}}$), which caused visible cell damage for exposures longer than 1 s.

A third approach is to coat gold nanoparticles with a fluorescent dye. While such fluorescent particles contain significantly fewer fluorescent molecules than a dye-loaded particle, and hence produce a weaker signal that bleaches faster, they are easy to conjugate to gold via a streptavidin coated gold surface, and the gold nanoparticles bind to cells with moderate efficiency. We tested biotin-alexafluor488, biotin-atto465 and biotin-atto488, all of which are strongly excited by the 462 nm laser, and which we can detect in the fluorescence window between 505 and 605 nm. However, we found that no fluorescence was observed from the dye-coated gold particles. While surprising, this may be explained by quenching by gold nanoparticles, whereby resonant energy transfer between the dye and the gold nanoparticle can enhance non-radiative decay [218]. Particularly strong effects have been reported for blue excitable dyes [219]. In addition the high background of GFP or YFP emission, and the relatively lower signal from surface

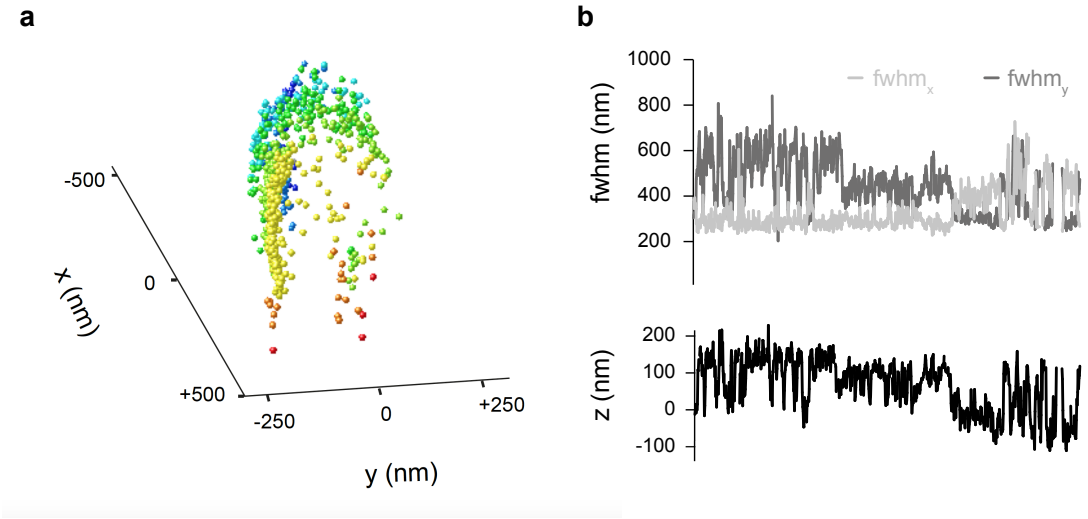


Figure 6.14: a) Example 3D trajectory of a protein on a neurite, determined from fluorescence imaging with astigmatic focusing. b) The FWHM in the x and y dimensions were used to calculate the z coordinate based on the calibration described in Section 3.2.2. The protein (trmX construct) was labelled with a $\phi = 40$ nm AuNP and illuminated with 462 nm illumination, detecting weak fluorescence from the gold nanoparticle in the range from 505 nm to 605 nm. For clarity, each localisation event in a) has been coloured on a scale from red to blue according to the x coordinate.

coating compared to loading the interior volume with dye, may also have contributed to the problem. The particle could also not be coated completely as some streptavidin sites were also needed for antibody attachment.

6.5.1 3D reconstruction from circular geometry

Though it was difficult to simultaneously optimise the scattering and fluorescence signal for 3D tracking, as described above, the trajectories we were able to record indicated that the particle moves around the top of the circumference of the neurite, but does not pass along the surface close to the glass coverslip. This fact, together with an assumption that the neurite is approximately cylindrical, allows

us to determine the z coordinate from the radius and the y coordinate. We can assume a 1:1 correspondence between the z and y positions, which allows for the determination of z based on the simple geometry of a circle (Equation 6.1).

$$z = \sqrt{r^2 - (y - y_0)^2} \tag{6.1}$$

where r is the radius of the neurite, y is the measured y coordinate, and y_0 is the the coordinate at the centre of the neurite axis.

Figure 6.15 shows an example 3D mapping of a trajectory. The iSCAT contrast, which varies smoothly as function of z, provides a further verification that the neuron does indeed have a circular geometry. The trajectory is colour coded by the contrast measured in iSCAT, showing smooth variation in contrast, which is symmetric about the y axis as expected for a circle.

6.5.2 Angular distribution of localisation events

A more convenient way to visualise the trajectory is to display the data in terms of only x and an angle, θ, which can again be derived from circular geometry. With this approach, the angular position appears to be randomly distributed around the neurite. It is important to note that 3D tracking on neurons with small diameters (less than $\sim$ 250 nm) is simple, as the particle contrast does not undergo closely spaced inversions in contrast with z. Most neurons have a larger radius than this, and as such there is at least one height at which contrasts inverts through zero, and the position of the particle cannot be determined. While a radial fitting approach could potentially locate the particle from the (non-zero) contrast of the PSF rings, we find that in the vicinity of the contrast inversion the SNR is too low for this method to be accurate. Large neurites therefore have stripes at certain latitudes where the particle cannot be localised.

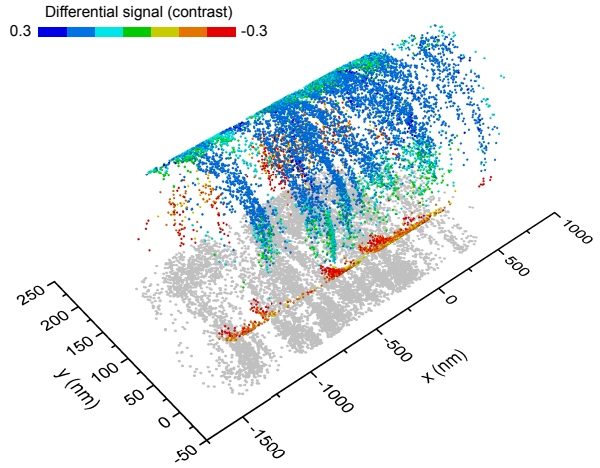


Figure 6.15: A 3D representation of the first trajectory shown in 6.11. The z coordinate has been calculated from the y coordinate and the neurite radius, determined as $(y_{max} - y_{min})/2$. For clarity, each localisation event has been coloured according to the iSCAT contrast.

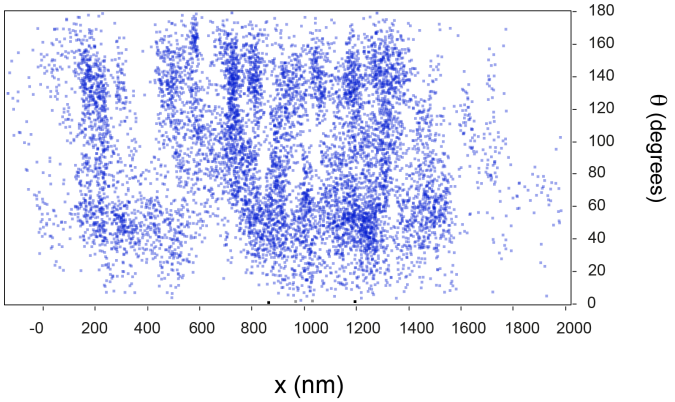


Figure 6.16: A phase representation of the first trajectory shown in Figure 6.11. The angle θ has been calculated from the y coordinate and the neurite radius.

6.6 Discussion

6.6.1 The cytoskeleton as a traffic jam, not a road block

All protein constructs undergo relatively fast microscopic diffusion ($\sim 1\ \mu m^2 s^{-1}$) and macroscopic diffusion coefficients five to ten times slower at time lags >10 ms. We expected to observe trajectories that reflected off actin fences spaced ~190 nm apart, but instead saw no clear evidence of this behaviour. There is, however, some evidence for periodic modulation in mobility, particularly for the extended transmembrane probe. While this finding has not been previously reported in high speed tracking studies, it is consistent with the behaviour that would be expected in regions of high protein density. Both circumferential friction around immobile obstacles [215], and percolation through dense arrays would give rise to slower diffusion [100, 220]. Lower diffusion coefficients observed at higher protein densities may explain, at least in part, the discrepancy between diffusion coefficients measured in reconstituted lipid membranes compared to native membranes of live cells [54, 63, 221]. In effect, the actin cytoskeleton appears to create a "traffic jam" of proteins, slowed by the locally high density of immobile obstacles, but does not act as a road block to diffusion.

6.6.2 Why is hopping not observed?

High speed SPT studies of membrane proteins in a range of cell types have reported facile identification of hop diffusion by eye [86, 222, 88, 205, 84]. In general, a frame rate of 40 kHz was found to be fast enough to detect confinements as short as 1 ms, or equivalently 40 frames residence time within a single corral. In our hands, however, hop diffusion is not apparent in any high speed trajectories.

To address possible explanations for the lack of hop diffusion in the present work, it is important to note that diffusion in neurons has not previously been studied at

high speeds. It is possible that the actin network has a lower effect on membrane protein mobility in neurons, than other cell types. Or, the difference could be due to a technical artefact associated with the experimental method.

One possible explanation why hopping was observed readily in previous studies but not in this work is a difference in the degree of cross-linking i.e. binding of the AuNP label to more than one membrane lipid or protein. The effect of cross-linking has been established by experiments in which membrane lipids were deliberately cross-linked, resulting in a greatly increased residence time inside actin-bounded compartments [88]. Intuitively, we expect that the convex curvature of the neuron reduces the chance of cross-linking in the current assay, therefore a difference in crosslinking may be a factor.

To test this hypothesis, we compare the macroscopic diffusion coefficients in this work and previous work. If cross-linking is greater, the macroscopic diffusion coefficient should be comparatively lower. Values reported in the literature for cell types with similar reported mesh sizes were examined. For example diffusion of the transferrin receptor (a transmembrane protein) in NRK cells with a mesh size of 230 - 260 nm was reported to have $D_{50ms} = 0.31\ \mu\text{m}^2\text{s}^{-1}$ [86]. In the current results, we observe $D_{50ms} = 0.17\ \mu\text{m}^2\text{s}^{-1}$ for the trm probe. The values we report are the 1D diffusion coefficients along the neurite axis. We have not included the y coordinate in our analysis due to the limited length of the neurons (approximately 400 nm) in the y dimension, and the curvature of the membrane, both of which produce apparent reduced diffusion values in this dimension. We also note that our experiments are susceptible to steric exclusion of the AuNP near the coverslip, which may contribute towards slower diffusion values on neurons compared to cell types where the outer membrane does not come into contact with the coverslip. Within the natural variation of diffusion coefficients between different cell types, there is no strong evidence to suggest that cross linking is higher in literature

studies than in the current work.

Another possibility is that molecular pinning, combined with higher localisation errors of dark field SPT (σ = 16 - 20 nm) gives the appearance of compartmentalisation. We do not observe molecular pinning events in the trajectories we have recorded on neurons, however there is evidence that this mechanism of confinement does occur in other cell types [17].

It is also interesting to note that some high speed SPT studies have reported small compartments nested within larger compartments, based on fitting the time-dependent diffusion plot to several regimes of Brownian diffusion [86]. We speculate on an alternate theory, wherein the small compartments represent the size of the slow mobility zone, and the large compartments represent average spacing between actin fences. This theory could be verified by performing iSCAT tracking and subsequent mobility analysis on the cell types thought to exhibit double compartmentalisation, including NRK cells which exhibit apparent 230 nm compartments nested within 750 nm compartments when studied with dark field SPT.

6.6.3 Could periodic mobility arise from steric interactions of the label?

It is clear from a comparison of the macroscopic diffusion coefficients measured with $\phi = 40$ nm AuNPs, QDots and fluorescent dyes, that the larger gold nanoparticles have some slowing effect compared to the smaller labels. Whether this effect is amplified at the actin fences, and hence causes or amplifies the spatial periodicity in mobility, is an important question to address.

Some label-size dependent slowing with uniform effect along the length of the neurite, is expected, for example due to increased drag of the $\phi = 40$ nm AuNP through

the extracellular medium, and hindered motion near the glass surface. However, there are also mechanisms by which the label size could have a non-uniform effect throughout the compartment. In particular, increased protein density near actin fences could lead to a greater probability of steric interactions with the gold label. Furthermore, if a gold nanoparticle is crosslinked to more than one protein in the membrane, the probability of finding a path between protein obstacles decreases dramatically.

It is difficult to compare mobility data with gold labels and QDots, as the time scale 5 ms over which differences in mobility are apparent is equal to the frame time of the QDots data. Whether the increased size of the label does amplify the slowing effect specifically at the actin fences could be investigated in future by studies with gold nanoparticles of different sizes. Another approach would be to carry out a titration in antibody labelling density. In the current work we conjugated AuNPs with an average of two antibodies per particle with the aim of minimising cross-linking, however we cannot rule out the potential contribution to steric slowing.

6.6.4 Are GPI anchored proteins confined with rafts?

The mobility of GPI anchored proteins may be modified by a number of potential interactions, for example the formation of transient homo-dimers [223], the incorporation into lipid rafts [72, 173], or leaflet interdigitation [207, 64, 71, 224]. As such, the GPI anchored proteins might be expected to undergo various modes of motion in addition to compartmentalisation or slowing imparted by the actin fences.

The GPI-GFP protein construct used in this assay has been shown to exhibit clustering within domains based on concentration-independent FRET results [72]. As clustering is interpreted as evidence for raft association, we would expect the

GPI-anchored probe to experience additional confinement within raft domains.

GPI-anchored proteins have also been observed to undergo transient trapping in cells for time scales of ms [207, 64, 71, 224] and within areas estimated as no greater than 120 nm. Where the area could be determined with higher spatial resolution using STED-FCS, trapping was confirmed to be within regions <20 nm [64] diameter. A recent study shows that trapping is mediated by interdigitation of long, saturated lipid tails with immobilised phosphatidylserine lipids, bound via adapter proteins to cortical actin filaments on the cytoplasmic surface [224]. Whether this occurs in neurons, where the cortical actin filaments are incorporated into the stable cytoskeletal structure, is unknown.

Data was examined for transient trapping events consistent with interdigitation-mediated immobilisation as described in the literature, but there was no indication of any such behaviour. This leaves two possibilities - that the GPI-anchored protein associates only weakly with immobile raft domains nucleated by the actin fences, or that the raft domains with which it associates are mobile. Unfortunately the first case cannot be distinguished from the motion expected for interaction with protein pickets. Indeed we do observe a modulation in the mobility of the GPI-anchored protein which sometimes exhibits the same spatial frequency as the actin fences (such as the sample data shown in Figure 6.9 a), but this modulation is observed to a stronger extent in the transmembrane proteins, suggesting that the raft interactions, if they exist, are weak.

If rafts are mobile, they would be very difficult to detect, which is consistent with previous high speed tracking results which report the same average compartment sizes for GPI and transmembrane proteins [84]. In this work, we find that the GPI-anchored protein diffuses faster than both of the transmembrane proteins on all time scales. The microscopic diffusion coefficient is faster than the extended transmembrane protein by a factor of 1.5, and the macroscopic diffusion coefficient

is faster by a factor of 3. There is no consensus in the literature regarding the relative diffusion coefficient of transmembrane proteins and their equivalent GPI anchored forms, suggesting that the ratio may vary from protein to protein depending on the relative magnitude of GPI-AP raft interactions compared to the transmembrane protein actin interactions [203, 204, 84, 225]. The greater level of noise in the spatial autocorrelation of GPI-GFP mobility may also be explained in part by the propensity of GPI-GFP to form transient dimers, with concomitant change in diffusion coefficient.

6.7 Summary and outlook

To date, the models for membrane compartmentalisation by actin have been built upon single molecule trajectories lacking information on the spatial arrangement of the underlying actin filaments, and studies of the effect of average actin density on diffusion. For the first time, we have investigated the mobility of single proteins in cells where the size, shape and relative location of actin compartments is known, allowing us to correlate subtle changes in mobility to the location of actin filaments in the underlying cytoskeletal network.

Our results support the view that actin plays a weak role in controlling membrane diffusion, possibly via protein crowding effects, but does not act as a reflective barrier according to the picket fence model. Our interpretation is consistent with a number of studies demonstrating the importance of protein density on diffusion.

Future super-resolution studies will be vital in confirming the phase of the actin rings relative to the regions of slow mobility. We expect the slow mobility regions to be in phase with actin, consistent with slowing of mobility due to the presence of protein pickets and the associated increase in viscosity and lipid packing density.

6.8 Contributions

This study was part of a larger collaborative project with Helge Ewers' group at Kings College London (KCL). The work presented here was carried out by myself and David Albrecht, with contributions as follows: The primary hippocampal neurons were prepared by David Albrecht at KCL, including the expression of synthetic protein constructs. Super-resolution images of the actin-spectrin cytoskeleton (an example of which is shown in Figure 6.1) were also recorded at KCL, as well as tracking experiments with QDot labels (Figure 6.13). All other data shown in this Chapter was recorded in Oxford and analysed by myself. Specifically, this included construction of the iSCAT microscope, acquisition and fitting of data, and authorship of the analysis software to link trajectories based on fitting errors, perform spatial analysis of particle mobilities, and calculate distributions of diffusion coefficients.

Chapter 7

Conclusion and Outlook

Studying the organisation of the plasma membrane has proven to be an immensely challenging task, due to the experimental difficulty in imaging the motion of single molecules and nanoscopic assemblies on small length scales and fast time scales, and to the complexity of unravelling the interplay of a vast number of competing interactions.

In this work, we have used interferometric scattering microscopy (iSCAT) to break through two important technical barriers that have limited experimental studies to date. Firstly, we have demonstrated the possibility of directly visualising small, dynamic structures in bilayer membranes without the use of labels. Secondly, we have demonstrated single particle tracking at high speeds (50 kHz) with accuracies down to 1 nm, more than an order of magnitude smaller than the accuracy typically achieved in other state of the art methods. This brings us very close to the length and time scales necessary to localise a single molecule diffusing in the membrane with error comparable to the molecular diameter.

The ability to visualise membrane dynamics at this level of detail has brought to light several interesting findings regarding the control of membrane processes in cells. In particular, one goal that has been elusive for several decades is the observation of

dynamic lipid assemblies, known in a cellular context as "lipid rafts". Nanoscopic objects on this length scale, between single molecules and the diffraction limit, are difficult to study by other microscopy techniques. In Chapter 4 we exploited the sensitivity of iSCAT to small differences in refractive index in order observe lipid domains dynamically, non-invasively and without any labels. We provided the first evidence that domains can exist in an equilibrium state with a distribution of nanoscopic sizes, and that single domains dynamically grow, merge, divide and dissolve. Furthermore the nanodomain lifetimes we have measured are comparable ($\sim$ 200 ms) to the reported time scales of signalling processes, supporting the view that lipid nanodomains could indeed control the assembly of signalling complexes. Our methodology offers many possibilities for further investigating the dynamics of lipid nanodomains, such as studying the effect of lipid composition on domain properties, or the effects of mobile and anchored proteins on domain formation. Furthermore, the technique can easily be combined with single molecule tracking, for example to study how lipid phase separation affects the assembly of dimers and signalling complexes.

In Chapter 5 we have characterised the mobility of lipids in model bilayer membranes, to investigate the cause(s) of anomalous diffusion. Our observation of transient confinement of GM1 lipids even in simple model membranes indicates interleaflet lipid-lipid interactions control the motion of GM1 molecules, and that this occurs without the need for transmembrane components. The mechanism we outline in this work, of outerleaflet lipids becoming trapped by interaction with immobilised lipids in the opposing leaflet, via interdigitation of long, saturated lipid tails, is consistent with recent findings in cell membranes. While GM1 is not present in the inner leaflet in cell membranes, phosphatidyl serine lipids have been shown to play the same role, being immobilised by actin binding, and interdigitating with outerleaflet GPI anchored proteins. Future studies in model and cell membranes would be vital in providing quantitative details about the

number of immobilized lipids required for trapping, and how interdigitation sites are related to lipid rafts and the location of actin filaments. High speed tracking of single molecules could also be combined with label free imaging, to determine how diffusion of raft lipids and proteins changes depending on the local phase of the membrane in lipid bilayer models.

In Chapter 6 we have directly investigated the influence of actin on the dynamics of single molecules diffusing in the membrane of hippocampal neurons. We observed a modulation in mobility that correlates with the highly regular spacing of actin rings in the sub-membrane cytoskeleton. Interestingly, the high speed trajectories recorded with 40 nm gold nanoparticle labels do not show evidence of hop diffusion, but suggest that protein crowding may play be the major cause of the difference in diffusion on fast and slow time scales. In particular, we observe some evidence for regions of slowed mobility that corresponds with the spacing of actin fences, consistent with the greater density of proteins expected to occur at the actin fences. This finding unites observations of the dependence of measured diffusion coefficients on the presence of actin, as well as the many reports of a dependence on the density of membrane proteins.

Only a handful of high speed tracking experiments using iSCAT have been carried out to date and our results on neurons are the first use of iSCAT in cell membranes. It would be valuable to examine mobility in other cell types, and to compare the mobilities of a range of lipids and proteins. Label-free iSCAT also presents many possibilities for the detection of single biomolecules, and for directly observing assembly processes in biological contexts as well as for chemistry and materials science applications.

What is stopping us from reaching spatial dimensions for single molecules, unlimited temporal resolution, the sensitivity to detect smaller lipid domains, and to do so in cells? The spatiotemporal resolution is a simple consequence of the SNR of the

experiment where the signal is related to the size of the scattering label, and the noise - in a shot noise limited experiment - can be decreased by collecting more photons. It is clearly undesirable to use larger labels, leaving the reduction of noise as the remaining option. Using detectors with higher pixel fill factors, and near-optimal quantum efficiency, could increase the detection efficiency from the current 10% much closer to 100%. Such detectors are currently available, though are typically much more expensive, and generally cannot operate at very fast frame rates. On the other hand it is possible, at the expense of SNR, to image at higher speeds with specialised cameras.

The sensitivity can similarly be increased by collecting more photons, but in many cases the signal is not shot-noise limited, but rather the lower noise limit is determined by internal motion of the sample. This is almost always the case in cells, and is also the limitation in the studies in droplet bilayers presented in Chapter 4, where we have been limited in detection sensitivity to domains with radius of 50 nm. Ideally an assay is required with no mobile scattering components. While such model membrane assays exist, this is not a feasible solution when the aim is to image small scatterers in cells. In particular, the mobile components of any cell would likely overshadow the contrast due to membrane phases, and therefore lipid rafts are unlikely to be detectable using label-free method in cells. Finding a solution to the problem of competing background scatter would be extremely valuable. Several potential approaches are worth investigating, for example, precise z sectioning could potentially eliminate scatter from planes above and below the membrane. Alternately, low-coherence light sources offer a possible means to exclusively image structures close to the glass-water interface.

Discussion of high speed tracking is not complete without mention of the potential artefacts of large labels. While we have characterised the artefacts due to label interactions in simple, all-lipid model membranes in Chapter 5 and determined that

the label does not cause anomalous diffusion, we do not know whether this is the case in the more complex environment in cells. Ideally it would be desirable to perform tracking with a range of label sizes to investigate whether patterns in mobility, such as the periodic slowing we observe in neurons, are induced or enhanced by the label. One promising approach to tracking with smaller particles is to use a label which generates a signal in both the fluorescence and scattering channels and to localise the particle by correlating the signal in both channels. A range of possibilities for discriminating the label based on its interaction with light could also be explored, including steady state or time-resolved methods.

In summary, interferometric scattering microscopy has revealed previously inaccessible details of membrane dynamics and offers vast potential for a number of future experiments. The facile combination with fluorescence makes it possible to combine label-free imaging with specificity of fluorescence labelling, or to extend the capabilities of high speed tracking in scattering environments. Studies in model membranes and in cells will continue to provide complementary approaches to exploring the many complex questions presented by the cell membrane.

Bibliography

[1] S J Singer and G L Nicolson. The fluid mosaic model of the structure of cell membranes. *Science*, 175(4023):720–31, 1972.

[2] L D Frye and M Edidin. The Rapid Intermixing of Cell Surface Antigens After Formation of Mouse-Human Heterokaryons. *J Cell Sci*, 7:319–335, 1970.

[3] Y Lange, M H Swaisgood, B V Ramos, and T L Steck. Plasma membranes contain half the phospholipid and 90 percent of the cholesterol and sphingomyelin in cultured human fibroblasts. *J Biol Chem*, 265(7):3786–93, 1989.

[4] G van Meer. Lipid traffic in animal cells. *Annu Rev Cell Biol*, 5:247–75, 1989.

[5] K Simons and G van Meer. Lipid sorting in epithelial cells. *Biochem*, 27(17):6197–6202, 1988.

[6] I Pascher. Molecular arrangements in sphingolipids. Conformation and hydrogen bonding of ceramide and their implication on membrane stability and permeability. *Biochim Biophys Acta*, 455:433–51, 1976.

[7] J C Holthuis, T Pomorski, R J Raggers, H Sprong, and G V van Meer. The organizing potential of sphingolipids in intracellular membrane transport. *Physiol Rev*, 81:1689–723, 2001.

[8] W Curatolo. The physical properties of glycolipids. *Biochim Biophys Acta*, 906:111–136, 1987.

[9] R Koynova and M Caffrey. Phases and phase transitions of the sphingolipids. *Biochim Biophys Acta*, 1255:213–236, 1995.

[10] C A Lingwood. Glycosphingolipid Functions. *Cold Spring Harb Perspect Biol*, 3:a004788, 2011.

[11] G van Meer, D R Voelker, and G W Feigenson. Membrane lipids: where they are and how they behave. *Nat Rev Mol Cell Biol*, 9(2):112–124, 2008.

[12] T Blom, P Somerharju, and E Ikonen. Synthesis and biosynthetic trafficking of membrane lipids. *Cold Spring Harb Perspect Biol*, 3:a004713, 2011.

[13] K Simons and E Ikonen. Functional rafts in cell membranes. *Nature*, 387(6633):569–572, 1997.

[14] O A Weisz and E Rodriguez-Boulan. Apical trafficking in epithelial cells: signals, clusters and motors. *J Cell Sci*, 122:4253–4266, 2009.

[15] R Phillips, T Ursell, P Wiggins, and P Sens. Emerging roles for lipids in shaping membrane-protein function. *Nature*, 459(7245):379–385, 2009.

[16] R Schroeder, E London, and D Brown. Interactions between saturated acyl chains confer detergent resistance on lipids and glycosylphosphatidylinositol (GPI)-anchored proteins: GPI-anchored proteins in liposomes and cells show similar behavior. *Proc Natl Acad Sci USA*, 91(25):12130–12134, 1994.

[17] R Raghupathy, A A Anilkumar, A Polley, P P Singh, M Yadav, C Johnson, S Suryawanshi, V Saikam, S D Sawant, A Panda, Guo Z, R A Vishwakarma, M Rao, and S Mayor. Transbilayer lipid interactions mediate nanoclustering of lipid-anchored proteins. *Cell*, 23(161):581–594, 2015.

[18] M S Bretscher. Membrane structure: some general principles. *Science*, 181:622–9, 1973.

[19] K Balasubramanian and A J Schroit. Aminophospholipid asymmetry: A matter of life and death. *Annu Rev Physiol*, 65:71–34, 2003.

[20] M Sheetz. Cell control by membrane-cytoskeleton adhesion. *Nat Rev Mol Cell Bio*, 2:392–396, 2001.

[21] K Gowrishankar, S Ghosh, S Saha, S Mayor, and M Rao. Active remodeling of cortical actin regulates spatiotemporal organization of cell surface molecule. *Cell*, 149:1353–1367, 2012.

[22] M Bezanilla, A S Gladfelter, D R Kovar, and W Lee. Cytoskeletal dynamics: A view from the membrane. *J Cell Biol*, 209(3):329–337, 2015.

[23] E H Egelman, N Francis, and D J DeRosier. F-actin is a helix with a random variable twist. *Nature*, 298:131–135, 1982.

[24] D Bray and J G White. Cortical flow in animal cells. *Science*, 239:883–888, 1988.

[25] N Terada, Y Fujii, and S Ohno. Three-dimensional ultrastructure of in situ membrane skeletons in human erythrocytes by quick-freezing and deep-etching method. *Histol Histopathol*, 11:787–800, 1996.

[26] K Xu, G Zhong, and X Zhuang. Actin, spectrin and associated proteins form a periodic cytoskeletal structure in axons. *Science*, 339(6118):452–456, 2013.

[27] E D'Este, D Kamin, F Göttfert, A El-Hady, and S W Hell. STED Nanoscopy Reveals the Ubiquity of Subcortical Cytoskeleton Periodicity in Living Neurons. *Cell Reports*, 10(8):1246–1251, 2015.

[28] N Morone. Three-dimensional reconstruction of the membrane skeleton at the plasma membrane interface by electron tomography. *J Cell Biol*, 174(6):851–862, 2006.

[29] E J Luna and A L Hitt. Cytoskeleton-plasma membrane interactions. *Science*, 258:955–964, 1992.

[30] G T Charras, C K Hu, M Coughlin, and T J Mitchison. Reassembly of contractile actin cortex in cell blebs. *J Cell Biol*, 175:477–490, 2006.

[31] K Kawai, M Fujita, and M Nakao. Lipid components of two different regions of an intestinal epithelial cell membrane of mouse. *Biochim Biophys Acta*, 369:222233, 1974.

[32] D A Brown and K J Rose. Sorting of GPI-anchored proteins to glycolipid-enriched membrane subdomains during transport to the apical cell surface. *Cell*, 568(3):533–44, 1992.

[33] K A Melkonian, T Chu, L B Tortorella, and D A Brown. Characterization of proteins in detergent-resistant 20. membrane complexes from Madin Darby canine kidney epithelial cells. *Biochemistry*, 16:161–170, 1995.

[34] M Peirce and H Metzger. Hotspots of GPI-anchored proteins and integrin nanoclusters function as nucleation sites for cell adhesion. *J Cell Biol*, 275:976–982, 2000.

[35] T V Kurzchalia, E Hartmann, and P Dupree. Guilt by insolubility: does a proteins detergent insolubility reflect a caveolar location? *Trends Cell Biol*, 5:187 189, 1995.

[36] E London and Brown DA. Insolubility of lipids in Triton X-100: physical origin and relationship to sphingolipid/cholesterol membrane domains (rafts). *Biochem Biophys Acta*, 1508:182–195, 2000.

[37] X M Li, J M Smaby, M M Momsen, H L Brockman, and R E Brown. Sphingomyelin interfacial behavior: the impact of changing acyl chain composition. *Biophys J*, 78:1921–1931, 2000.

[38] H Heerklotz. Triton promotes domain formation in lipid raft mixtures. *Biophys J*, 83(5):2693–2701, 2002.

[39] K Simons and M J Gerl. Revitalizing membrane rafts: new tools and insights. *Nat Rev Mol Cell Biol*, 11:688–699, 2010.

[40] C Dietrich, L A Bagatolli, Z N Volovyk, M Levi, N L Thompson, E Gratton, and K Jacobson. Lipid rafts reconstituted in model membranes. *Mol Biol Cell*, 11:316A–316A, 2000.

[41] K Simons and W L C Vaz. Model Systems, Lipid Rafts, and Cell Membranes. *Annu Rev Biophys Biomol Struct*, 33(1):269–295, 2004.

[42] T Baumgart, A T Hammond, P Sengupta, S T Hess, D A Holowka, B A Baird, and W W Webb. Large-scale fluid/fluid phase separation of proteins and lipids in giant plasma membrane vesicles. *P Natl Acad Sci USA*, 104(9):3165–3170, 2007.

[43] E Sezgin, I Levental, M Grzybek, G Schwarzmann, V Mueller, A Honigmann, V N Belov, C Eggeling, U Coskun, K Simons, and P Schwille. Partitioning, diffusion, and ligand binding of raft lipid analogs in model and cellular plasma membranes. *BBA - Biomembranes*, 1818(7):1777–1784, 2012.

[44] J Y Huang and G W Feigenson. Monte-Carlo Simulation of Lipid Mixtures - Finding Phase-Separation. *Biophys J*, 65(5):1788–1794, 1993.

[45] S A Pandit, E Jakobsson, and H L Scott. Simulation of the Early Stages of Nano-Domain Formation in Mixed Bilayers of Sphingomyelin, Cholesterol, and Dioleylphosphatidylcholine. *Biophys J*, 87(5):3312–3322, 2004.

[46] E Betzig and R J Chichester. Single molecules observed by near-field scanning optical microscopy. *Science*, 262:14221425, 1993.

[47] T Funatsu, Y Harada, M Tokunaga, K Saito, and T Yanagida. Imaging of single fluorescent molecules and individual ATP turnovers by single myosin molecules in aqueous solution. *Nature*, 374:555559, 1995.

[48] I Sase, H Miyata, J E T Corrie, J S Craik, and K Kinosita. Real time imaging of single fluorophores on moving actin with an epifluorescence microscope. *Biophys J*, 69:323328, 1995.

[49] T Schmidt, G J Schutz, W Baumgartner, H J Gruber, and H Schindler. Imaging single molecule diffusion. *Proc Natl Acad Sci*, 93:29262929, 1996.

[50] T Ha, T Enderle, D F Ogletree, D S Cemla, P R Selvin, and S Weiss. Probing the interaction between two single molecules: fluorescence resonance energy transfer between a single donor and a single acceptor. *Proc Natl Acad Sci*, 93:62646268, 1996.

[51] N F van Hulst, M F Garcia-Parajo, M H P Moers, J A Veerman, and A G T Ruiter. Near-field fluorescence imaging of generic material: towards the molecular limit. *J Struct Biol*, 119:222231, 1997.

[52] Y Jia, A Sytnik, L Li, S Vladimirov, B S Cooperman, and R M Hochstrasser. Nonexponential kinetics of a single tRNAPhe molecule under physiological conditions. *Proc Natl Acad Sci USA*, 94:79327936, 1997.

[53] S Jin and A S Verkman. Single Particle Tracking of Complex Diffusion in Membranes: Simulation and Detection of Barrier, Raft, and Interaction Phenomena. *J Phys Chem B*, 111(14):3625–3632, 2007.

[54] M J Saxton and K Jacobson. Single-particle tracking: applications to membrane dynamics. *Annu Rev Biomol Biophys Struct*, 26:373–99, 1997.

[55] M J Saxton. Anomalous diffusion due to obstacles: a Monte Carlo study. *Biophys Jl*, 6(2 part 1):394–401, 1994.

[56] M J Saxton. Anomalous diffusion due to binding: a Monte Carlo study. *Biophys J*, 239(4835):61–64, 1996.

[57] D Axelrod, D E Koppel, J Schlessinger, E Elson, and W W Webb. Mobility measurement by analysis of fluorescence photobleaching recovery kinetics. *Biophys J*, 16:10551069, 1976.

[58] E A J Reits and J J Neefjes. From fixed to FRAP: measuring protein mobility and activity in living cells. *Nature Cell Biology*, 3:E145–E147, 2001.

[59] N L Thompson. Fluorescence correlation spectroscopy. In J R Lakowicz, editor, *Topics in Fluorescence Spectroscopy*, pages 337–378. Plenum Press, 1991.

[60] R E Thompson, D R Larson, and W W Webb. Precise nanometer localization analysis for individual fluorescent probes. *Biophys J*, 82(5):2775–2783, 2002.

[61] S T Hess, S Huang, A A Heikal, and W W Webb. Biological and chemical applications of fluorescence correlation spectroscopy: a review. *Biochemistry*, 41:697–705, 2002.

[62] G J Schutz, H Schindler, and T Schmidt. Single-molecule microscopy on model membranes reveals anomalous diffusion. *Biophys J*, 73:10731080, 1997.

[63] K Bacia, D Scherfeld, N Kahya, and P Schwille. Fluorescence Correlation Spectroscopy Relates Rafts in Model and Native Membranes. *Biophys J*, 87(2):1034–1043, 2004.

[64] C Eggeling, C Ringemann, R Medda, G Schwarzmann, K Sandhoff, S Polyakova, V N Belov, B Hein, C von Middendorff, A Schönle, and S W Hell. Direct observation of the nanoscale dynamics of membrane lipids in a living cell. *Nature*, 457(7233):1159–1162, 2009.

[65] V Mueller, C Ringemann, A Honigmann, G Schwarzmann, R Medda, M Leutenegger, S Polyakova, V N Belov, S W Hell, and C Eggeling. STED Nanoscopy Reveals Molecular Details of Cholesterol and Cytoskeleton-Modulated Lipid Interactions in Living Cells. *Biophys J*, 101(7):1651–1660, 2011.

[66] V Mueller, H Ta, A Schoenle, E Sezgin, S W Hell, A Honigmann, and C Eggeling. Scanning STED-FCS reveals spatiotemporal heterogeneity of lipid interaction in the plasma membrane of living cells. *Nat Commun*, 5:1–12, 2014.

[67] S J Sahl, M Leutenegger, M Hilbert, S W Hell, and C Eggeling. Fast molecular tracking maps nanoscale dynamics of plasma membrane lipids. *Proc Natl Acad Sci*, 107(15):6829–6834, 2010.

[68] M Brameshuber, J Weghuber, V Ruprecht, I Gombos, I Horvat, L Vigh, P Eckerstorfer, E Kiss, H Stockinger, and G J Schutz. Imaging of mobile long-lived nanoplatforms in the live cell plasma membrane. *J Biol Chem*, 285:1765–41771, 2010.

[69] S B Triffo, H H Huang, A W Smith, E T Chou, and J T Groves. Monitoring lipid-anchor organization in cell membranes by PIE-FCCS. *J Am Chem Soc*, 134:833–842, 2012.

[70] R Varma and S Mayor. GPI-anchored proteins are organized in submicron domains at the cell surface. *Nature*, 394:798 801, 1998.

[71] D Goswami, K Gowrishankar, S Bilgrami, S Ghosh, R Raghupathy, R Chadda, R Vishwakarma, M Rao, and S Mayor. Nanoclusters of GPI-Anchored Proteins Are Formed by Cortical Actin-Driven Activity. *Cell*, 135(6):1085–1097, 2008.

[72] P Sharma, R Varma, R C Sarasij, I Ira, K Gousset, G Krishnamoorthy, M Rao, and S Mayor. Nanoscale Organization of Multiple GPI-Anchored Proteins in Living Cell Membranes. *Cell*, 116:577–589, 2004.

[73] F A Heberle, R S Petruzielo, J Pan, P Drazba, N Kučerka, R F Standaert, G W Feigenson, and J Katsaras. Bilayer Thickness Mismatch Controls Domain Size in Model Membranes. *J Am Chem Soc*, 135(18):6853–6859, 2013.

[74] M J Swamy, L Ciani, M Ge, A K Smith, D Holowka, B Baird, and J H Freed. Coexisting domains in the plasma membranes of live cells characterized by spin-label ESR spectroscopy. *Biophys J*, 90:4452–4465, 2006.

[75] T Parasassi, G De Stasio, A dUbaldo, and E Gratton. Phase fluctuation in phospholipid membranes revealed by Laurdan fluorescence. *Biophys J*, 57:1179–1186, 1990.

[76] T Parasassi and E Gratton. Membrane lipid domains and dynamics as detected by laurdan fluorescence. *J Fluoresc*, 365:373–385, 1995.

[77] S A Sanchez and M A Tricerri. Laurdan generalized polarization fluctuations measures membrane packing micro-heterogeneity in vivo. *P Natl Acad Sci USA*, 109(19):7314–7319, 2012.

[78] M Hof. Solvent relaxation in biomembranes. In W Rettig, B Strehmel, S Schrader, and H Seifert, editors, *Applied Fluorescence in Chemistry, Biology and Medicine*, pages 439–456. Springer, 1999.

[79] P Jurkiewicz, L Cwiklik, P Jungwirth, and M Hof. Lipid hydration and mobility: An interplay between fluorescence solvent relaxation experiments and molecular dynamics simulations. *Biochimie*, 94(1):26–32, 2012.

[80] M Stockl, A P Plazzo, and A Herrmann. Detection of lipid domains in model and cell membranes by fluorescence lifetime imaging microscopy of fluorescent lipid analogues. *J Biol Chem*, 283:30828–30837, 2008.

[81] O O Glebov and B J Nichols. Lipid raft proteins have a random distribution during localized activation of the T-cell receptor. *Nature Cell Biology*, 6(3):6–243, 2004.

[82] A K Kenworthy and M Edidin. Distribution of a glycosylphosphatidylinositol-anchored protein at the apical surface of MDCK cells examined at a resolution of 100 A using imaging fluorescence resonance energy transfer. *J Cell Biol*, 142:69–84, 1998.

[83] A K Kenworthy, B J Nichols, C L Remmert, G M Hendrix, M Kumar, J Zimmerberg, and J Lippincott-Schwartz. Dynamics of putative raft-associated proteins at the cell surface. *J Cell Biol*, 165:735–746, 2004.

[84] Y M Umemura, M Vrljic, S Y Nishimura, T K Fujiwara, K G N Suzuki, and A Kusumi. Both MHC class II and its GPI-anchored form undergo hop diffusion as observed by single-molecule tracking. *Biophys J*, 95(1):435–450, 2008.

[85] E D Sheets, G M Lee, R Simson, and K Jacobson. Transient confinement of a glycosylphosphatidylinositol-anchored protein in the plasma membrane. *Biochemistry*, 36(41):12449–58, 1997.

[86] Fujiwara and A Kusumi. Phospholipids undergo hop diffusion in compartmentalized cell membrane. *J Cell Biol*, 157(6):1071–1082, 2002.

[87] K Ritchie, X Shan, J Kondo, K Iwasawa, T Fujiwara, and A Kusumi. Detection of Non-Brownian Diffusion in the Cell Membrane in Single Molecule Tracking. *Biophys J*, 88(3):2266–2277, 2005.

[88] K Murase, T Fujiwara, Y Umemura, K Suzuki, R Iino, H Yamashita, M Saito, H Murakoshi, K Ritchie, and A Kusumi. Ultrafine Membrane Compartments for Molecular Diffusion as Revealed by Single Molecule Techniques. *Biophys J*, 86(6):4075–4093, 2004.

[89] M Tomishige, Y Sako, and A Kusumi. Regulation mechanism of the lateral diffusion of band 3 in erythrocyte membranes by the membrane skeleton. *J Cell Biol*, 142:989–1000, 1998.

[90] F Heinemann, Vogel S K, and P Schwille. Lateral membrane diffusion modulated by a minimal actin cortex. *Biophys J*, 104:1465–75, 2013.

[91] S Wieser, M Moertelmaier, E Fuertbauer, H Stockinger, and G J Schutz. (Un)confined diffusion of CD59 in the plasma membrane determined by high-resolution single molecule microscopy. *Biophys J*, 92(10):3719–28, 2007.

[92] M Przybylo, J Sykora, J Humpolíčková, A Benda, A Zan, and M Hof. Lipid diffusion in giant unilamellar vesicles is more than 2 times faster than in supported phospholipid bilayers under identical conditions. *Langmuir*, 22(22):9096–9099, 2006.

[93] R Merkel, E Sackmann, and E Evans. Molecular friction and epitactic coupling between monolayers in supported bilayers. *J Phys France*, 50:1535–1555, 1989.

[94] M R Morrow, D Singh, Lu D, and C W Grant. Glycosphingolipid fatty acid arrangement in phospholipid bilayers: cholesterol effects. *Biophys J*, 68(1):179–186, 1995.

[95] J M Boggs and K M Koshy. Do the long fatty acid chains of sphingolipids interdigitate across the center of bilayer of shorter chain symmetric phospholipids? *Biochim Biophys Acta*, 1189:233–241, 1992.

[96] S Chiantia and E London. Acyl Chain Length and Saturation Modulate Interleaflet Coupling inAsymmetric Bilayers: Effects on Dynamics and Structural Order. *Biophys J*, 103(11):2311–2319, 2012.

[97] M Javanainen, H Hammaren, M Monticelli, J Jeon, M S Miettinen, H Martinez-Seara, R Metzlerad, and I Vattulainen. Anomalous and normal diffusion of proteins and lipids in crowded lipid membranes. *Faraday Discuss*, 161:397–417, 2013.

[98] S Wieser, J Weghuber, M Sams, H Stockinger, and G J Schutz. Lateral membrane diffusion modulated by a minimal actin cortex. *Soft Matter*, 5:32873294, 2009.

[99] M Frick, K Schmidt, and B J Nichols. Modulation of lateral diffusion in the plasma membrane by protein density. *Curr Opin Biol*, 17:462–467, 2007.

[100] S Ramadurai, A Holt, V Krasnikov, G van den Bogaart, J A Killian, and B Poolman. Lateral Diffusion of Membrane Proteins. *J Am Chem Soc*, 131(35):12650–12656, 2009.

[101] J Domanski, S J Marrink, and L V Schafer. Transmembrane helices can induce domain formation in crowded model membranes. *Biochim Biophys Acta Biomembr*, 1818:984–994, 2012.

[102] P S Niemela, M Miettinen, L Monticelli, H Hammaren, P Bjelkmar, T Murtola, E Lindahl, and I Vattulainen. Membrane proteins diffuse as dynamic complexes with lipids. *J Am Chem Soc*, 132:7574–5, 2010.

[103] H Murakoshi, R Iino, T Kobayashi, T Fujiwara, C Oshima, A Yoshimura, and A Kusumi. Single-molecule imaging analysis of Ras activation in living cells. *Proc Natl Acad Sci USA*, 101:73177322, 2004.

[104] K G N Suzuki, T K Fujiwara, Sanematsu. F, R Iino, M Edidin, and A Kusumi. GPI-anchored receptor clusters transiently recruit Lyn and G for temporary cluster immobilization and Lyn activation: single-molecule tracking study. *J Cell Biol*, 177:717730, 2007.

[105] R S Kasai and A Kusumi. Single-molecule imaging revealed dynamic GPCR dimerization. *Curr Opin Cell Biol*, 27:7886, 2014.

[106] W E Moerner and L Kador. Optical detection and spectroscopy of single molecules in a solid. *Phys Rev Lett*, 62:2535–2538, 1989.

[107] P Kukura, M Celebrano, A Renn, and V Sandoghdar. Single-Molecule Sensitivity in Optical Absorption at Room Temperature. *J Phys Chem Lett*, 1(23):3323–3327, 2010.

[108] S Chong, W Min, and X S Xie. Ground-State Depletion Microscopy: Detection Sensitivity of Single-Molecule Optical Absorption at Room Temperature. *J Phys Chem Lett*, 1:3316–3322, 2010.

[109] H Deschout, K Neyts, and K Braeckmans. The influence of movement on the localization precision of sub-resolution particles in fluorescence microscopy. *J Biophotonics*, 5(1):97–109, 2011.

[110] A Yildiz, J N Forkey, S A McKinner, T Ha, Y E Goldman, and P R Selvin. Myosin V walks hand-over-hand: single fluorophore imagingwith 1.5-nm localization. *Science*, 300:20612065, 2003.

[111] A Pertsinidis, Y Zhang, and S Chu. Subnanometre single-molecule localization, registration and distance measurements. *Nature*, 466(7306):647–651, 2010.

[112] A Kusumi, T A Tsunoyama, K M Hirosawa, Kasai R S, and T K Fujiwara. Tracking single molecules at work in living cells. *Nature Chem Biol*, 10:524–32, 2014.

[113] X Michalet, F F Pinaud, L A Bentoilia, J M Tsay, S Doose, J J Li, G Sundaresan, A M Wu, S S Gambhir, and S Weiss. Quantum dots for live cells, in vivo imaging, and diagnostics. *Science*, 307:538–44, 2005.

[114] H Geerts, M De Brabander, R Nuydens, S Geuens, M Moeremans, J De Mey, and P Hollenbeck. Nanovid tracking: a new automatic method for the study of mobility in living cells based on colloidal gold and video microscopy. *Biophys J*, 52:775–82, 1987.

[115] J Ortega-Arroyo and P Kukura. Interferometric scattering microscopy (iSCAT): new frontiers in ultrafast and ultrasensitive optical microscopy. *Phys Chem Chem Phys*, 14(45):15625, 2012.

[116] A Curtis. The mechanism of adhesion of cells to glass A study by interference reflection microscopy. *J Cell Biol*, 20:199–215, 1964.

[117] M Piliarik and V Sandoghdar. Direct optical sensing of single unlabelled proteins and super-resolution imaging of their binding sites. *Nat Commun*, 5, 2014.

[118] J Ortega-Arroyo, J Andrecka, K M Spillane, N Billington, Y Takagi, J R Sellers, and P Kukura. Label-Free, All-Optical Detection, Imaging, and Tracking of a Single Protein. *Nano Lett*, 14(4):2065–2070, 2014.

[119] H Ueno, S Nishikawa, R Iino, K V Tabata, S Sakakihara, T Yanagida, and H Noji. Simple Dark-Field Microscopy with Nanometer Spatial Precision and Microsecond Temporal Resolution. *Biophys J*, 98(9):2014–2023, 2010.

[120] P Kukura, H Ewers, C Müller, A Renn, A Helenius, and V Sandoghdar. High speed nanoscopic tracking of the position and orientation of a single virus. *Nat Methods*, 6(12):923–927, 2009.

[121] J Andrecka and P Kukura. Label-free detection of the Assembly of Microtubules. Publication in preparation.

[122] J Andrecka, K M Spillane, J Ortega-Arroyo, and P Kukura. Direct observation and control of supported lipid bilayer formation with interferometric scattering microscopy. *ACS nano*, 7(12):10662–10670, 2013.

[123] J Ortega-Arroyo, A Biestte, and P Kukura. Single-molecule chemical dynamics: direct observation of physical autocatalysis. Publication in preparation.

[124] K Lee and M El-Sayed. Dependence of the Enhanced Optical Scattering Efficiency Relative to That of Absorption for Gold Metal Nanorods on Aspect Ratio, Size, End-Cap Shape, and Medium Refractive Index. *J Phys Chem B*, 109(43):2033120338, 2006.

[125] A O Govorov, W Zhang, T Skeini, H Richardson, J Lee, and N A Kotov. Gold nanoparticle ensembles as heaters and actuators: melting and collective plasmon resonances. *Nanoscale Res Lett*, 1:84–90, 2006.

[126] K Jiang, D A Smith, and Pinchuk. Size-Dependent Photothermal Conversion Efficiencies of Plasmonically Heated Gold Nanoparticles. *J Phys Chem C*, 117(51):27073–27080, 2013.

[127] M Honda, Y Saito, N I Smith, K Fujita, and S Kawata. Nanoscale heating of laser irradiated single gold nanoparticles in liquid. *Opt Express*, 19(13):12375–83, 2011.

[128] J Waters. Accuracy and precision in quantitative fluorescence microscopy. *J Cell Biol*, 185(7):1135–1148, 2009.

[129] J Raedler and E Sackmann. On the measurement of weak repulsive and frictional colloidal forces by reflection interference contrast microscopy. *Langmuir*, 8:848–853, 1992.

[130] J Hwang and W E Moerner. Interferometry of a single nanoparticle using the Gouy phase of a focused laser beam. *Opt Commun*, 280(2):487–491, 2007.

[131] B Hajj, J Wisniewski, M El Beheiry, J Chen, A Revyakin, C Wu, and M Dahan. Whole-cell, multicolor superresolution imaging using volumetric multifocus microscopy. *Proc Natl Acad Sci USA*, 111:17480–17485, 2014.

[132] R J Ober, S Ram, and E S Ward. Localization accuracy in single-molecule microscopy. *Biophys J*, 86:1185–1200, 2004.

[133] R J Ober, S Ram, and E S Ward. High accuracy 3D quantum dot tracking with multifocal plane microscopy for the study of fast intracellular dynamics in live cells. *Biophys J*, 95:6025–6043, 2008.

[134] H P Kao and A S Verkman. Tracking of single fluorescent particles in three dimensions: use of cylindrical optics to encode particle position. *Biophys J*, 67(3):1291–300, 1994.

[135] L Holtzer, T Meckel, and T Schmidt. Nanometric three-dimensional tracking of individual quantum dots in cells. *Appl Phys Lett*, 90:053902, 2007.

[136] B Huang, W Wang, M Bates, and X Zhuang. Three-Dimensional Super-Resolution Imaging by Stochastic Optical Reconstruction Microscopy. *Science*, 319(5864):810–813, 2008.

[137] S Quirin, S R P Pavani, and R Piestun. Optimal 3D single-molecule localization for superresolution microscopy with aberrations and engineered point spread functions. *Proc Natl Acad Sci USA*, 109:675–679, 2012.

[138] Y Shechtman, L E Weiss, A S Backer, S J Sahl, and W E Moerner. Three-Dimensional Scan-Free Multiple-Particle Tracking over Large Axial Ranges with Tetrapod Point Spread Functions. *Nano Lett*, 15:4194–4199, 2015.

[139] K M Spillane, J Ortega-Arroyo, G de Wit, C Eggeling, H Ewers, M I Wallace, and P Kukura. High-Speed Single-Particle Tracking of GM1 in Model Membranes Reveals Anomalous Diffusion due to Interleaflet Coupling and Molecular Pinning. *Nano Lett*, 14:5390–5397, 2014.

[140] J W Gibbs. The equilibrium of Heterogeneous Substances. *T Conn Acad Arts Sci*, 3(5), 1874-1878.

[141] P F Almeida, A Pokorny, and A Hinderliter. Thermodynamics of membrane domains. *Biochim Biophys Acta*, 1720:1–13, 2005.

[142] D G Ackerman and G W Feigenson. Lipid bilayers: clusters, domains and phases. *Essays Biochem*, 57:33–42, 2015.

[143] A Radhakrishnan, T G Anderson, and H M McConnell. Condensed complexes, rafts, and the chemical activity of cholesterol in membranes. *Proc Natl Acad Sci USA*, 9:12422–7, 2000.

[144] X M Li, M M Momsen, J M Smaby, H L Brockman, and R E Brown. Cholesterol decreases the interfacial elasticity and detergent solubility of sphingomyelins. *Biochem*, 40:5954–63, 2001.

[145] S L Veatch and S L Keller. Separation of liquid phases in giant vesicles of ternary mixtures of phospholipids and cholesterol. *Biophys J*, 85(5):3074–3083, 2003.

[146] V A J Frolov, Y A Chizmadzhev, F S Cohen, and J Zimmerberg. "Entropic Traps" in the Kinetics of Phase Separation in Multicomponent Membranes Stabilize Nanodomains. *Biophys J*, 91(1):189–205, 2006.

[147] S L Veatch and S L Keller. Seeing spots: Complex phase behavior in simple membranes. *BBA - Mol Cell Res*, 1746(3):172–185, 2005.

[148] Sarah L Veatch. From small fluctuations to large-scale phase separation: lateral organization in model membranes containing cholesterol. *Semin cell dev biol*, 18(5):573–582, 2007.

[149] M Skocaj, B Bakrac, I Krizaj, P Macek, G Anderluh, and K Sepcic. The Sensing of Membrane Microdomains Based on Pore-Forming Toxins. *Current Medicinal Chemistry*, 20(4):491–501, 2013.

[150] M C Howland, A W Szmodis, B Sanii, and A N Parikh. Characterization of Physical Properties of Supported Phospholipid Membranes Using Imaging Ellipsometry at Optical Wavelengths. *Biophys J*, 92(4):1306–1317, 2007.

[151] D Marsh. Liquid-ordered phases induced by cholesterol: A compendium of binary phase diagrams. *BBA - Biomembranes*, 1788(10):2114–2123, 2009.

[152] J R Silvius. Role of cholesterol in lipid raft formation: lessons from lipid model systems. *BBA - Biomembranes*, 1610(2):174–183, 2003.

[153] R F M de Almeida, A Fedorov, and M Prieto. Sphingomyelin / Phosphatidylcholine / Cholesterol Phase Diagram: Boundaries and Composition of Lipid Rafts. *Biophys J*, 85(4):2406–2416, 2003.

[154] F A Heberle, J Wu, S L Goh, R S Petruzielo, and G W Feigenson. Comparison of Three Ternary Lipid Bilayer Mixtures: FRET and ESR Reveal Nanodomains. *Biophys J*, 99(10):3309–3318, 2010.

[155] S L Veatch, K Gawrisch, and S L Keller. Closed-loop miscibility gap and quantitative tie-lines in ternary membranes containing diphytanoyl PC. *Biophys J*, 90(12):4428–4436, 2006.

[156] J Zhao, F A Heberle, T T Mills, P Klawitter, G Huang, G Costanza, and G W Feigenson. Phase studies of model biomembranes: Complex behavior of DSPC/DOPC/cholesterol. *Biochim Biophys Acta*, 1768(1):2764–2776, 2007.

[157] S Leptihn, O K Castell, B Cronin, E Lee, L C M Gross, D P Marshall, J R Thompson, M Holden, and M I Wallace. Constructing droplet interface bilayers from the contact of aqueous droplets in oil. *Nat Protoc*, 8(6):1048–1057, 2013.

[158] H Bayley, B Cronin, A Heron, M A Holden, W L Hwang, R Syeda, J Thompson, and M I Wallace. Droplet interface bilayers. *Mol BioSyst*, 4(12):1191, 2008.

[159] L C M Gross, A J Heron, S C Baca, and M I Wallace. Determining Membrane Capacitance by Dynamic Control of Droplet Interface Bilayer Area. *Langmuir*, 27(23):14335–14342, 2011.

[160] J R Thompson, A J Heron, Y Santoso, and M I Wallace. Enhanced Stability and Fluidity in Droplet on Hydrogel Bilayers for Measuring Membrane Protein Diffusion. *Nano Lett*, 7(12):3875–3878, 2007.

[161] K Jaqaman, D Loerke, M Mettlen, H Kuwata, S Grinstein, S L Schmid, and G Danuser. Robust single-particle tracking in live-cell time-lapse sequences. *Nat Methods*, 5(8):695–702, 2008.

[162] P G Saffman and M Delbruck. Brownian Motion in Biological Membranes. *P Natl Acad Sci USA*, 72(8):3111–3113, 1975.

[163] A Naji, A J Levine, and P A Pincus. Corrections to the Saffman-Delbruck mobility for membrane bound proteins. *Biophys J*, 93(11):49–51, 2007.

[164] E P Petrov and P Schwille. Translational Diffusion in Lipid Membranes beyond the Saffman-Delbrück Approximation. *Biophys J*, 94(5):L41–L43, 2008.

[165] B D Hughes, B A Pailthorpe, and L R White. The Translational and Rotational Drag on a Cylinder Moving in a Membrane. *J Fluid Mech*, 110:349–372, 1981.

[166] E P Petrov, R Petrosyan, and P Schwille. Translational and rotational diffusion of micrometer-sized solid domains in lipid membranes. *Soft Matter*, 8(29):7552, 2012.

[167] G Guigas and M Weiss. Size-Dependent Diffusion of Membrane Inclusions. *Biophys J*, 91(7):2393–2398, 2006.

[168] P Espanol. Dissipative particle dynamics. In Sydney Yip, editor, *Handbook of Materials Modeling*, pages 2503–2512. Springer Netherlands, 2005.

[169] P Espanol and P Warren. Statistical-Mechanics of Dissipative Particle Dynamics. *EPL*, 30(4):191–196, 1995.

[170] E Evans and E Sackmann. Translational and Rotational Drag Coefficients for a Disk Moving in a Liquid Membrane-Associated with a Rigid Substrate. *J Fluid Mech*, 194:553–561, 1988.

[171] I Plasencia, L Norlén, and L A Bagatolli. Direct Visualization of Lipid Domains in Human Skin Stratum Corneum's Lipid Membranes: Effect of pH and Temperature. *Biophys J*, 93(9):3142–3155, 2007.

[172] G G Ruocco, M J Shipley. Interaction of cholesterol with galactocerebroside and galactocerebroside-phosphatidylcholine bilayer membranes. *Biophys J*, 46(6):695–707, 1984.

[173] K Simons and J L Sampaio. Membrane Organisation and Lipid Rafts. *Cold Spring Harb Perspect Biol*, 3:6a004697, 2011.

[174] K Simons and D Toomre. Lipid rafts and signal transduction. *Nat Rev Mol Cell Biol*, 1(1):31–39, 2001.

[175] A K Kenworthy, N Petranova, and M Edidin. High-resolution FRET microscopy of cholera toxin B-subunit and GPI-anchored proteins in cell plasma membranes. *Mol Biol Cell*, 11:1645–1655, 2000.

[176] S A Pandit, E Jakobsson, and H L Scott. Simulation of the Early Stages of Nano-Domain Formation in Mixed Bilayers of Sphingomyelin, Cholesterol, and Dioleylphosphatidylcholine. *Biophys J*, 87(5):3312–3322, 2004.

[177] E Ikonen. Cellular cholesterol trafficking and compartmentalization. *Nature Rev Mol Cell Biol*, 9:125–138, 2009.

[178] T Gil, M C Sabra, J H Ipsen, and O G Mouritsen. Wetting and capillary condensation as means of protein organization in membranes. *Biophys J*, 73(4):1728–1741, 1997.

[179] S Meinhardt, R L C Vink, and F Schmid. Monolayer curvature stabilizes nanoscale raft domains in mixed lipid bilayers. *Proc Natl Acad Sci USA*, 110(12):4476–4481, 2013.

[180] J J Amazon, S L Goh, and G W Feigenson. Competition between line tension and curvature stabilizes modulated phase patterns on the surface of giant unilamellar vesicles: A simulation study. *Phys Rev E*, 87(2):022708, 2013.

[181] S L Veatch, O Soubias, S L Keller, and K Gawrisch. Critical fluctuations in domain-forming lipid mixtures. *P Natl Acad Sci USA*, 104(45):17650–17655, 2007.

[182] J Ehrig, E P Petrov, and P Schwille. Phase separation and near-critical fluctuations in two-component lipid membranes: Monte Carlo simulations on experimentally relevant scales. *New J Phys*, 13(7233):1159–1162, 2011.

[183] S Wennmalm, P Thyberg, L Xu, and J Widengren. Molecular friction and epitactic coupling between monolayers in supported bilayers. *Anal Chem*, 81:9209–9215, 2009.

[184] P M Crespo, N von Muhlinen, R Iglesias-Bartolome, and J L Daniotti. The association of viral proteins with host cell dynein components during virus infection. *FEBS J*, 278(17):6043–6056, 2008.

[185] D J F Chinnapen, W T Hsieh, Y M Welscher, D E Saslowsky, L Kaoutzani, E Brandsma, L D'Auria, H Park, J S Wagner, K. R Drake, M Kang, T Benjamin, M. D Ullman, C E Costello, A. K Kenworthy, T Baumgart, R H Massol, and W I Lencer. Lipid sorting by ceramide structure from plasma membrane to ER for the cholera toxin receptor ganglioside GM1. *Dev Cell*, 23(3):573–586, 2012.

[186] N Gupta and A L DeFranco. Visualizing lipid raft dynamics and early signaling events during antigen receptor-mediated B-lymphocyte activation. *Mol Cell Biol*, 14(2):432–444, 2003.

[187] J Shi, T Yang, S Kataoka, Y Zhang, A J Diaz, and P S Cremer. GM1 Clustering Inhibits Cholera Toxin Binding in Supported Phospholipid Membranes. *J Am Chem Soc*, 129(18):5954–5961, 2007.

[188] C Dietrich, Z N Volovyk, and M Levi. Partitioning of Thy-1, GM1, and cross-linked phospholipid analogs into lipid rafts reconstituted in supported model membrane monolayers. In *P Natl Acad Sci USA*, volume 98, pages 10642–7, 2001.

[189] C Dietrich, B Yang, T Fujiwara, A Kusumi, and K Jacobson. Relationship of lipid rafts to transient confinement zones detected by single particle tracking. *Biophys J*, 82(1):274–284, 2002.

[190] P Mascalchi, E Haanappel, K Carayon, S Mazères, and L Salomé. Probing the influence of the particle in Single Particle Tracking measurements of lipid diffusion. *Soft Matter*, 8(16):4462, 2012.

[191] D S Martin, M B Forstner, and J A Käs. Apparent Subdiffusion Inherent to Single Particle Tracking. *Biophys J*, 83(4):2109–2117, 2002.

[192] Thierry Savin and Patrick S Doyle. Static and dynamic errors in particle tracking microrheology. *Biophys J*, 88(1):623–638, 2005.

[193] H Ewers, W Rómer, A E Smith, K Bacia, S Dmitrieff, W Chai, R Mancini, J Kartenbeck, V Chambon, L Berland, A Oppenheim, G Schwarzmann, T Feizi, P Schwille, P Sens, A Helenius, and L Johannes. GM1 structure determines SV40-induced membrane invagination and infection. *Nat Cell Biol*, 12(1):11–18, 2010.

[194] E Sackmann. Supported membranes: scientific and practical applications. *FEBS J*, 271(5245):43–48, 2008.

[195] R Šachl, M Amaro, G Aydogan, A Koukalova, I I Mikhalyov, I A Boldyrev, J Humpolíčková, and M Hof. On multivalent receptor activity of GM1 in cholesterol containing membranes. *Biochim Biophys Acta*, 1843(4):850–857, 2014.

[196] M Seul and S Subramaniam. Mono-and bilayers of phospholipids at interfaces: interlayer coupling and phase stability. *P Natl Acad Sci USA*, 89(17):3592–3595, 1985.

[197] G van den Bogaart, N Hermans, V Krasnikov, A H de Vries, and B Poolman. On the decrease in lateral mobility of phospholipids by sugars. *Biophys J*, 92(5):1598–605, 2007.

[198] N Chada, K P Sigdel, R Gari, Raghavendar, T R Matin, L L Randall, and G M King. Glass is a Viable Substrate for Precision Force Microscopy of Membrane Proteins. *Nature*, 5:12550, 2015.

[199] C Hsieh, S Spindler, J Ehrig, and V Sandoghdar. Tracking Single Particles on Supported Lipid Membranes: Multimobility Diffusion and Nanoscopic Confinement. *J Phys Chem B*, 118(6):1545–1554, 2014.

[200] W Malorni, U Testa, G Rainaldi, E Tritarelli, and C Peschle. Oxidative stress leads to a rapid alteration of transferrin receptor intravesicular trafficking. *Exp Cell Res*, 241:102–16, 1998.

[201] M Coue, S L Brenner, I Spector, and E D Korn. Inhibition of actin polymerization by latrunculin A. *FEBS Letters*, 213(2):316–318, 1987.

[202] J F Casella, M D Flanagan, and S Lin. Cytochalasin D inhibits actin polymerization and induces depolymerization of actin filaments formed during platelet shape change. *Nature*, 293(5830):302–305, 1981.

[203] S Y Nishimura, M Vrljic, L O Klein, H M McConnell, and W E Moerner. Cholesterol depletion induces solid-like regions in the plasma membrane. *Biophys J*, 90:927–38, 2006.

[204] M Vrljic, S Y Nishimura, S Brasselet, W E Moerner, and H M McConnell. Translational diffusion of individual class II MHC membrane proteins in cells. *Biophys J*, 83:2681–92, 2002.

[205] K Suzuki, K Ritchie, E Kajikawa, T Fujiwara, and A Kusumi. Rapid hop diffusion of a G-protein-coupled receptor in the plasma membrane as revealed by single-molecule techniques. *Biophys J*, 88(5):3659–80, 2005.

[206] L Wawrezinieck, H Rigneault, D Marguet, and P Lenne. Fluorescence Correlation Spectroscopy Diffusion Laws to Probe the Submicron Cell Membrane Organization. *Biophys J*, 89(6):4029–4042, 2005.

[207] P F Lenne, L Wawrezinieck, and D E Marguet. Dynamic molecular confinement in the plasma membrane by microdomains and the cytoskeleton meshwork. *EMBO J*, 25:32453256, 2006.

[208] G Lukinavicius, L Reymond, E D'Este, M Masharina, F Gottfert, H Ta, A Guther, M Fournier, S Rizzo, and H Waldmann. Fluorogenic probes for live-cell imaging of the cytoskeleton. *Nat Methods*, 11:731–733, 2014.

[209] A Pralle, P Keller, E L Florin, K Simons, and J K Horber. Sphingolipid-cholesterol rafts diffuse as small entities in the plasma membrane of mammalian cells. *J Cell Biol*, 148:997–1008, 2000.

[210] P Keller, D Toomre, E Diaz, J White, and K Simons. Multicolour imaging of post-Golgi sorting and trafficking in live cells. *Nat Cell Biol*, 3:140–149, 2001.

[211] D Albrecht. PhD thesis, 2015.

[212] S Kaech and G Banker. Culturing Hippocampal Neurons. *Nat Protocols*, 1(5):2406–2415, 2006.

[213] H Ewers, T Tada, J D Petersen, B Racz, M Sheng, and D Choquet. A septin-dependent diffusion barrier at dendritic spine necks. *PLoS One*, 9:e113916, 2014.

[214] M M Sperotto and O G Mouritsen. Monte Carlo simulation studies of lipid order parameter profiles near integral membrane proteins. *Biophys J*, 59(2):261–70, 1991.

[215] P F F Almeida, W L C Vaz, and T E Thompson. Lateral diffusion and percolation in two-phase, two-component lipid bilayers. Topology of the solid-phase domains in-plane and across the lipid bilayer. *Biochemistry*, 298:18–25, 1992.

[216] J Ries, C Kaplan, E Platonova, H Eghlidi, and H Ewers. A simple, versatile method for GFP-based super-resolution microscopy via nanobodies. *Nat Methods*, 9(6):582–584, 2012.

[217] P V Gaiduk, A Ruijgrok, M Yorulmaz, and Orrit M. Making gold nanoparticles fluorescent for simultaneous absorption and fluorescence detection on the single particle level. *Phys Chem Chem Phys*, 13:149–153, 2011.

[218] E Dulkeith, A C Morteani, T Niedereichholz, T A Klar, J Feldmann, S A Levi, F C van Veggel, D N Reinhoudt, M Moller, and D I Gittins. Fluorescence quenching of dye molecules near gold nanoparticles: radiative and nonradiative effects. *Phys Rev Lett*, 89:203002, 2002.

[219] S Mayilo, M A Kloster, M Wunderlich, A Lutich, T A Klar, A Nichtl, K Kurzinger, F D Stefani, and J Feldmann. Long-Range Fluorescence Quenching by Gold Nanoparticles in a Sandwich Immunoassay for Cardiac Troponin. *Nano Lett*, 9(12):4558–4563, 2009.

[220] W L C Vaz, F Goodsaid-Zalduondo, and K Jacobson. Lateral diffusion of lipids and proteins in bilayer membranes. *Febbs Lett*, 174(2):199–207, 1984.

[221] W W Webb, L S Barak, D W Tank, and E S P Wu. Molecular mobility on the cell surface. *Biochem Soc Symp*, 46:191–205, 1981.

[222] A Kusumi, I Koyama-Honda, and K Suzuki. Molecular dynamics and interactions for creation of stimulation-induced stabilized rafts from small unstable steady-state rafts. *Traffic*, 5(4):213–30, 2004.

[223] K G N Suzuki, R S Kasai, K M Hirosawa, Y L Nemoto, M Ishibashi, Y Miwa, T K Fujiwara, and A Kusumi. Transient gpi-anchored protein homodimers are units for raft organization and function. *Nat Chem Biol*, 8(9):774–783, 2012.

[224] R Raghupathy, A A Anilkumar, A Polley, P P Singh, M Yadav, C Johnson, S Suryawanshi, V Saikam, S D Sawant, A Panda, Z Guo, R A Vishwakarma, M Rao, and S Mayor. Transbilayer Lipid Interactions Mediate Nanoclustering of Lipid-Anchored Proteins. *Cell*, 161(3):581–594, 2015.

[225] D E Shvartsman, M Kotler, R D Tall, M G Roth, and Y I Henis. Differently anchored influenza hemagglutinin mutants display distinct interaction dynamics with mutual rafts. *J Cell Biol*, 163(4):879–88, 2003.